UNIVERSIDADE DE LISBOA
FACULDADE DE CIÊNCIAS
DEPARTAMENTO DE FÍSICA

Biases in weak lensing measurements of galaxy simulated images

Ana Patrícia Amaral Rodrigues

Mestrado em Física
Especialização em Astrofísica e Cosmologia

Dissertação orientada por:
Dr. Ismael Tereno
Dr. Carla Sofia Carvalho

2021

Acknowledgments

Among all of the people involved in the completion of this thesis, I must begin by thanking my supervisor, Ismael Tereno, for offering me the opportunity that led to the work presented here. Without him I would most likely never had pursued a Cosmology-related project. He encouraged me to leave my comfort zone and work on a topic that not only brought diversity to my research experience, but also personal growth.

I am beyond grateful to my co-supervisor, Sofia Carvalho, for all the time and dedication she has put into this work, always making sure I felt supported. Her invaluable advice during this journey allowed me to stay both motivated and reassured, and I know I will be carrying her words with me throughout my professional life, wherever that leads me.

A special thanks to António da Silva who witnessed my evolution throughout this thesis, and was a constant source of motivation, so important in many moments of self-doubt. His helpful contributions with coding suggestions and presentation solutions definitely improved the final work.

I am thankful to the EWC team, specially to Dr. Tim Schrabback and Dr. Henk Hoekstra for their input on my results; to Diana Scognamiglio for her availability to answer my questions; and to Chris Duncan for staying four hours on Slack helping me setup his *Euclid* PSF modelling code. I am also thankful to the entire team at IA, an institution that will always have a special place in my heart, in particular to Carlos Santos, Sandra Homem, and João Retrê.

To the ones who always have my back, and that have supported me through the thick and thin: Marta, Isabel, Carolina, Rafael, and Miguel. Thank you so much for the feedback, for the guidance, and for the friendship.

For her incredible feedback and last-minute, panic-soothing help, a heartfelt thanks to Aoife Boyle.

I am grateful to have shared this MSc journey with my friends and colleagues: Victor, André, Miguel, and Ana. With a special thanks to Victor for his precious advice and constant support.

Working on this thesis through two home confinement orders, and restricted living for more than a year was an added challenge, both in work execution and mentally. For this I am grateful to Xiomara Pereira, for being my home support and keeping me sane.

And last, but most certainly not least, an enormous thank you to my mother. Even though we have been living in different countries since my 18th birthday, she has always been my biggest support.

Abstract

Weak gravitational lensing due to the large-scale distribution of matter in the Universe is responsible for introducing distortions to the images of distant galaxies, in a process known as cosmic shear. This occurs due to the deflection of light by the gravitational field produced by matter inhomogeneities along the line-of-sight, which coherently deforms the observed ellipticity of such galaxies. The dependence of this effect on the dynamics of large-scale structures makes it a powerful tool for probing the nature of dark matter and the evolution of dark energy, allowing constraints to be made to cosmological parameters.

Over the years, an increase in precision of cosmological data has been accompanied by an increase in sensitivity to systematic errors. These must be modelled and removed from the measurements, with the accuracy of this calibration becoming a relevant limitation to the performance of future cosmological observations, such as the ones made by the *Euclid* mission.

Following this growing concern, this thesis is focused on the quantification of biases introduced by specific image manipulation procedures, and the evaluation of their impact in the constraint of the cosmological parameters Ω_m and σ_8. The first step of this work involved the simulation of parametric galaxy images with realistic properties. To these, a mock variable cosmic shear signal was introduced, after which a point spread function (PSF) was applied, in conjunction with noise as a function of exposure time. This defined the first calibration tests, aiming to quantify the bias from the PSF removal algorithm in the presence of a realistic sample, with noise properties, and as a function of an input cosmic shear signal. The bias analysis from these first tests was done based on galaxy properties, confirming that smaller, fainter galaxies are more susceptible to bias. The results of this analysis also showed that the residual errors from the PSF correction method used in this work strongly depend on both galaxy and PSF ellipticities.

The next steps of this work used simulated *Euclid*-like images, with the objective of quantifying the systematics introduced by the process of dithering and subsequent stacking of dithered images, and the bias introduced by *Euclid*'s PSF variation along its field-of-view (FoV). Analysing the residual errors remaining after correcting the PSF in different set-ups demonstrated the importance of an accurately modelled PSF, and the calibration of each data processing step regarding systematics.

The bias values obtained in the first part of the thesis were then included in the procedure to constrain Ω_m and σ_8 parameters. This was done by computing biased correlation functions and the respective maximum likelihood regions, in simulated *Euclid*-like observing conditions. The results of this analysis allow an overview of the impact that these routine image manipulation procedures and PSF variations might have on weak lensing measurements.

Keywords: weak gravitational lensing, galaxy image simulations, systematic effects; data analysis; cosmological parameters.

Resumo

O último século assistiu a uma evolução significativa na área da Cosmologia, em particular ao nascimento da Cosmologia Observacional, impulsionado por um contínuo desenvolvimento tecnológico. Modelos teóricos outrora impossíveis de serem verificados puderam, finalmente, apoiar-se na observação de fenómenos cosmológicos para a sua validação. Entre as observações mais relevantes está o fenómeno de lentes gravitacionais, que revolucionou o conhecimento que até então se tinha sobre a composição e dinâmica do Universo, confirmando a teoria proposta por Einstein de que a presença de matéria alteraria a geometria do espaço-tempo, defletindo a luz durante a sua propagação.

O efeito de lentes gravitacionais pode ser descrito pelo campo gravitacional criado pela distribuição de matéria no Universo, sendo classificado consoante a intensidade com que são alteradas a forma e orientação das galáxias observadas. Quando este efeito de distorção se deve à distribuição de matéria a grande escala, é observado como uma acumulação de pequenas alterações na forma destes objetos, num efeito conhecido como cisalhamento cósmico (ou *cosmic shear*). Embora subtil, deste efeito podem ser extraídas informações importantes sobre a constituição e evolução do Universo, uma vez que depende intrinsecamente da quantidade matéria presente, independentemente da sua natureza. O atual modelo cosmológico descreve a composição do Universo como sendo dominada por duas componentes sobre as quais a informação é ainda insuficiente: matéria e energia escuras. Desta forma, a exploração da relação entre o efeito de cisalhamento cósmico e a quantidade total de matéria, permite não só determinar a distribuição espacial desta componente, mas também caracterizar o impacto da energia escura na evolução da dinâmica do Universo, devido à relação entre as duas componentes.

Sendo medido através da elipticidade das galáxias observadas, o impacto deste fenómeno é muito pequeno, quantificado apenas através da correlação entre elipticidades observadas entre galáxias. Com a crescente precisão de experiências futuras, efeitos subtis como o cisalhamento cósmico estão especialmente sujeitos a erros sistemáticos (ou *bias*). Em particular, o fator dominante, de entre os vários responsáveis, é a *point spread function* (PSF) específica do telescópio. Resultante da contribuição dos vários elementos óticos e de deteção do instrumento, a PSF e o respetivo resíduo de remoção, produzido pelo algoritmo de correção de PSF usado, sobrepõem-se ao efeito cosmológico em estudo. Devido aos exigentes requisitos científicos impostos a futuras observações, como as da missão *Euclid*, será necessário produzir uma análise extensiva aos vários fatores que podem influenciar as medições, de modo a calibrar os resultados tendo em conta estes erros sistemáticos.

É precisamente este efeito de *cosmic shear* que se encontra na base do trabalho desenvolvido nesta dissertação. Em particular, a quantificação de erros sistemáticos introduzidos por procedimentos específicos de manipulação de imagem, que contaminam as medições de quantidades cosmológicas dependentes deste fenómeno. Esta incerteza adicional é parametrizada por dois factores, um de caráter aditivo e outro de caráter multiplicativo, e afetam diretamente as observações de elipticidade das galáxias.

O procedimento aplicado na quantificação do impacto deste *bias* na estimativa de quantidades cosmológicas, passou numa primeira fase pela simulação de imagens de galáxias individuais, usando o

programa *GalSim*. À elipticidade intrínseca de uma amostra realista de galáxias paramétricas (criadas a partir de características de objetos reais, observados pelo *Hubble Space Telescope* (HST)), foi adicionada uma distorção com o objectivo de simular o efeito de cisalhamento cósmico. Estas imagens foram posteriormente convoluídas com uma PSF semelhante à da missão *Euclid*, após o qual foi adicionado ruído.

Com vista a avaliar o resíduo deixado pelo método de remoção da distorção associada à PSF (método KSB), foram feitos dois tipos de testes. O primeiro incluiu, para além do efeito da PSF, a variação do sinal de *cosmic shear*, enquanto o segundo teste adicionou a ambos estes fatores o efeito de ruído, simulado a partir da variação do tempo de exposição. A análise de ambos os testes foi realizada considerando o conjunto de galáxias agrupado em intervalos de *redshift*, magnitude e tamanho. Esta divisão da análise em função das propriedades referidas permitiu avaliar a existência de correlações entre o *bias* obtido e algumas das características principais da amostra.

Os resultados destes testes de calibração demonstraram uma ausência de correlação entre o *redshift* das galáxias e os *biases* aditivo e multiplicativo, revelando, no entanto, que galáxias de maior magnitude (menor brilho) e mais pequenas (em área ocupada na imagem) foram as mais prejudicadas. Este comportamento era esperado, uma vez que objetos nestas condições são mais suscetíveis a erros sistemáticos. Em particular, o ruído aplicado no segundo teste produziu valores superiores de *bias*, aumentando a incerteza das medições. Atendendo a que as observações de *cosmic shear* são compostas, em grande parte, por galáxias longínquas que se enquadram maioritariamente nestas duas características, estes resultados permitem confirmar a importância de uma calibração precisa face a efeitos sistemáticos. Foi igualmente verificado que, de uma forma geral, os valores obtidos para o *bias* se encontram dentro do intervalo de valores de referência obtidos noutros trabalhos semelhantes, notando que o valor elevado do termo aditivo de *bias* coincide com uma maior elipticidade da PSF aplicada. O método KSB introduz resíduos mais elevados quanto maior a elipticidade, quer do objecto observado quer da PSF aplicada, efeito já previamente reportado noutros estudos sobre este algoritmo.

Estando esta dissertação inserida no âmbito da missão *Euclid*, a segunda parte deste trabalho focou-se na simulação de imagens com características realistas, semelhantes às esperadas nesta missão, de modo a estudar os erros sistemáticos introduzidos por processos específicos de manipulação de imagens, comuns em astronomia. Usando agora apenas parte da amostra inicial de galáxias (10%), foram simuladas imagens às quais foram convoluídos modelos de PSF obtidos com o programa *PSFToolkit*, desenvolvido pela equipa de modelização de PSF da missão *Euclid*. O ruído aplicado pretendeu simular o efeito de deteção por CCD, com valores de ganho e ruído de leitura consistentes com o tipo de CCD da missão. Também a escala de pixel e o tempo de exposição foram tomados em consideração e definidos de acordo com o instrumento simulado.

Devido ao espaçamento existente entre CCDs, as observações feitas pela missão *Euclid* irão implementar o procedimento de *dithering*, onde a mesma região do céu é observada várias vezes, com pequenos deslocamentos, correspondentes à distância entre os detetores. Isto permitirá certificar que todo o campo de visão é observado e que nenhuma informação é perdida devido a este espaçamento. As imagens assim produzidas poderão ser adicionadas entre si (processo conhecido como *stacking*), aumentando a proporção de sinal-ruído, simulando uma imagem com maior tempo de exposição.

Nesta segunda parte do trabalho, as galáxias foram convoluídas com modelos de PSF, com o objetivo de estudar dois efeitos: o *bias* produzido pela variação da PSF *Euclid* ao longo do campo de visão; e os erros introduzidos na correção de imagens obtidas pelo procedimento de *dithering* e posterior *stacking* destas imagens. No primeiro caso, a variação das propriedades da PSF em diferentes pontos do campo de visão resultaram em distorções adicionais consistentes com o grau de elipticidade dos respetivos modelos de PSF. No estudo do efeito simultâneo de *dithering* e *stacking*, os valores de *bias* obtidos

foram comparados para diferentes correções de PSF. Especificamente, casos em que as imagens *stacked* foram corrigidas, não pela PSF verdadeira, mas por uma PSF efetiva, mostraram um aumento de erros sistemáticos quando comparados com casos em que esta correção foi feita usando a verdadeira PSF. Em ambos os efeitos estudados, os valores do termo aditivo de *bias* mostraram ser mais elevados do que o esperado, refletindo um efeito estatístico resultante da redução da amostra, em combinação com as propriedades de elipticidade intrínseca das galáxias e do resíduo do próprio método KSB.

O avanço da cosmologia observacional permitiu restringir os modelos cosmológicos aceites, limitando os valores possíveis de parâmetros cosmológicos, dos quais dependem esses modelos. No entanto, para além de limitações tecnológicas, a precisão na estimativa destes parâmetros depende igualmente da eficiência com que se calibram e removem efeitos como os aqui estudados. Deste modo, assumindo uma correção perfeita da componente aditiva do *bias* e tomando apenas o termo multiplicativo, foram propagados os erros sistemáticos encontrados na segunda parte, de forma a avaliar o impacto destes na estimativa de parâmetros cosmológicos (Ω_m e σ_8) diretamente relacionados com o fenómeno de *cosmic shear*.

Nesta parte final do trabalho verificou-se que uma variação, mesmo que pequena, nas características da PSF produz efeitos significativos no constrangimento destes parâmetros. Confirmou-se igualmente a importância do método de correção de imagens *stacked*, ao quantificar o erro introduzido na estimativa dos parâmetros mencionados e relacionando com o que seria a correção ideal. Os resultados obtidos permitem sugerir que tensões atualmente existentes em parâmetros cosmológicos medidos por diferentes experiências poderão ser devidas a erros sistemáticos, e não só a flutuações estatísticas.

O trabalho realizado nesta dissertação foi uma pequena contribuição para a quantificação do impacto que procedimentos comuns em astronomia poderão vir a ter em testes cosmológicos de elevada precisão, confirmando a necessidade de considerar o máximo de fatores externos ao fenómeno físico, de forma a atingir a precisão desejada.

Palavras-chave: lentes gravitacionais, simulação de imagens, efeitos sistemáticos; análise de dados; parâmetros cosmológicos.

Contents

Acknowledgments **iii**

Abstract **v**

Resumo **vii**

List of Tables **xiii**

List of Figures **xv**

1 Introduction **1**

2 Background **5**

2.1 Homogeneous Universe 5

2.1.1 Spacetime metric 5

2.1.2 Redshift and the Hubble parameter 6

2.1.3 Spacetime dynamics 6

2.2 Inhomogeneous Universe 7

2.2.1 Primordial density power spectrum 7

2.2.2 Cosmological parameters 9

2.3 Theory of gravitational lensing 9

2.3.1 Light deflection and the lens equation 9

2.3.2 Shear and convergence 11

2.4 Cosmological weak lensing 12

2.4.1 Convergence and shear fields produced by large-scale structure 12

2.4.2 Observing cosmic shear 13

2.4.3 Measuring cosmic shear: systematics 15

2.5 *Euclid* mission 16

2.5.1 *Euclid* in a nutshell 16

2.5.2 Biases in *Euclid* future data 16

3 Calibration tests **19**

3.1 *GalSim*: overview and capabilities 19

3.2 Methodology 23

3.2.1 Input galaxy sample properties 23

3.2.2 *GalSim* Configuration 24

3.2.3 Shape measurement: KSB method 25

3.2.4 Bias determination . . . 27
3.3 Results and Discussion . . . 27
3.3.1 T1 and T2: impact of shear variation in noiseless images . . . 27
3.3.2 T3 and T4: impact of shear and noise combination . . . 33

4 Simulating *Euclid* data **39**
4.1 Methodology . . . 39
4.1.1 Input galaxy sample reduction . . . 39
4.1.2 Dithering in *Euclid*'s observations . . . 40
4.1.3 *Euclid*'s PSF modelling . . . 41
4.1.4 GalSim general configuration . . . 43
4.2 Results and Discussion . . . 44
4.2.1 Case I: PSF variation along the field-of-view . . . 44
4.2.2 Cases II, IId, III, and IV: Bias resulting from image manipulation . . . 49

5 Impact of shear measurement biases on the constraints on cosmological parameters **51**
5.1 Cosmic shear as a cosmological probe . . . 51
5.2 Methodology . . . 53
5.2.1 The likelihood function . . . 53
5.2.2 *nicaea*: overview and configuration . . . 54
5.2.3 Biased correlation functions and parameters' space sampling . . . 55
5.3 Results and Discussion . . . 57
5.3.1 Impact from PSF variation . . . 57
5.3.2 Impact from image manipulation procedures . . . 58

6 Conclusions and Future Work **63**

Bibliography **67**

A *GalSim* configuration: Input shear values **73**

B Summary of results from calibration test sets **75**
B.1 Test sets T1 and T2 . . . 75
B.2 Test sets T3 and T4 . . . 76

C Summary of results from *Euclid* data simulations **79**
C.1 Case I: PSF variation along the field-of-view . . . 79
C.2 Cases II, IId, III, and IV: Bias resulting from image manipulation . . . 79

List of Tables

2.1 ΛCDM model parameters and 68%-confidence regions from CMB *Planck* and BAO data. 9

3.1 Summary of the main parameters in the *GalSim* configuration file. 23
3.2 Summary of parameter setup used in the different test sets. 25

4.1 Summary of ellipticity values for the PSF models. 43
4.2 Summary of *CCDnoise* parameters. 44

5.1 Summary of cosmological parameters set for the configuration of *nicaea*. 55
5.2 Results from biased model performance for PSF variation along the FoV. 58
5.3 Results from biased model performance for the different biased cases. 60

A.1 Input shear values. 73

B.1 Best-fit values for multiplicative and additive biases for each redshift bin for test sets T1 and T2. 75
B.2 Best-fit values for multiplicative and additive biases for each magnitude bin for test sets T1 and T2. 75
B.3 Best-fit values for multiplicative and additive biases for each half-light radius bin for test sets T1 and T2. 76
B.4 Best-fit values for multiplicative and additive biases for each redshift bin for test sets T3 and T4. 76
B.5 Best-fit values for multiplicative and additive biases for each magnitude bin for test sets T3 and T4. 76
B.6 Best-fit values for multiplicative and additive biases for each half-light radius bin for test sets T3 and T4. 77

C.1 Best-fit values for multiplicative and additive biases for each position in the field-of-view. 79
C.2 Best-fit values for multiplicative and additive biases for each considered case. 79

List of Figures

2.1 Gravitational lensing configuration in the thin-lens approximation. 10
2.2 Illustration of the effect of optical scalars on a circular object. 11
2.3 Illustration of the effect of individual ellipticity components. 14
2.4 Impact of instrument bias on weak gravitational lensing observations. 16

3.1 Example of simulated galaxy images using *GalSim*. 22
3.2 Example of simulated sheared galaxy images using *GalSim*. 22
3.3 Histograms of the normalised frequency of sample properties. 24
3.4 Histograms of the intrinsic ellipticity of the sources in the catalogue. 24
3.5 Monochromatic *Euclid*-like PSF. 25
3.6 Probability density functions of observed shear , PSF-corrected shear, and intrinsic ellipticity, for test set T1 and one realization of test set T2. 28
3.7 Combined results for the residual shear present in test sets T1 and T2 as a function of input shear signal. 29
3.8 Fitted values of multiplicative and additive biases for test sets T1 and T2. 29
3.9 Variation of multiplicative and additive biases as a function of redshift, for test sets T1 and T2. 30
3.10 Variation of multiplicative and additive biases as a function of magnitude, for test sets T1 and T2. 31
3.11 Variation of multiplicative and additive biases as a function of half-light radius, for test sets T1 and T2. 32
3.12 Illustration of correlations between galaxy properties, present in the filtered COSMOS catalogue. 32
3.13 Fitted values of multiplicative and additive biases for test sets T3 and T4. 33
3.14 Results of the residual shear present in test sets T3 and T4 for g_1. 34
3.15 Results of the residual shear present in test sets T3 and T4 for g_2. 34
3.16 Variation of multiplicative bias for test sets T3 and T4, as a function of redshift. 35
3.17 Variation of additive bias for test sets T3 and T4, as a function of redshift. 35
3.18 Variation of multiplicative bias for test sets T3 and T4, as a function of magnitude. . . . 36
3.19 Variation of additive bias for test sets T3 and T4, as a function of magnitude. 36
3.20 Variation of multiplicative bias for test sets T3 and T4, as a function of half-light radius. 37
3.21 Variation of additive bias for test sets T3 and T4, as a function of half-light radius. 37

4.1 Comparison of the distribution of redshift, magnitude, and half-light radius between the COSMOS catalogue and the reduced sample. 40

4.2 Comparison of intrinsic ellipticity between the COSMOS catalogue and the reduced sample. . . . 40
4.3 Coverage of the VIS field-of-view, and dither pattern. . . . 41
4.4 Plots of *Euclid*'s PSF ellipticity variation along the FoV. . . . 42
4.5 Model of *Euclid*'s PSF for each chosen point in the FoV. . . . 43
4.6 Illustration of the procedures used to simulate different image manipulation conditions. . . . 45
4.7 Results of the residual shear for one position of the FoV. . . . 46
4.8 Variation of multiplicative and additive biases as a function of redshift, magnitude, and half-light radius, in one position of the FoV. . . . 47
4.9 Results of the residual shear as a function of input shear signal, for PSF variation along the FoV. . . . 48
4.10 Fitted values of multiplicative and additive biases for each position in the field-of-view. . . . 48
4.11 Results of the residual shear as a function of input shear signal, for cases I (P6) to IV. . . . 49
4.12 Fitted values of multiplicative and additive biases for cases I (P6) to IV. . . . 49

5.1 Confidence level contours in the Ω_m - σ_8 plane from the analysis of different cosmological probes. . . . 52
5.2 Marginalised posterior distributions in the $\Omega_m - \sigma_8$ plane for different points in the FoV. 57
5.3 Marginalised posterior distributions in the $\Omega_m - \sigma_8$ plane for the different case comparisons. 59
5.4 Marginalised posterior distributions in the $\Omega_m - \sigma_8$ plane for case I (P6) marginalised over the multiplicative bias. . . . 61

Chapter 1

Introduction

In our world, matter is not distributed uniformly but rather concentrated in single celestial bodies which are not at rest but rather in relative motion (slow when compared to the velocity of light). But it is very well possible that the mean ("measured naturally") spatial density of matter, taken for spaces which contain many fixed stars, is an almost constant quantity in the universe. In that case, the equations must be amended with an additional term with the character of our λ-term. The universe then must be closed in itself, and its geometry deviates from that of a spherical or elliptical space only little, and only locally, as, for example, the shape of the earth's surface deviates from that of an ellipsoid. - A. Einstein [1].

In 1917, Albert Einstein formulated the Theory of General Relativity to include the cosmological constant that would modify the solutions to his field equations, so as to describe the Universe as a closed, quasi-static, and essentially homogeneous distribution of mass [2]. However, not long after this formulation, in 1927, Georges Lemaître predicted that the Universe might in fact be expanding at a constant rate [3], as opposed to this static hypothesis. Then, two years later, Edwin Hubble made redshift observations of nearby galaxies that indicated that these objects were receding at increasingly large velocities [4], with his measurements becoming the basis for the concept of an expanding Universe, and defining the expansion rate as the Hubble constant. Afterwards, the λ term introduced by Einstein was disregarded by himself, and removed from the equations.

The following decades witnessed the birth and establishment of the Big Bang theory. While the notion of a *primeval atom*, from which the Universe came into existence, was first presented by Lemaître in 1931 [5], it was only after World War II that George Gamow attempted to explain the origin of chemical elements through primordial nucleosynthesis, by considering the earlier stages of the Universe to be dominated by radiation instead of matter. Later on, Gamow's associates, Ralph Alpher and Robert Herman, predicted the existence of a diffuse background of blackbody radiation, with a temperature of around $5K$, that would be observed today as a remnant of this early hot stage of the Universe [6]. Confirmation of this prediction came in 1965 with the detection of this cosmological microwave background radiation (CMB) by Arno Penzias and Robert Wilson [7]. By now there were enough arguments to establish the Big Bang theory as the most accepted cosmological model, and so it became the standard explanation for the origin and evolution of the Universe.

After defining the Big Bang theory as the standard cosmological model, physicists were able to focus on how structures were formed and evolved, making the remainder of the 1960s, as well as the following decade, rich in publications around density perturbation models [8–11]. These aimed to explain how structures in the Universe, such as galaxies, and galaxy clusters, could have grown from gravitational interactions in the large-scale matter distribution, described as fluctuations from an isotropic and homogeneous density field. Eventually, the relation found between the primordial density fluctuations and

the temperature variations in the CMB [8], in conjunction with increasingly sensitive observations, allowed the constraint of parameters in structure formation models and the subsequent narrowing down of possible models.

In the beginning of the 1980s, however, it became apparent that the measured amplitude for these primordial density fluctuations was in conflict with the estimated amount of existent baryonic matter. The solution came in the form of cold dark matter (CDM), which would only interact gravitationally relative to baryonic matter, allowing structures to form while maintaining small amplitude perturbations during the early stages of the Universe [12]. Such a model included an underlying bias in the distribution of baryonic matter relative to CDM, thus defining the distribution of galaxies on large scales.

Dark matter would be considered the dominant component up until the end of the twentieth century and the beginning of the twenty-first, when the discovery of an acceleration in the expansion of the Universe revealed the need for another component, now designated as dark energy, which affects not only the expansion velocity, but also structure formation. Results from the Wilkinson Microwave Anisotropy Probe (WMAP) [13] in combination with large-scale galaxy surveys, allowed the determination, with increased precision, of the large-scale geometry of the Universe and values for the density parameters of all components, which indicated dark energy to be the dominant component today. In fact, the effects of dark energy can be interpreted as Einstein's cosmological constant with a positive value, resulting in this term begin reintroduced in the field equations. Therefore, the reformulation of the standard cosmological model to include dark energy became known as the ΛCDM model. In Einstein's own words in correspondence to William de Sitter: *In any case, one thing stands. The general theory of relativity allows the addition of the term $\lambda g_{\mu\nu}$ in the field equations. One day, our actual knowledge of the composition of the fixed-star sky, the apparent motions of fixed stars, and the position of spectral lines as a function of distance, will probably have come far enough for us to be able to decide empirically the question of whether or not λ vanishes. Conviction is a good mainspring, but a bad judge!* [14].

As is clear from the scientific events presented so far, the importance of cosmology as a physical science has increased significantly in the last century. With constant technological advances, this mainly theoretical field is being transformed into an increasingly observational science. This evolution has resulted in the current understanding of the Universe now being described by the concordance model, a modification of ΛCDM that includes the phenomenon of inflation, responsible for solving some of the issues remaining from previous descriptions of the Universe. The concordance model is a product of decades of knowledge, built by the joint contributions of mathematical predictions and observational data. Therefore, the importance of observational cosmology lies greatly in providing information used to empirically constrain the values of cosmological parameters, on which cosmological models, such as the concordance model, are based.

Some of the major scientific breakthroughs achieved in the twenty-first century can be attributed to Astronomy, with well-known examples being the first detection of gravitational waves in 2016 [15] and the direct observation of the event horizon of a black hole in 2019 [16]. In particular, one of the most important scientific contributions from Cosmology is the very well-documented observation of gravitational lensing phenomena. As predicted by Einstein's theory of General Relativity, the presence of matter deflects the propagation of light (gravitational lensing), with this deflection being not only an indirect indicator of the presence of dark matter but also a probe of the evolution of dark energy, thus becoming a useful tool in understanding the nature of these two components.

Gravitational lensing can be divided into strong and weak lensing [17], depending, amongst other factors, on the strength of the distortions to the trajectory of light. Lensing, as a probe of the dark matter distribution, relies on the detection of the very subtle effect of cosmic shear. This effect is translated into

a cumulative distortion in observed galaxy shapes, as a result of light from the source being deflected along its path through the large-scale matter distribution. It is therefore a weak gravitational lensing phenomenon, where the distortion is added to the galaxy's own intrinsic ellipticity. Since the shape of the source is unknown, the cosmic shear signal can only be statistically detected through the observation of a large number of sources, assuming galaxies to be randomly oriented in the sky.

Due to the very small impact of cosmic shear on the overall galaxy shape, this quantity is bound to be strongly affected by systematic and spurious errors occurring during data acquisition and subsequent processing, in particular due to the optical effects of the telescope's point-spread function (PSF). Constant improvement in instrument sensitivity allows the determination of cosmological parameters with increasing precision, but this must be accompanied by an increasingly accurate correction of any distortions additional to the lensing signal, at the risk of introducing biases to these measurements. A future generation of cosmological surveys, such as *Euclid*[1], will have very low tolerance to systematic errors in order to fulfil the mission's goals, making the process of bias correction even more crucial.

The objective of this thesis is precisely to quantify multiplicative and additive biases introduced by common image manipulation steps used in astronomical data, to model their effects on the final cosmic shear measurements, and to propagate their impact into the estimation of cosmological parameters. The applied procedure follows a methodology similar to that of preceding works that evaluated bias in weak lensing measurements [18–21], while focusing on simulating realistic galaxy images with *Euclid*-like conditions. This work studies the impact of bias due to several factors: *Euclid*'s PSF variation along the field-of-view; variations in the applied noise model; and variations resulting from image manipulation processes, such as dithering of individual exposures and posterior stacking of these dithered images. This study also quantifies how different choices of PSF correction may impact the biased measurements, in light of a specific PSF-correcting algorithm.

The work here presented is part of the Enabling Weak lensing Cosmology (EWC) project funded by the H2020 European Programme, of which the University of Lisbon is a participating node[2], collaborating closely with two of the other nodes (University of Bonn and Astronomical Observatory of Rome). The EWC project is a collaboration among scientists from around the world, embedded in the *Euclid* Consortium, and consists of preparatory work that will be used to characterise biases affecting future *Euclid* data.

This thesis is divided into five parts. Chapter 2 reviews baseline cosmological concepts, necessary to better understand the weak lensing phenomenon, and summarises *Euclid*'s calibration challenges. Chapter 3 describes the software used to simulate galaxy images, the applied methodology, and the results of the first calibration tests. Chapter 4 incorporates *Euclid*'s observing conditions into the simulated galaxy images and analyses the bias introduced by its PSF variation across the FoV, as well as from dithering, and stacking processes. Chapter 5 analyses the impact of the bias found in Chapter 4 on the estimation of cosmological parameters. Finally, Chapter 6 summarises the conclusions from the analysis presented in the previous chapters, suggesting future work that can be done to improve these results and exploring additional effects that could introduce bias in cosmic shear measurements.

Analyses such as these are key when calibrating future *Euclid* observations against variations in the image-production procedure, and must be carried out in order to increase precision in the final measurements. With this in mind, it is the aim of this thesis to make a humble contribution to this challenging step of weak lensing data calibration.

[1] `https://www.euclid-ec.org/`

[2] `https://weaklensing-cosmology.org/`

Chapter 2

Background

Since the phenomenon of cosmic shear is the basis of this work, the present chapter reviews important baseline concepts of cosmology that are necessary to understand the origin and impact of weak gravitational lensing due to large scale structure. A more in-depth description of the observation and measurement of cosmic shear is given, emphasizing the susceptibility of this quantity to biases introduced during data acquisition and handling. At the end of this chapter, a brief summary on *Euclid*'s mission characteristics is presented, as well as some of the calibration challenges associated with this particular space mission.

2.1 Homogeneous Universe

Most aspects of our current understanding of the Universe are described by the concordance cosmological model. Its fundamental pillars are the cosmological principle and the field equations given by General Relativity, and it describes the components of the Universe as fluids, quantifying their effect on cosmic expansion. This section consists of a brief overview of basic cosmological definitions in light of this particular model.

2.1.1 Spacetime metric

Spacetime, as defined by General Relativity, is a four-dimensional manifold, with properties that are affected by the presence of matter. In this definition, two events with coordinates x^μ are separated by a line element ds, with a local geometry described by

$$ds^2 = g_{\mu\nu} dx^\mu dx^\nu, \tag{2.1}$$

where $g_{\mu\nu}$ is the metric tensor. Coordinate indices range from 0 to 3, with $\mu = 0$ representing the time coordinate and $\mu = 1, 2, 3$ corresponding to the three spatial coordinates. Fundamental to the concordance model, the cosmological principle states that the Universe should be described by a homogeneous and isotropic matter distribution when observed on large scales. These two requirements constrain the range of allowed metric representations, with the most general case being given by the spherically symmetric Friedmann-Lemaître-Robertson-Walker (FLRW) metric:

$$ds^2 = -cdt^2 + a^2(t)[d\omega^2 + f_K^2(\omega)(d\theta^2 + sin^2\theta d\phi^2)]. \tag{2.2}$$

In the equation above, the expansion of spacetime is embedded in the scale factor $a(t)$, which can

assume values between 0 (corresponding to a singularity at the time of the Big Bang) and a_0 (current time). Here, c is the speed of light, ω represents the comoving radial coordinate, and $f_K(\omega)$ is the comoving radius of the sphere, which depends on the spatial curvature, K, as defined in Eq. (2.3) [22].

$$f_K(\omega) = \begin{cases} K^{-1/2} sin(K^{1/2}\omega) & (K > 0 : spherical) \\ \omega & (K = 0 : flat) \\ (-K)^{-1/2} sinh[(-K)^{-1/2}\omega] & (K < 0 : hyperbolic) \end{cases} . \tag{2.3}$$

Comoving quantities are not affected by the expansion of the Universe, but are fixed in the expanding reference frame. In Eq. (2.3), $spherical$, $flat$, and $hyperbolic$ correspond to the geometries associated with each spatial curvature value.

2.1.2 Redshift and the Hubble parameter

Due to the expansion of the Universe, photon wavelength λ increases as photons follow their path through spacetime from the emitting source to the observer. This change is quantified by the redshift factor, written as either a function of wavelength or of the scale factor:

$$z = \frac{\lambda_{observed}}{\lambda_{emitted}} - 1 = \frac{a(t_0)}{a(t)} - 1. \tag{2.4}$$

In 1929, Edwin Hubble published the correlation between measured distances to nearby galaxies and the corresponding redshifts – later known as Hubble-Lemaître law [3, 4] – which showed that objects at greater distances r were receding at higher velocities v, with a proportionality factor of H_0 defined as the Hubble constant. Generalising beyond the nearby Universe, this law becomes:

$$\mathbf{v}(t) = H(t)\mathbf{r}(t), \tag{2.5}$$

where the proportionality term is now the Hubble function, representing the relative expansion rate

$$H(t) = \frac{\dot{a}(t)}{a(t)}. \tag{2.6}$$

The particular case of $H_0 = H(t_0)$ corresponds to the Hubble parameter, with a measured value of $H_0 = (67.4 \pm 0.5)\ \mathrm{km\ s^{-1}\ Mpc^{-1}}$ [23].

2.1.3 Spacetime dynamics

The way that the content in the Universe affects spacetime geometry can be described through Einstein's field equations,

$$G_{\mu\nu} = \frac{8\pi G}{c^4} T_{\mu\nu} - \Lambda g_{\mu\nu}, \tag{2.7}$$

in combination with a spacetime metric $g_{\mu\nu}$, such as the one in Eq. (2.2). Here, $G_{\mu\nu}$ is the Einstein tensor, $T_{\mu\nu}$ represents the stress-energy tensor of the cosmological fluid, and Λ is the cosmological constant. In a homogeneous and isotropic Universe described by $g_{\mu\nu}$, Einstein's field equations yield a solution for the evolution of the scale factor in the form of two independent equations [24], namely the Friedman

equation and the acceleration equation, given respectively by:

$$H^2 = \left(\frac{\dot{a}}{a}\right)^2 = \frac{8\pi G}{3}\rho - \frac{Kc^2}{a^2} + \frac{\Lambda c^2}{3}, \tag{2.8}$$

$$\frac{\ddot{a}}{a} = -\frac{4}{3}\pi G\left(\rho + \frac{3p}{c^2}\right) + \frac{\Lambda c^2}{3}. \tag{2.9}$$

Solutions to Eqs. (2.8) and (2.9) depend on the values of total density, geometry, and Λ in the considered model, with Eq. (2.9) allowing for the definition of an equation of state of the form:

$$\mathrm{w}_i = \frac{p_i}{\rho_i c^2}, \tag{2.10}$$

relating the energy density, ρ, and pressure, p, of each component of the cosmological fluid. Assuming a Universe containing radiation, matter, curvature, and dark energy, the Friedmann equation in Eq. (2.8) can be rewritten as

$$H^2 = H_0^2\left[\frac{\Omega_r}{a^4} + \frac{\Omega_m}{a^3} + \frac{\Omega_K}{a^2} + \Omega_\Lambda\right], \tag{2.11}$$

where Ω_i ($i = r, m, K, \Lambda$) correspond to the density contributions of each component to the total density of the cosmological fluid, Ω, which by construction will sum to one. Values for some of these parameters are summarised in Table 2.1, showing the current estimates for these components in the Universe. Given the different evolution of the energy densities with the four-dimensional volume, different components may dominate over others in driving the spacetime dynamics at different times.

2.2 Inhomogeneous Universe

While at large scales the Universe may be considered homogeneous and isotropic, at smaller scales it appears highly inhomogeneous, showing an intricate distribution of hierarchical structures in the form of galaxies, clusters of galaxies, and filaments. These local inhomogeneities can be studied, at first approximation, through linear perturbation theory.

2.2.1 Primordial density power spectrum

The complex systems observed today are thought to have started as small inhomogeneities in the on-average homogeneous primordial fluid. These inhomogeneities are thought to have been generated by small quantum fluctuations at the time of inflation, creating density gradients in the homogeneous and isotropic self-gravitating fluid. As such, regions where density was slightly higher than the average global value caused an excess attraction and the consequent infall of surrounding material; conversely, lower-density regions lost mass to higher-density regions. As a result, density fluctuations became amplified over time and led to the formation of structures.

Energy density perturbations may be written as the sum of a background, unperturbed value, and a deviation from the global average [25]:

$$\rho(t, \mathbf{x}) = \bar{\rho}(t)(1 + \delta(t, \mathbf{x})), \tag{2.12}$$

where $\bar{\rho}$ is the mean density, and δ is defined as the dimensionless density contrast, representing the variation from the global mean value, and dependent on both time and the three dimensional space coordinate. Since the exact distribution of the density contrast as a function of position is unknown,

predictions of its spatial properties can only be made through a statistical approach. The density contrast field is assumed to behave as a random field, characterised by a probability distribution function, and thus invariant under both rotation and translation [26]. Similarly to the density field, other quantities can be used to characterise the inhomogeneous Universe such as pressure, velocity, and gravitational potential, when written in their perturbed form, as in Eq. (2.12).

A Gaussian primordial density field will be completely described by its first and second-order moments, particularly the two-point correlation function, ξ, written as:

$$\xi(r) = \langle \delta(\mathbf{x}) \delta^*(\mathbf{x} + \mathbf{r}) \rangle, \tag{2.13}$$

where the angled brackets represent averages over an ensemble of possible realizations of the density field, with the limitation that at large-scales there is only one available Universe to study, and thus only one possible realization. As a result of its invariance under the mentioned transformations, this correlation function will only depend on the three dimensional distance $r = |x - x'|$ between two positions.

In order to compute ξ, it is useful to rewrite the density contrast field by expanding it in its Fourier modes as given by:

$$\delta_{\mathbf{k}}(\mathbf{k}, t) = \int d^3\mathbf{x}\, \delta(\mathbf{x}, t) e^{i\mathbf{k}\cdot\mathbf{x}}, \tag{2.14}$$

where the comoving wave vector is defined as $|\vec{k}| = 2\pi/\lambda$. The two-point correlation function in Fourier space is then [27]:

$$\xi(\mathbf{x}, t) = \langle \delta_{\mathbf{k}} \delta^*_{\mathbf{k}'} \rangle = \left\langle \int d^3\mathbf{x}\, \delta(\mathbf{x}, t) e^{i\mathbf{k}\cdot\mathbf{x}} \int d^3\mathbf{x}'\, \delta(\mathbf{x}', t) e^{-i\mathbf{k}'\cdot\mathbf{x}'} \right\rangle = (2\pi)^3 \delta_D(\mathbf{k} - \mathbf{k}') P_\delta(k). \tag{2.15}$$

which introduces P_δ, the power spectrum of the density perturbations, defined as the Fourier transform of the correlation function

$$\xi(\mathbf{x}) = \frac{1}{(2\pi)^3} \int d^3\mathbf{k}\, P_\delta(k) e^{-i\mathbf{k}\cdot\mathbf{x}}. \tag{2.16}$$

Note also that δ_D is the Dirac's delta.

Most models of inflation favour density perturbations in adiabatic form [26], with a Gaussian probability distribution, and a primordial density power spectrum, $P_\delta(k)$, well described by a power law,

$$P_\delta(k) = A k^{n_s}, \tag{2.17}$$

where n_s is defined as the spectral index of scalar perturbations. In its dimensionless form, the matter power spectrum relates to the amplitude of density perturbations in each scale k as follows:

$$\Delta^2(k) \propto k^3 P_\delta, \tag{2.18}$$

Since the initial amplitude is unknown, it is necessary to normalise the power spectrum. This is usually done by defining the σ_8 parameter, which corresponds to the amplitude of the power spectrum today, at the scale of $R = 8\ h^{-1}\mathrm{Mpc}$.

It is therefore possible to study the inhomogeneous Universe by making use of the information obtained through the power spectrum of specific perturbed quantities, such as the density contrast field. In particular, the relation between matter distribution at large scales and the respective matter power spectrum can be explored through the measurement of observables associated with this quantity, with the

information thus obtained serving as motivation for future missions.

2.2.2 Cosmological parameters

Measurements of the power spectrum are done through observational cosmology, and such measurements are used to constrain cosmological parameters of the current cosmological model. Some of these parameters have already been introduced, and their current values are presented in Table 2.1. These were obtained from the combination of *Planck* Collaboration measurements [23] of CMB anisotropies, with information gathered from temperature and polarization maps, as well as from CMB lensing reconstruction. The current estimates are consistent with a spatially-flat ΛCDM cosmology with purely adiabatic, Gaussian initial fluctuations.

Future missions, such as *Euclid*, will provide highly reliable measurements of dark energy related parameters. Since the theoretical prediction, as given by quantum field theory, for the amount of dark energy is much higher than what is estimated by observations, *Euclid* data may either confirm the concordance model as the standard explanation for the origin and evolution of the Universe, or impose a revision on the current theory of gravity. This data can also be used to break existing parameter degeneracies when combined with CMB data.

Table 2.1: Best-fit ΛCDM model parameters and 68%-confidence regions, obtained from the combination of the full CMB *Planck* data and BAO data (Baryonic Acoustic Oscillations) [23].

Ω_m	0.3111 ± 0.0056
Ω_Λ	0.6889 ± 0.0056
H_0	67.66 ± 0.42 km s^{-1}Mpc^{-1}
σ_8	0.8102 ± 0.0060
n_s	0.9665 ± 0.0038
w_0	-1.03 ± 0.03

2.3 Theory of gravitational lensing

2.3.1 Light deflection and the lens equation

As implied by General Relativity, the distribution of mass in the Universe affects the propagation of light. This occurs due to light following the curvature of spacetime, which is the expression of the gravitational field created by the presence of matter. The result is that light from other galaxies is deflected in its path towards Earth, and the impact on observed images will depend on the size of the mass distribution acting as a lens between source and observer. This effect is called gravitational lensing.

The deflection of light due to gravitational lensing can be analysed geometrically using the thin-lens approximation, assuming that the lens size is much smaller than the distances between the source and lens, and the distance between the lens and observer [26]. As shown in Fig. 2.1, a light ray emitted from an object in the source plane, at a two-dimensional angular position $\boldsymbol{\beta}$, is deflected by an angle $\hat{\boldsymbol{\alpha}}$ due to the presence of matter in the lens plane. The image of this source will be seen in a virtual image plane at an angular position $\boldsymbol{\theta}$.

The relation between the source and image distances to the optical axis, projected onto the source plane, can be obtained through trigonometry and is given by:

$$D_s\boldsymbol{\beta} = D_s\boldsymbol{\theta} - D_{ds}\hat{\boldsymbol{\alpha}}, \tag{2.19}$$

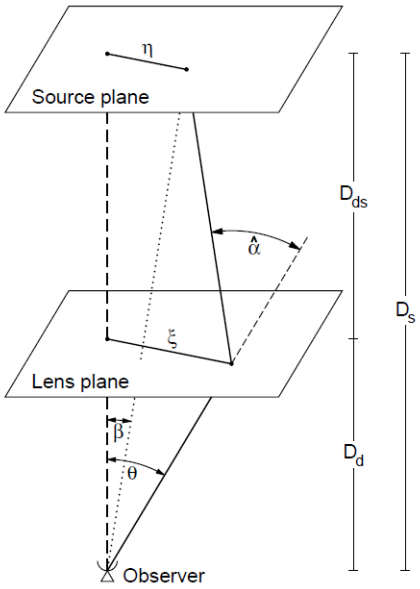

Figure 2.1: Gravitational lensing configuration in the thin-lens approximation. Adapted from Ref. [26].

where $D_s\boldsymbol{\theta}$ is the projected distance of the image to the centre of the source plane, $D_s\boldsymbol{\beta}$ is the distance of the source relative to the optical axis, and $D_{ds}\hat{\boldsymbol{\alpha}}$ is the excess distance created by the lens [26]. Defining the scaled deflection angle as: $\boldsymbol{\alpha}(\boldsymbol{\theta}) = \frac{D_{ds}}{D_s}\hat{\boldsymbol{\alpha}}(D_d\boldsymbol{\theta})$, the lens equation becomes:

$$\boldsymbol{\beta} = \boldsymbol{\theta} - \boldsymbol{\alpha}. \tag{2.20}$$

Assuming galaxies as extended sources of small angular size, Eq. (2.20) can be linearised as follows:

$$\boldsymbol{\beta}(\boldsymbol{\theta}) = \boldsymbol{\beta}(\boldsymbol{\theta_0}) + \boldsymbol{A}(\boldsymbol{\theta_0})(\boldsymbol{\theta} - \boldsymbol{\theta_0}), \tag{2.21}$$

where $\boldsymbol{\beta_0}$ and $\boldsymbol{\theta_0}$ are the central positions of source and image, respectively, and $\boldsymbol{A}$ is called the amplification matrix, responsible for describing the lensing transformation between the source and lens planes.

As a general distortion matrix, $\boldsymbol{A}$ can be decomposed into a linear combination of a symmetrical traceless matrix, an antisymmetrical matrix and a trace, as given by Eq. (2.22).

$$\boldsymbol{A} = \begin{bmatrix} \sigma_1 & \sigma_2 \\ \sigma_2 & -\sigma_1 \end{bmatrix} + \begin{bmatrix} 0 & \omega \\ -\omega & 0 \end{bmatrix} + \begin{bmatrix} \frac{\Theta}{2} & 0 \\ 0 & \frac{\Theta}{2} \end{bmatrix}. \tag{2.22}$$

These matrices represent fundamental distortions occurring in the image in the form of shear (σ_1, σ_2), vorticity ω, and expansion Θ, also known as optical scalars [26], illustrated in Fig. 2.2.

The phenomenon of gravitational lensing can be divided in two regimes: strong and weak lensing. Strong lensing occurs near the source-lens-observer line of alignment, and in regions of density perturbations with large amplitude. This regime is characterised by strong distortions to the galaxy shape, such as a change in apparent position, and source magnification. Analogously, weak lensing is detected when observing further away from the line of alignment, and in regions of smaller amplitude fluctuations. Here the distortions are less pronounced, resulting in a small increase in galaxy ellipticity [26]. In both regimes, the lens can be either luminous or dark matter, allowing the possibility of probing the matter distribution, regardless of its nature. Being a gravitational effect implies that it is independent of the lens luminosity, involving no emission or absorption of photons, and therefore not affecting the frequency

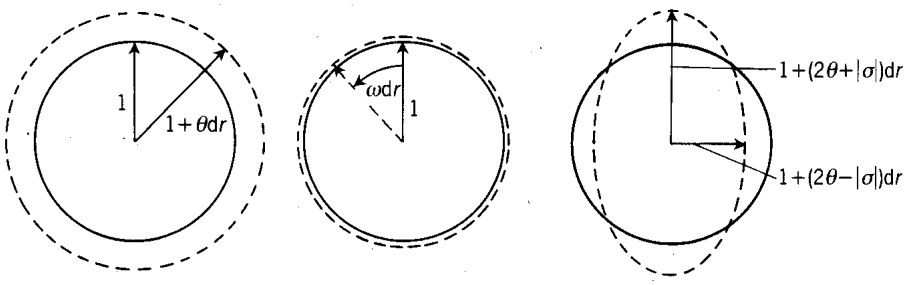

Figure 2.2: Illustration of the effect of optical scalars on a circular object. From left to right: expansion, vorticity, and shear. Reproduced from Ref. [28].

of light from the source to the image. The last two properties imply surface brightness conservation, so that when magnification occurs, flux also increases [26], thus providing a useful tool for observing faint sources.

2.3.2 Shear and convergence

Gravitational lensing can be treated as an effect resulting from a combination of lenses, each contributing differently to the overall deflection of the light path. This results in the definition of an effective deflection potential [27]

$$\psi(\boldsymbol{\theta}, \chi) = \frac{2}{c^2} \int_0^{\chi} d\chi' \frac{f_K(\chi - \chi')}{f_K(\chi)} f_K(\chi') \Phi(f_K \theta, \chi'), \tag{2.23}$$

representing the sum of contributions from all deflection potentials Φ along the line-of-sight, weighted by a lensing kernel that is a function of the comoving distances to the source (χ) and lenses (χ').

By considering Eq. (2.20), and introducing the Jacobian $\boldsymbol{A} = \partial\boldsymbol{\beta}/\partial\boldsymbol{\theta}$, the amplification matrix can be written in the form [27]:

$$A_{ij}(\boldsymbol{\theta}, \chi) = \delta_{ij} - \partial_i \partial_j \psi(\boldsymbol{\theta}, \chi), \qquad i, j = 1, 2. \tag{2.24}$$

Therefore, the optical scalars defined in Eq. (2.22) can be obtained by computing second-order derivatives of this potential. Since the matrix is symmetrical, the vorticity is zero, implying that gravitational lensing produces no rotation:

$$\omega = 0. \tag{2.25}$$

The expansion is given by the trace $\Theta = 2 - (\partial_1\partial_1\psi + \partial_2\partial_2\psi)$, from which results the definition of the convergence κ:

$$\kappa = 1 - \frac{\Theta}{2} = \frac{1}{2}(\partial_1\partial_1\psi + \partial_2\partial_2\psi). \tag{2.26}$$

Finally, the two-component shear, defined in Eq. (2.22) as (σ_1, σ_2), can be redefined as:

$$\gamma_{ij} = -\sigma_{ij} \Rightarrow \gamma_1 = \frac{1}{2}(\partial_1\partial_1\psi - \partial_2\partial_2\psi), \gamma_2 = \partial_1\partial_2\psi, \tag{2.27}$$

or in the form of a complex number $\gamma = \gamma_1 + i\gamma_2 = |\gamma| \exp(2i\phi)$.

Since convergence is a scalar quantity, it is responsible for an isotropic distortion affecting the size of the observed object. Shear, on the other hand, has an effect on the shape of the object, by contributing with an anisotropic distortion. Introducing the above definitions in the amplification matrix, it can be

parametrised as follows:

$$A = \begin{bmatrix} 1-\kappa-\gamma_1 & \gamma_2 \\ -\gamma_2 & 1-\kappa+\gamma_1 \end{bmatrix}. \tag{2.28}$$

Since the lens equation describes the transformation between source and image, the magnification parameter is in turn defined as:

$$\mu = \frac{1}{\mathrm{detA}} = \frac{1}{(1-\kappa)^2 - |\gamma|^2} = \frac{1}{(1-\kappa)^2(1-g^2)}, \tag{2.29}$$

where g is the reduced shear, given by $g_i = \gamma_i/(1-\kappa)$.

2.4 Cosmological weak lensing

As described in previous sections, fluctuations in the primordial density field have grown to become large-scale structures that act as a lens system deflecting light paths between the emitting sources and the observer. In the particular case of gravitational lensing due to the presence of the large-scale matter distribution, this manifests as a cosmological effect known as cosmic shear.

2.4.1 Convergence and shear fields produced by large-scale structure

As the impact of weak gravitational lensing by large-scale structure is characterised by both the convergence and shear fields, it is therefore characterised by their respective power spectra.

Taking the shear correlation function to be:

$$\xi_\gamma(\vartheta) = \langle |\gamma|(\boldsymbol{\theta})|\gamma|^*(\boldsymbol{\theta'})\rangle, \tag{2.30}$$

where $\vartheta = |\boldsymbol{\theta} - \boldsymbol{\theta'}|$ is the separation between two points in the sky. This correlation can also be evaluated for the individual components of shear, which are usually combined as:

$$\xi_+ = \xi_{11} + \xi_{22};\ \xi_- = \xi_{11} - \xi_{22};\ \xi_\times = \xi_{12} = 0, \tag{2.31}$$

where $\xi_{ij}(\vartheta) = \langle \gamma_i(\boldsymbol{\theta})\gamma_j^*(\boldsymbol{\theta'})\rangle$, with $i, j = 1, 2$. Then the power spectrum of the shear field P_γ can be obtained with a Fourier transform:

$$(2\pi)^2\delta_D(\boldsymbol{\ell} - \boldsymbol{\ell'})P_\gamma(\boldsymbol{\ell}) = \langle \tilde{\gamma}(\boldsymbol{\ell})\tilde{\gamma}^*(\boldsymbol{\ell'})\rangle, \tag{2.32}$$

where $\boldsymbol{l}$ is the two-dimensional wave vector. Since both the convergence and shear are derived from the lensing potential (Eq. 2.23), it can be shown that their power spectra are related through [26]:

$$\langle \tilde{\gamma}(\boldsymbol{\ell})\tilde{\gamma}^*(\boldsymbol{\ell'})\rangle = \frac{(\ell_1^2 - \ell_2^2 + 2i\ell_1\ell_2)(\ell_1^2 - \ell_2^2 - 2i\ell_1\ell_2)}{\ell^4}\langle \tilde{\kappa}(\boldsymbol{\ell})\tilde{\kappa}^*(\boldsymbol{\ell'})\rangle = \langle \tilde{\kappa}(\boldsymbol{\ell})\tilde{\kappa}^*(\boldsymbol{\ell'})\rangle, \tag{2.33}$$

which implies that the power spectra of the convergence and shear are identical ($P_\kappa = P_\gamma$).

Since the convergence is the Laplacian of the effective lensing potential (see Eq. (2.26)), the convergence field is associated with the mass of the lens through the Poisson equation, thus being related to the matter power spectrum P_δ [26]. Therefore the explicit dependency of P_γ on the density power spectrum

can be written as

$$P_\gamma(\ell) = \frac{9}{4}\left(\frac{H_0}{c}\right)^4 \Omega_{m,0}^2 \int_0^{w_H} dw \frac{\overline{W}^2(w)}{a^2(w)} P_\delta\left(\frac{\ell}{f_K(w)}, w\right). \tag{2.34}$$

Here, the upper integration boundary w_H represents the horizon distance. The weighting function $\overline{W}(w)$ is defined by

$$\overline{W}(w) \equiv \int_w^{w_H} dw' G(w') \frac{f_K(w'-w)}{f_K(w')}, \tag{2.35}$$

where $G(w')$ is the normalised source distance distribution, with $dw'G(w') = p_z(z)dz$ corresponding to the normalised source redshift distribution. This dependence of P_δ on source redshift shows the importance of accurately determining the redshift distribution of the sources being observed. The result in Eq. (2.34) reveals a correlation between mass in large-scale structures and the shear power spectrum, suggesting that there is a way to probe the matter distribution through the observed shear field. Therefore, properties of both the convergence and shear fields will depend on the measured values of fundamental cosmological parameters.

The observable shear correlation functions, written in Eq. (2.31), are Fourier transforms of the shear power spectrum. Integrating the isotropic angular part, the relations are

$$\xi_+ = \int \frac{d\ell}{2\pi} \ell P_\gamma(\ell) J_0(\ell\theta); \qquad \xi_- = \int \frac{d\ell}{2\pi} \ell P_\gamma(\ell) J_4(\ell\theta), \tag{2.36}$$

where J_n ($n = 0, 4$) is the Bessel function defined as $J_n(x) = \frac{1}{2\pi}\int_{-\pi}^{\pi} d\phi e^{i(n\phi - xsin(\phi))}$. Hence the shear correlation functions can be computed from the shear power spectrum, which in turn can be computed from the matter density power spectrum, according to Eq. (2.34).

2.4.2 Observing cosmic shear

As described in Section 2.3.1, matter acting as a gravitational lens deflects light crossing through the matter distribution. In the case of cosmic shear, this effect will result in a coherent alignment of galaxy image orientations, which can only be detected by measuring the correlation of shapes between galaxy pairs in an image. Due to the distortion being so small, it will not be detected in individual galaxies, but only by observing a large number of objects, making it a statistical effect. This means that it will be described by both the convergence and the shear fields, and their respective power spectra. Since the shear field cannot be measured directly from observations, it must be associated with an observable, or shear estimator, in this case defined as the ellipticity of observed sources.

As galaxies are seen as 2-dimensional objects, their shape can be parametrised by two quantities, the eccentricity $|e|$ and the orientation ϕ, such that the ellipticity associated with each object is then:

$$e = |e| \exp(2i\phi) = e_+ + ie_\times. \tag{2.37}$$

The individual components measure the excess flux along the x-axis with respect to the flux along the y-axis (e_+), and the excess flux along the $y = x$ line with respect to the $y = -x$ line ($e_\times$). As seen in Fig. 2.3, the absolute value of e ranges from 0, corresponding to a perfect circle, to 1.

In practice, the ellipticity of an object, as defined in

$$e = \frac{Q_{11} - Q_{22} + 2iQ_{12}}{Q_{11} + Q_{22} + 2(Q_{11}Q_{22} - Q_{12}^2)^{1/2}}, \tag{2.38}$$

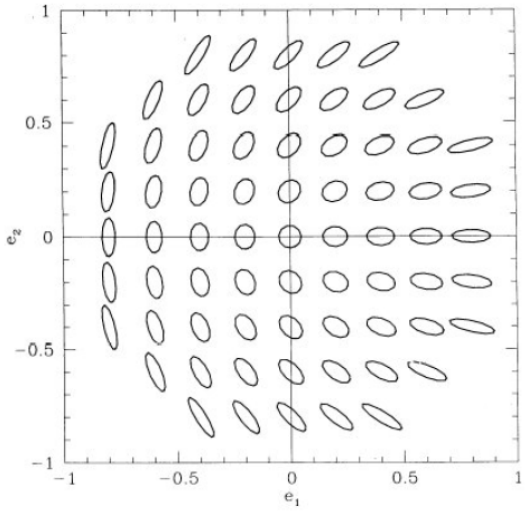

Figure 2.3: Illustration of the effect of individual ellipticity components. Reproduced from Ref. [29].

is derived by computing the second-order moments Q_{ij} of the surface brightness $I(\theta)$, with respect to the object centroid, as

$$Q_{ij} = \int d^2\boldsymbol{\theta} I(\boldsymbol{\theta})(\theta_i - \theta_i^0)(\theta_j - \theta_j^0). \tag{2.39}$$

In the presence of matter, the source shape will be slightly distorted into the observed image shape, as predicted by Eq. (2.19). Since it is a small effect, it satisfies the weak lensing approximation:

$$\kappa << 1, \quad |\gamma| << 1, \quad g \approx \gamma + \gamma\kappa. \tag{2.40}$$

By applying the lens transformation, Eq. (2.28), to the matrix of the second-order moments of the lens, it is possible to find the second-order moments of the source. Inserting this into Eq. (2.37) gives the image ellipticity. The weak lensing regime reduces Eq. (2.37) to a simple linear expression:

$$e_i^s = e_i - g_i \Leftrightarrow e_i = e_i^s + g_i, \qquad i = 1, 2. \tag{2.41}$$

This relation shows that the observed ellipticity, e_i, is the result of linearly adding the reduced shear produced by the lensing effect ($g \sim \gamma$) to the intrinsic source ellipticity e_i^s. Although the source contribution to the observed ellipticity is unknown, it is still possible to use this as a cosmic shear estimator considering the properties of the intrinsic ellipticity distribution.

Assuming galaxy orientations to be randomly distributed in the sky [26], the distribution of the source ellipticity should have an average $\langle e_s \rangle = 0$, with a dispersion σ_s, resulting in an unbiased estimator:

$$\hat{\gamma} = \langle e_{obs} \rangle - \langle e_s \rangle \pm \frac{\sigma_s^2}{N}. \tag{2.42}$$

However, this may not be the case if the considered galaxies are correlated, due, for example, to being part of the same dark matter halo. In this situation, the intrinsic ellipticity distribution will not average to zero, and the estimator will be biased.

As cosmic shear is a much smaller contribution to the overall ellipticity of the observed galaxies than their intrinsic shapes, measurements of this effect are thus very susceptible to both noise and bias. As

seen from Eq. (2.42), this results in weak lensing studies requiring a large number of galaxies N.

2.4.3 Measuring cosmic shear: systematics

The previous subsection covered how to estimate shear field properties using galaxy shapes, so as to make use of the information gathered by cosmic shear measurements. For the reasons mentioned above, weak lensing studies require deep, wide surveys, capable of probing a broad range of redshift values and collecting data from a large number of lensing sources. Fundamental bias in the cosmic shear estimator can occur due to an intrinsic alignment of galaxies, present before the lensing effect, and varies with galaxy morphology [22]. The impact of physical processes in galaxy formation can outweigh the cosmological signal produced by the dark matter lenses. In addition, the process of data acquisition and handling also introduces systematic errors, contributing to the distortion of galaxy shapes in the obtained images.

One of the main factors responsible for altering the observed galaxy ellipticities is the PSF. Light arriving at a telescope will suffer a characteristic distortion, mainly due to the properties of the optical system. In the case of ground-based observations, light rays will be further affected by seeing. In weak lensing surveys, some of these concerns can be minimised by choosing space-based instruments to avoid atmospheric effects and reduce the PSF to a diffraction-limited performance. In terms of surface brightness, the observed object, f^{obs}, will be the result of a convolution between the PSF and the original brightness profile, f^{source}, as written below:

$$f^{obs} = [PSF] * f^{source}. \tag{2.43}$$

Therefore, the correction of the PSF distortion is performed through the deconvolution of a detailed parametric model of the point-spread function from the observed images. Although a lot of effort can be put into this process, PSF residuals may remain in the corrected ellipticities [18], introducing an additive bias in the measurements that is independent of the shear signal. Other systematic errors may arise from calibration issues, such as bias in source selection criteria that can affect the mean ellipticity of the observed sample, introducing a correlation with the cosmic shear or PSF ellipticity [18]. The resulting calibration bias appears as a multiplicative error m_i, following a parametrisation of the shear bias from the Shear TEsting Programme 2 (STEP2) [19]:

$$\hat{\gamma}_i - \gamma_i^{true} = m_i \gamma_i^{true} + c_i, \tag{2.44}$$

where $i = 1, 2$ corresponds to the two individual shear components. Here, $\hat{\gamma}_i$ is the observed ellipticity, γ_i^{true} is the true shear, and c_i represents the additive bias.

Other biases can be introduced by the instrument, particularly in the detector (such as pixelation and noise), which are caused by wavelength-related effects due to a wavelength-dependent PSF, in particular galaxy colour gradients, as well as by redshift-related shear distributions due to redshfit-dependent galaxy properties (see Fig. 2.4). Common image manipulation processes, such as image registration, stacking, and aliasing [30], as well as the shape measuring methods themselves [18], can also introduce biases in shape measurements.

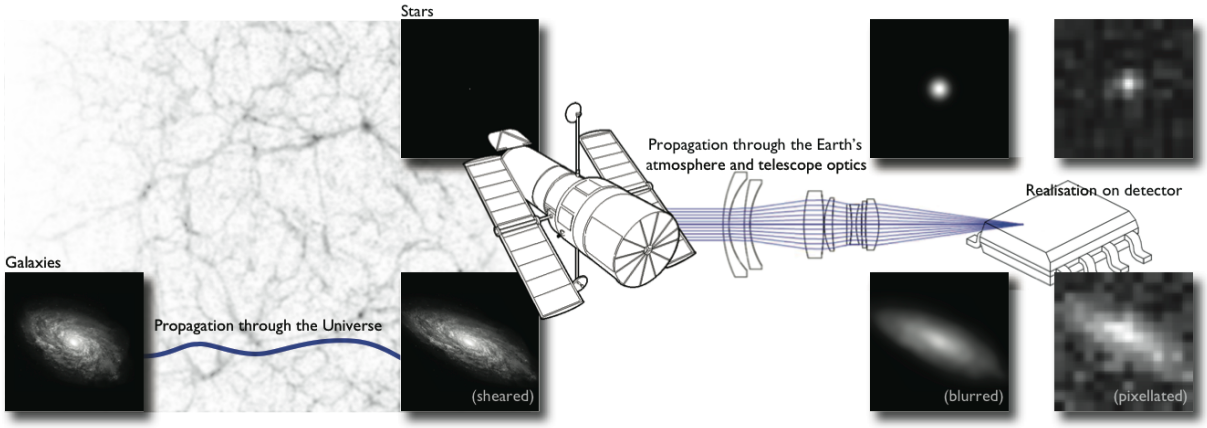

Figure 2.4: Impact of instrument bias on weak gravitational lensing observations. Adapted from Ref. [21].

2.5 *Euclid* mission

2.5.1 *Euclid* in a nutshell

The current standard cosmological model requires two components: dark matter and dark energy. The first is still unknown in nature, and the second is very difficult to explain with current fundamental physics. This causes concern, as dark energy appears to account for the majority of the energy density in the Universe, and seems to be responsible for its accelerated expansion.

The lack of observational data with the required precision to improve the current knowledge on these two components has led to the proposal and development of the *Euclid* space mission [31], by the European Space Agency (ESA). This mission will focus on two independent primary cosmological probes: weak gravitational lensing and galaxy clustering (including baryonic acoustic oscillations, and redshift space distortions). Predicted to launch in 2022, *Euclid* contains two instruments: the optical imager (VIS) and the near infra-red spectrophotometer (NISP). With these instruments, *Euclid* will perform a spectroscopic survey and an imaging survey at optical and near infrared (NIR) wavelengths, covering $15000\ \mathrm{deg}^2$ of extragalactic sky, with a wide field-of-view of $0.5\ \mathrm{deg}^2$. *Euclid* will reach limiting magnitudes of ~ 24.5, which will allow it to build a catalogue of order 1 billion weak lensing source galaxies. *Euclid* will also be complemented with photometric data from ground-based facilities, in order to estimate the photometric redshifts of this large number of galaxies.

2.5.2 Biases in *Euclid* future data

Galaxy shapes are used to estimate the shear power spectrum, but this process in itself includes systematic errors. While the ideal shear estimator is unbiased, in practice, even if galaxies are randomly oriented in an image, other processes will add their own contribution to the object shape, independently of the weak lensing effect. These external processes will introduce a bias in the estimator, which has to be corrected in order to reduce ellipticity measurements to cosmic shear alone.

All of the biases mentioned so far are general effects found when measuring ellipticity in cosmic shear studies. In addition to this, *Euclid* is being developed with particular characteristics that represent a challenge in bias determination [31], specifically related to its PSF modelling.

Euclid's point-spread function will vary along the field-of-view [32], while also varying during observation time, due to differences in spacecraft pointing jitter in between exposures [33]. It will also be slightly undersampled by the CCD pixel grid, thus needing a combination of three to four individual

exposures (dithers) in order to recover part of the spatial frequencies. Furthermore, since the VIS instrument has a single optical filter, ranging from $550-900\ nm$ [31], this will introduce a colour gradient bias due to PSF chromaticity [34]. Since the spectral energy distribution (SED) of galaxies is not constant over the entire object, but varies depending on galaxy morphology and redshift, this means that the image will be convolved with spatially different PSF models. Including such a broad range of wavelengths in a single filter results in added complexity in this correction, as the observed images must be deconvolved using an effective PSF that, in the presence of galaxy colour gradients, may not be the correct estimate of the true convolved PSF [34]. While in general the point-spread function is wavelength-dependent, this dependency can be minimised by choosing narrower filters. In the case of *Euclid*, due to its broad optical filter, the impact on the measured PSF is no longer negligible.

Overall, in order for *Euclid* to fulfil its tight scientific requirements for weak lensing measurements, it will be necessary to account for many sources of bias, and correct for them in observations, representing a challenge to future data reduction.

Chapter 3

Calibration tests

Since cosmic shear detection is technically challenging, an accurate analysis of the measurements must rely on detailed correction of instrumental effects and systematic errors. In order to study the impact of bias introduced during data acquisition and posterior image manipulation, weak lensing studies use image simulations to test and quantify additive and multiplicative bias contributions from each step of the data processing. It is the aim of this work to reproduce this methodology and study the systematics resulting from specific image operations, in light of *Euclid*'s requirements. Starting with less complex calibration tests, the present chapter gives an overview of the capabilities of the *GalSim* software, followed by a description of the configuration used to produce the set of calibration tests and the respective results for the measured bias.

3.1 *GalSim*: overview and capabilities

GalSim, the modular galaxy image simulation toolkit, is a publicly available code[3] built to satisfy the requirements for high precision simulations of images obtained in future missions such as *Euclid* [35]. Originally developed as a tool in the creation of the dataset for the GRavitational lEnsing Accuracy Testing 3 (GREAT3) challenge [36], it has since evolved to include many additional capabilities.

The software uses Python in combination with C++ so that it works essentially as a Python class library. There are two ways of producing the desired simulations: either using an input configuration file, run by the *GalSim* executable; or by using it directly within a Python script.

GalSim is able to represent astronomical objects with a wide range of complexity by offering a diverse assortment of options for building surface brightness and PSF profiles, noise parameters, weak lensing effects, and many other customisable properties, some of which will be described in more detail in the next sections. It is also able to handle convolution-deconvolution processes and other image transformations while introducing only minimal distortions to the galaxy shapes [35].

In order to build the simulated images, *GalSim* requires the definition of a set of parameters depending on the desired result. The classes and functions available for customisation can be divided into six main categories according to functionality:

1. Creation of astronomical objects through the definition of surface brightness profiles;
2. Generation of gravitational lensing effects;
3. Definition and characterisation of image-to-world coordinates;
4. Rendering of created objects into images;

[3] `https://github.com/GalSim-developers/GalSim`

5. Generation of random numbers to be used by noise models;
6. Shape estimation methods to measure observed ellipticities.

1. Surface brightness profiles

There are several ways to define the surface brightness profile of an astronomical object in *GalSim*. The main available functions include common PSF models (e.g. Airy disk), analytic galaxy profiles (e.g. Sérsic), interpolation of a user-provided input image, as well as more realistic galaxy models based on HST observations [35]. There is also the option to apply different transformations to these models, such as stretching, rotation, and dilation.

This work focused on using interpolated images of custom PSF models, convolved with realistic parametric galaxy profiles based on the Cosmological Evolution Survey (COSMOS) data [37, 38], provided by *GalSim*[4].

2. Lensing shear and magnification

Since it was originally built as part of the GREAT3 weak lensing challenge, *GalSim* is capable of handling the construction of sheared and magnified objects.

GalSim defines the shape parameter in various ways. One way is through the ratio

$$|g| = \frac{a-b}{a+b}, \tag{3.1}$$

where a and b are, respectively, the ellipse major and minor axes. This definition is used by *GalSim* under the assumption that galaxy shapes can be represented by ellipses. For ellipses, the ellipticity measured with second-order moments through Eq. (2.38) indeed reduces to the ratio in Eq. (3.1). Moreover, since the ellipticity is linearly related to the reduced shear (see Eq. (2.41)), the ratio in Eq. (3.1) is also called the reduced shear. Its components are $g_1 = |g|\cos(2\beta)$ and $g_2 = |g|\sin(2\beta)$, with β the representing the real-space position angle.

In all shear definitions used by *GalSim*, the applied transformation preserves the area, resulting in the need for an additional magnification parameter, as written in Eq. (2.29). *GalSim* also allows the definition of a lensing shear field through a specified shear power spectrum, to be applied either on a grid or to arbitrary positions.

All sheared image simulations presented in this work included a shear parameter defined by its individual components g_1 and g_2.

3. World coordinate system

In order to provide a mapping from pixel to world coordinates, *GalSim* uses two main systems, celestial and Euclidean coordinates. The first is defined in terms of right ascension (RA) and declination (Dec), based on a spherical coordinate system, while the latter is defined relative to a tangent plane projection of the sky. Since this work is based on the analysis of shear measurements in individual galaxies, as opposed to simulating an entire field-of-view, it was not necessary to define a world coordinate system.

[4] *GalSim* COSMOS dataset: `https://zenodo.org/record/3242143`

4. Image rendering

GalSim can render, or draw, object profiles onto images through three different methods: by drawing the surface brightness profile directly at the centre of each pixel; via discrete Fourier transform (DFT) of the brightness profile, by convolving the profile with a pixel response, while also allowing the convolution between both galaxy and PSF profiles if needed; or by drawing via 'photon shooting', which treats the profile as a probability distribution where the flux of each photon is added to whichever pixel it hits. If no method is specified by the user, *GalSim* defaults to DFT. The image class is also responsible for defining the number and position of galaxies to be rendered onto an image, as well as other relevant parameters such as pixel scale, background sky level, image size, and chosen coordinate system.

This work required convolving a PSF profile with different galaxy surface brightness profiles, followed by the convolution with the pixel scale. Therefore the rendering method was set to DFT.

5. Noise modelling

As noise is present in all real observational data, *GalSim* provides different noise options to choose from, depending on the instrument and scenario being modelled. The basis of all available noise models is the implementation of random deviates sampled from a range of different probability distributions. While the majority of these noise models are uncorrelated, with independent values from pixel to pixel, *GalSim* also offers the option to generate correlated noise similar to that present in real images.

Two main noise models were used throughout this work – COSMOS noise, and CCD noise –, at two different stages. These will be described in more detail further into this chapter, as well as in Chapter 4.

6. Shape measurement

GalSim includes the HSM module (Hirata, Seljak, Mandelbaum [39, 40]) containing routines to estimate second-order moments of galaxy shapes and to carry out PSF correction using different algorithms. These routines are implemented using two main functions: *FindAdaptiveMoments*, responsible for computing the moments of the best-fitting elliptical Gaussian, and returning the object shape following Eqs. (2.38) and (2.39); and *EstimateShear*, which estimates object shear, correcting for the convolution by the PSF. This correction is done through one of four methods described in the *GalSim* documentation [35].

This work focused on using the Kaiser, Squires, and Broadhurst (KSB) method [29] for the PSF correction. A more detailed description of this algorithm will be given in Section 3.2.3.

Example of GalSim capabilities

This project began by getting familiar with *GalSim*, while exploring as many functionalities as needed, with the first step in the production of simulated images being the definition of a galaxy surface brightness profile. As previously mentioned, *GalSim* provides a catalogue with real HST data from COSMOS, allowing the creation of objects with realistic properties. It is then possible to either generate parametric galaxies based on this catalogue, or to use these data to build surface brightness profiles directly from observations. The option of using parametric data from the COSMOS catalogue was chosen for all image simulations throughout this work.

Next, it was necessary to choose a PSF model to convolve with this profile. As a first test of *GalSim*'s capabilities, the chosen PSF was modelled after an optical system based on the HST mirror diameter, and the effective wavelength for its F814W optical filter (as this was the one used for obtaining COSMOS data [38]).

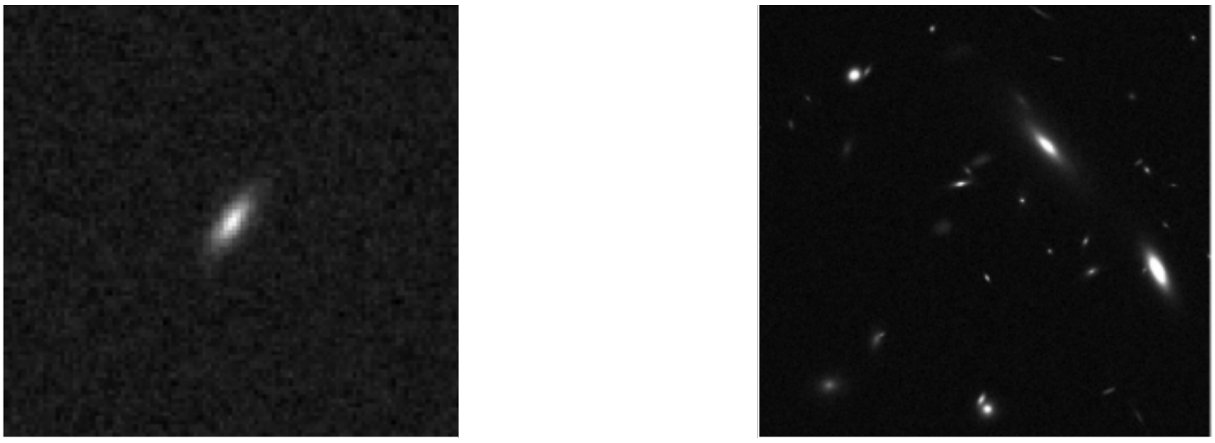

Figure 3.1: Example of simulated galaxy images using *GalSim*. *Left panel*: A single galaxy. *Right panel*: A galaxy field with 40 different randomly positioned sources. Both images contain correlated noise.

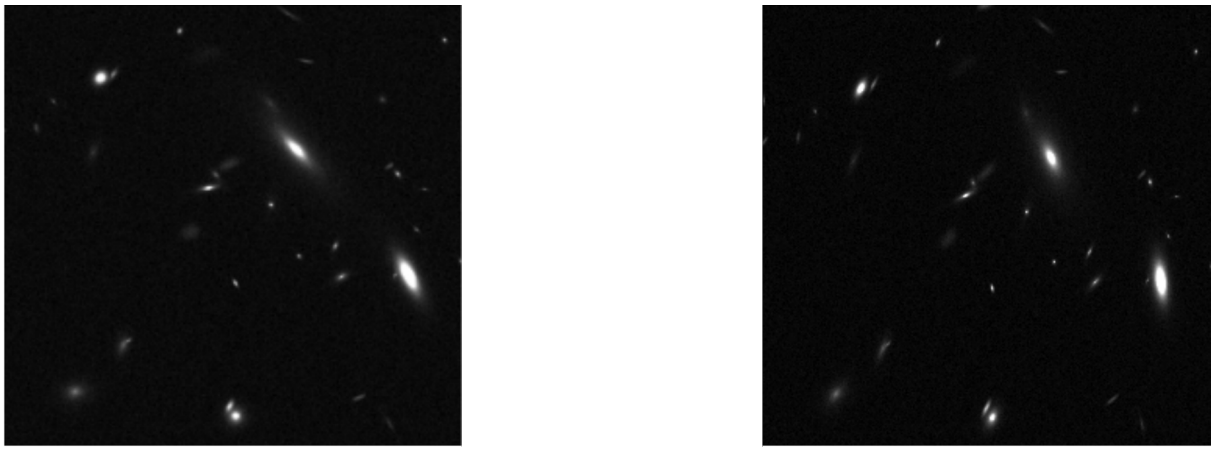

Figure 3.2: A comparison of two simulated images illustrating the differences between an image with no added shear (left panel), and an image with an input shear signal (right panel).

Two other parameters that needed to be defined were the pixel scale and the noise model. In this first approach, the pixel scale was set to 0.049 arcsec/pixel, to match the scale on the Advanced Camera for Surveys (ACS) (the instrument used when acquiring COSMOS data). For the noise model, the choice was a spatially correlated noise similar to what is found in F814W HST COSMOS science images, available in *GalSim*.

Two different images, one simulating a single galaxy, and another representing a field of galaxies, were created with this first setup and are shown in Fig. 3.1. At this stage, no shear was added, hence the observed ellipticities result from the intrinsic shape only.

In order to illustrate the impact of applying a weak lensing signal, Fig. 3.2 compares two images of the same galaxy distribution, where the one on the left contains intrinsic ellipticity only, and the one on the right contains intrinsic ellipticity plus an input shear signal. This method applies a constant shear over the entire image, resulting in every object being sheared by the same amount. The values for the shear components g_1 and g_2 were chosen so as to highly accentuate this effect, as opposed to a real cosmic shear signal. The values for the parameters used to build these two sets of images are summarised in Table 3.1.

Table 3.1: Summary of the main parameters in the *GalSim* configuration file.

Galaxy	
Surface brightness profile	COSMOSGalaxy
Galaxy type	Parametric
PSF	
Type	OpticalPSF
Wavelength	800.0 nm
Diameter	2.4 m
Image	
Pixel scale	0.049 arcsec/pixel
Image size	600×600 pixel
Noise type	COSMOS
Shear	
g_1,g_2	- 0.2, 0.2

3.2 Methodology

The core results of this thesis are divided into three main parts, with the present chapter focusing on a set of calibration tests, corresponding to less complex simulations. The following sections contain a more detailed description of the *GalSim* configuration used to produce these first tests, as well as results from shape bias measurements in the simulated images.

3.2.1 Input galaxy sample properties

As described in the previous section, *GalSim* produces galaxy images based on surface brightness profiles. The simulated sample used throughout this work was meant to represent a realistic galaxy set in its properties, such as redshift, magnitude, and size distribution. Therefore, the input galaxy population was built based on parametric models fitted to HST COSMOS observational data provided by *GalSim*. The choice of parametric galaxies, as opposed to using the exact imaging data, is justified with the need to minimise uncontrolled variability in the measurements, resulting, amongst other factors, from the complex morphologies present in real observations. Another requirement for the input galaxy population was that it covered the expected range of galaxy properties observed in *Euclid* data. Since the available HST COSMOS survey is deeper than the projected *Euclid* survey, this required the catalogue to be filtered in magnitude (in the COSMOS catalogue measured using the HST F814W filter), as well as in redshift. The new limiting values for these parameters are then $z < 2.5$, and $m_{814} < 24.5$ [41].

The largest COSMOS catalogue provided by *GalSim* comprises information for approximately 87000 galaxies. After the necessary cuts, almost 50000 galaxies were available to be used. Figure 3.3 shows the distribution in redshift, magnitude, and size of the galaxies in the new catalogue. Here, size is defined as the half-light radius, r_h, within which half of the source luminosity is contained, measured in number of pixels of the original COSMOS images. As expected [36, 42], the majority of the sources are found around $z = 0.8 - 1$, with smaller and fainter objects dominating the sample.

As described in the previous chapter, weak lensing studies use galaxy shapes to quantify cosmic shear effects, assuming a galaxy population with zero mean intrinsic ellipticity, such that the most relevant effect left results from lensing alone (Eq. (2.42)). Figure 3.4 shows the distribution of intrinsic ellipticity of the sources in the filtered catalogue, obtained by measuring the second-order moments of galaxy surface brightness, using the HSM module provided by *GalSim*. As expected, the intrinsic ellipticity,

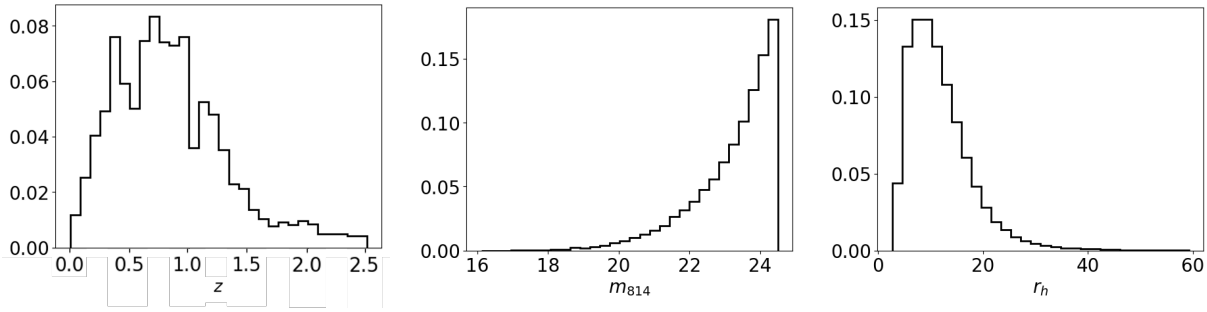

Figure 3.3: Histograms of the normalised frequency of redshift (left panel), magnitude in HST F814W filter (middle panel), and half-light radius (right panel) of the sources in the new filtered HST COSMOS catalogue.

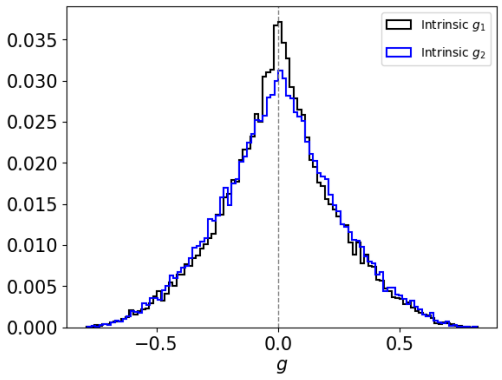

Figure 3.4: A histogram of the normalised frequency of intrinsic ellipticity of the sources in the new filtered HST COSMOS catalogue, measured with the HSM module. Solid lines in blue and black represent the shear components g_1 and g_2, respectively.

here divided into its two individual components (g_1 and g_2), is approximately zero on average. In this catalogue, source ellipticities show a dispersion of 0.3, with a noticeable, non-negligible amount of highly elliptical sources in this distribution.

3.2.2 *GalSim* Configuration

The calibration tests were divided into four different image sets, with varying parameters. The surface brightness profiles used to build the parametric galaxies were based in the filtered COSMOS catalogue, as described above, such that all four sets were based on the same input sample. These galaxies were then convolved with a *Euclid*-like point-spread function, interpolated from the FITS image shown in Fig. 3.5, kindly provided by Diana Scognamiglio from the Argelander Institute for Astronomy, Bonn. This PSF was created using a true SED, positioned in one of the standard ESA points across *Euclid*'s FoV, with a resolution of 0.02 arcsec/pixel. The image pixel scale was also the same in all tests, defined as 0.1 arcsec, corresponding to the pixel size of *Euclid*'s VIS instrument [31].

The first test set (T1) consisted of the convolution of each parametric galaxy with the *Euclid*-like PSF. No input shear, noise, or any other transformation was applied. The aim of this test was to evaluate the impact of the PSF alone on the simulated images.

Aside from the PSF convolution with each surface brightness profile, test set T2 introduced a variable lensing signal to the images. For this, a total of twelve different shear values were defined, resulting in twelve separate realizations of the almost 50000 galaxies in the catalogue. The input shear was set as (g_1, g_2) pairs, ranging from -0.06 to 0.06, based on the STEP1 and STEP2 challenges [18, 19]. They

Figure 3.5: A monochromatic *Euclid*-like PSF, with ellipticity values $g_1 = -0.04$ and $g_2 \approx 0$, as measured by *GalSim*. Image provided by Diana Scognamiglio.

were also chosen so as to include cases where shear values are identical in both components, as well as perfectly symmetric. The choice of not using a fixed step between values was made to guarantee that no bias was introduced due to possible alignment between g_1 and g_2, as well as to introduce diversity in shear conditions. The exact input shear values are shown in appendix A.1.

In the case of test set T3, the only factors contributing to galaxy shape distortion, apart from individual intrinsic ellipticity, were the PSF convolution and noise. Whenever a test included noise, the chosen noise model was COSMOS noise. *GalSim* provides an option for adding spatially correlated noise to images, modelled from the one present in the HST COSMOS F814W data. The mean noise correlation function is estimated from the catalogue observations, by averaging estimates from blank sky fields [35]. For test sets including noise, the varying parameter was the exposure time, with $t = \{10, 30, 60, 120, 180\}$ s corresponding to five different realizations of the same galaxy sample.

Finally, test set T4 included the contribution of all three main parameters: PSF convolution; noise, with exposure time variation; and variable input shear, as given in Table A.1.

A summary of the main parameter setup for each test set is presented in Table 3.2 below.

Table 3.2: Summary of parameter setup used in the different test sets.

Test set	PSF	Input shear	Noise
T1	Yes	No	No
T2	Yes	Yes	No
T3	Yes	No	Yes
T4	Yes	Yes	Yes

3.2.3 Shape measurement: KSB method

After generating the four different image sets described above, the next step consisted of measuring galaxy shapes. This was done using the *EstimateShear* function included in the HSM module. As previously mentioned, this function performs a PSF correction based on a specific implementation of the KSB algorithm [29, 35], such that the resulting shape corresponds to the galaxy ellipticity, affected by noise (when present), subtracted by the PSF.

In this method, shape parameters are first obtained by measuring the weighted second-order moments of the galaxy surface brightness, similar to Eqs. (2.38) and (2.39), now with an additional circular Gaussian weight function. This is generally necessary when analysing real imaging data, so as to suppress contributions from both nearby sources and sky noise. Similar to the previous chapter, galaxy ellipticity

due to the shearing effect e_i^{sh} is related to the source ellipticity e_i^s through [29, 43]:

$$e_i^s = e_i^{sh} - P_{ij}^{sh} g_j, \tag{3.2}$$

where g_j represents the reduced shear components and P_{ij}^{sh} is the linearised shear polarizability tensor. The tensor P_{ij}^{sh} measures the response of the shape of an object to an applied shear, and increases with the galaxy ellipticity. This equation is analogous to Eq. (2.41), but for the realistic case of weighted brightness moments.

The sheared shapes must then be corrected for the point-spread function smearing. This is done by dividing the PSF distortion into two separate effects: one resulting from the convolution with the anisotropic part of the PSF, which is responsible for a systematic shearing of galaxy images; and one from PSF isotropy, corresponding to the circularization of source shapes [43]. The KSB method will treat these two components by assuming the PSF to be the convolution of a circular isotropic part with an anisotropic perturbation. This leads to the linearisation of this anisotropy effect, with the variation in ellipticity due to this convolution written as [29]:

$$e_i^{shiso} = e_i^{obs} - P_{ij}^{sm} q_j, \tag{3.3}$$

where e_i^{shiso} represents the sheared galaxy ellipticity convolved with the isotropic component of the PSF, e_i^{obs} is the final observed ellipticity, and q_j is a measure of the PSF anisotropy. The term P_{ij}^{sm} is the smear polarizability, and is proportional to the inverse of the object's area, such that smaller objects are more affected by this anisotropy. Both tensors P_{ij}^{sh} and P_{ij}^{sm} can be computed directly from data, using the second and higher-order moments of the source brightness profile [44].

Relating the already circularised source ellipticity to the final PSF-convolved shape gives [45]:

$$e_i^{s'} = e_i^{obs} - P_{ij}^{\gamma} g_j - P_{ij}^{sm} q_j. \tag{3.4}$$

Here, P_{ij}^{γ} is the "pre-seeing" polarizability, given by:

$$P^{\gamma} = P^{sh} - \frac{P_*^{sh}}{P_*^{sm}} P^{sm}. \tag{3.5}$$

While in the absence of seeing the calculated P_{ij}^{sh} can be used as P_{ij}^{γ}, smaller sources are more affected by PSF circularization [43], resulting in the need to compute P^{γ} as in Eq. (3.5). In this expression, P_*^{sh} and P_*^{sm} represent the shear and the smear polarizability tensors measured from stellar objects, and contain information on the PSF shape only, since stars are not affected by cosmological shear [46]. It is then possible to show that the PSF correction is performed by subtracting the anisotropic part, while calibrating the ellipticity considering the PSF isotropic part as follows

$$e_i^{corr} = (e_i^{obs} - P_{ij}^{sm} q_j)(P_{ik}^{\gamma})^{-1}. \tag{3.6}$$

This quantity e_i^{corr} is thus the estimator of the cosmological shear, obtained after correcting the PSF effect. Note that e_i^{corr} still contains both the shear and the source ellipticity. It is an unbiased estimator of the shear in a sample of galaxies if the source ellipticities average to zero. It may also be a noisy estimator, not only because there is a dispersion in the values of the intrinsic source ellipticities (as seen in Eq. (2.42)), but also because it involves a division by a measured quantity P^{γ}. To compute e_i^{corr}, *GalSim* needs to compute P^{γ} and P_{ij}^{sm} for each galaxy, which are weighted moments of the surface

brightness of the galaxies.

The KSB method in *GalSim* returns two components of e_i^{corr} in the form of g_1 and g_2, representing the individual terms of the reduced shear.

3.2.4 Bias determination

Having obtained the PSF-corrected galaxy shapes for the parametric sample in each of the four test sets, they must now be compared with the known input shear values, γ_i^{input}. The determination of existing deviations from a perfect shear recovery is done by computing the best-fit parameters (m_i, c_i) to Eq. (2.44). Therefore, the parametrisation used throughout this work will be the one used in the Shear TEsting Programme 2 (STEP2) [19]:

$$\langle \gamma_i \rangle - \gamma_i^{input} = m_i \gamma_i^{input} + c_i. \tag{3.7}$$

Note that even though this parameterisation was introduced for shear, it will be applied to the reduced shear measurements of *GalSim*. This follows the standard procedure used in the literature , where in the weak lensing regime, it is assumed that γ can be approximated as the reduced shear, as seen in Eq. (2.40). However, the preliminary study of [47] shows that in the case of *Euclid* this practice will result in non-negligible biases.

Similar to what occurs in real observations, the input parametric galaxies have different intrinsic ellipticities. Since the impact of cosmic shear to the overall shape of each galaxy is so small, its estimation requires the measured PSF-corrected ellipticities to be averaged over all galaxies, $\langle \gamma_i \rangle$. As seen before, the distribution of intrinsic ellipticity has an approximately zero mean value with a standard deviation of 0.3, so when averaging the PSF-corrected shapes this contribution from intrinsic ellipticity should disappear. Using a perfect shear measurement method, both m and c would also be very close to zero, which means that the input shear would be perfectly recovered. By using the KSB algorithm, and considering the several factors that have been mentioned so far, a deviation from the input shear is expected to be introduced. From this point onward, the difference between average PSF-corrected ellipticity and input shear signal will be referred to as residual shear.

In the calibration tests presented in this chapter, the galaxy sample was divided into different sets based on the distribution of different properties, namely redshift, magnitude and size. This permitted an analysis of the bias based on sample characteristics, and the detection of correlations, if present, between bias and sample properties. The limiting values for the redshift bins were chosen in a manner appropriate for the *Euclid* lensing survey [48], here defined as $z = \{0.001,\ 0.418,\ 0.560,\ 0.678,\ 0.789,\ 0.900,\ 1.019,\ 1.155,\ 1.324,\ 1.576,\ 2.500\}$. For magnitude and size, the bin range was chosen so as to include approximately the same number of sources in each group. The resulting edge values were then defined as $m_{814} = \{16.2, 22.0,\ 22.9,\ 23.5,\ 23.8,\ 24.1,\ 24.3,\ 24.5\}$ and $r_h = \{6,\ 8,\ 10,\ 13,\ 17,\ 60\}$.

3.3 Results and Discussion

3.3.1 T1 and T2: impact of shear variation in noiseless images

Following the procedure described in previous sections, a sample of approximately 50000 parametric galaxies was convolved with the *Euclid*-like PSF shown in Fig. 3.5. Test sets T1 and T2 are noise free,

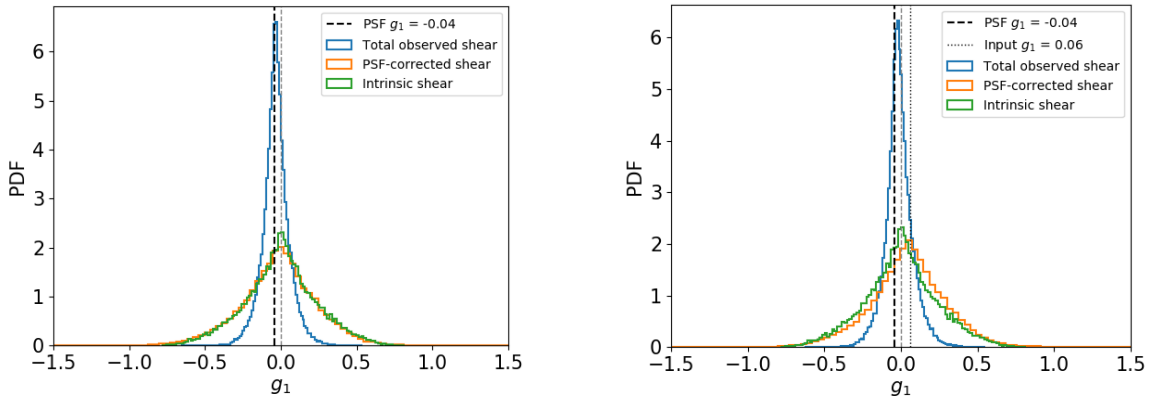

Figure 3.6: Probability density functions, for the first shear component, of total observed shear (blue), PSF-corrected shear (orange), and intrinsic ellipticity (green), for test set T1 (left panel), and for one input shear value of test set T2 (right panel). The first component of the PSF shear and the input shear value are represented by the black dashed line and the grey dotted line, respectively.

and cover a total of thirteen different input shear signals, ranging between -0.06 and 0.06, including $g_i = 0$ (T1), as defined in Table A.1.

Application of the KSB method to the thirteen realizations of the input sample resulted in measured PSF-corrected ellipticities, in a total of approximately 50000×13 values. Figure 3.6 illustrates the difference among the total observed shear (i.e. the cosmic shear signal affected by the PSF), the PSF-corrected ellipticity, and the measured intrinsic ellipticity (as presented in Fig. 3.4), for the first shear component only.

In both panels of Fig. 3.6 the total observed shear, in blue, clearly shows the effect of circularization of galaxy shapes due to the isotropic PSF component, reflected in the narrowing of the range of observed ellipticities. For test set T1, shown in the left panel, the observed distribution peaks around $g_1 = -0.04$, corresponding to the first ellipticity component of the applied PSF. Since, in this case, $g_1^{input} = 0$, the observed shear values reflect only the effect of PSF distortion, with no impact from the mock cosmic shear. On the other hand, shown in the right panel, the peak position of the total observed shear is affected by the combined distortions of PSF and input shear signal, with its distribution shifting away from the PSF ellipticity value. Results from KSB correction of PSF effects, represented by the solid orange line, return a distribution similar to the one of intrinsic ellipticity, represented in green, with both distributions showing a broader and more diverse range of ellipticities. While intrinsic shapes average to zero, in the presence of cosmic shear, the mean value of the PSF-corrected shear deviates from zero, reflecting the overall effect of the cosmic shear in ellipticity measurements. The described behaviour of these curves is also observed in the other realizations of input shear, as well as for the second shear component, g_2.

The values obtained from the implementation of the KSB algorithm were then used to find the best-fit parameters to Eq. (3.7). The residual shear, corresponding to the left-hand side of this equation, computed for T1 and T2 combined, is shown in Fig. 3.7, as a function of the input shear. Errors bars shown in this, and in the following figures, were obtained by computing the standard deviation of the mean for the various samples.

As previously mentioned, the bias quantification in calibration test sets T1 to T4 was done by dividing the galaxy sample based on its properties, in particular redshift, magnitude and size, and by analysing the residual shear separately for each bin. In the first sample binning, illustrated in Fig. 3.7, galaxies

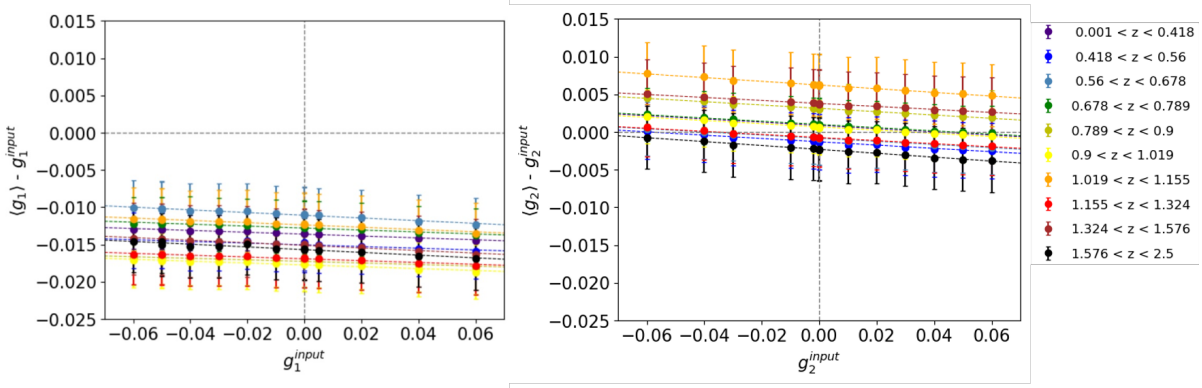

Figure 3.7: Combined results from the residual shear present in test sets T1 ($g = 0$) and T2, divided in its individual components g_1 (left panel) and g_2 (right panel), as a function of input shear signal. The dashed lines represent the linear fit from which m and c parameters are extracted. The different colours correspond to the ten redshift bins, with the edge values made explicit in the label. Each bin contains approximately 5000 galaxies.

were divided in ten redshift classes, here represented by ten different colours, with limits as given in the previous section, with each bin containing approximately 5000 galaxies.

Since the average intrinsic ellipticity peaks around zero, in the absence of deviations from a perfect shear recovery, the residual shear would also be zero, as the additional distortion in the corrected shapes would be attributed solely to the input lensing signal. As expected in more realistic conditions, Fig. 3.7 shows a non-zero slope with a residual shear offset, for all redshift bins, as well as for both components of shear. The resulting negative slope, which is consistent across redshift bins, shows that this measuring method systematically underestimates shear, independently of redshift and component. A similar behaviour has been observed when implementing KSB-based methods in different weak lensing studies with varied simulation conditions [18, 19, 41, 49, 50]. The offset values for the binned residual shear do not show any particular ordering, with higher residuals being attributed to either high-z or low-z galaxies. It is also relevant to note that, even when the input shear is set to zero (T1), some residual shear still remains in the measurements (between -0.020 and -0.010 for g_1, and between -0.002 and 0.006 for g_2). This is most likely an indicator of systematic errors introduced by the PSF-correcting method itself. The second shear component shows a smaller offset, mostly positive, and a steeper slope, whereas the first component has only negative values for residual shear.

These trends are best observed when analysing both slope and offset, simultaneously. Fitting the calibration and additive bias parameters in Eq. (3.7) returns the values for m and c shown in Table B.1,

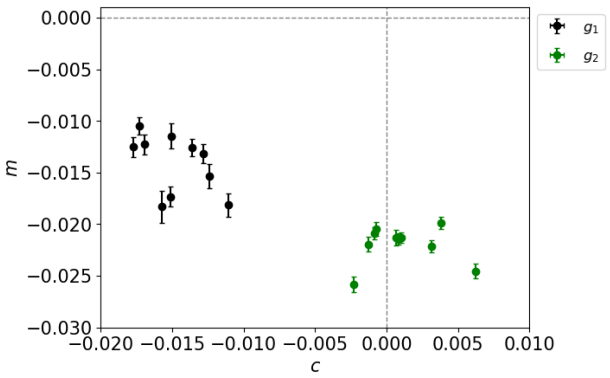

Figure 3.8: Fitted values of multiplicative and additive biases for each redshift bin. Black and green points correspond, respectively, to the first and second components of shear.

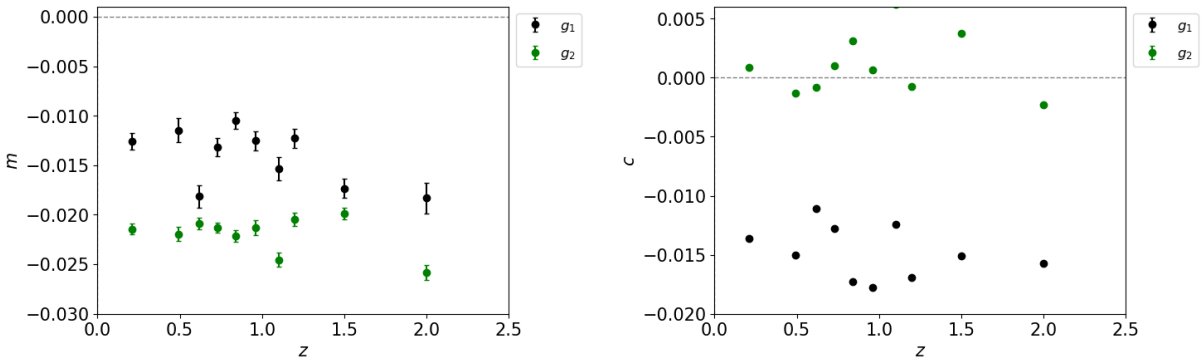

Figure 3.9: Variation of multiplicative bias (left panel), and additive bias (right panel) as a function of redshift. Black and green points represent, as before, the first and second components of shear.

and plotted in Fig. 3.8 below. The very small fitting errors (of the order of 10^{-4} for the multiplicative bias, and 10^{-5} for the additive term) translate what has been observed in Fig. 3.7, reflecting a well-behaved linear regression with a dispersion of 10^{-4} between redshift bins, corresponding to a consistent linear response to the input shear signal. The disparity in behaviour regarding the two different shear components becomes clear when analysing Fig. 3.8. This separation is given by the difference in overall values for the residual shear offset and multiplicative bias. The g_2 shear component, here shown in green, has a slightly higher absolute multiplicative bias, with the mean value $\langle m_2 \rangle = (-2.20 \pm 0.06) \times 10^{-2}$, while $\langle m_1 \rangle = (-1.42 \pm 0.09) \times 10^{-2}$. As mentioned before, component g_2 also appears to be less affected by the PSF correction than g_1, with $\langle c_2 \rangle = (1.05 \pm 0.83) \times 10^{-3}$, and $\langle c_1 \rangle = (-14.77 \pm 0.71) \times 10^{-3}$, respectively. This difference seems to derive from the additive bias dependence on PSF systematics originated from an imperfect PSF anisotropy correction. The convolved monochromatic PSF has a g_1 ellipticity component that is much higher than the second one, particularly $g_1^{PSF} = -0.04$ compared with $g_2^{PSF} \approx 0$, as measured by *GalSim*, and this is most likely the factor responsible for introducing larger residuals on the first component. This behaviour is in agreement with what may be expected for KSB-based algorithms, and has been observed in literature [19, 51]. In particular, in the bias analysis of the STEP2 project [19], similar values have been reported when highly elliptical PSFs (of the order of $g_1 \simeq 0.11$ and $g_2 \simeq 0.02$) were applied .

The explicit variation of both multiplicative and additive biases with redshift is shown in Fig. 3.9. As seen in Fig. 3.8, there is a clear difference in the way that individual components of shear, g_1 and g_2, are affected. Both components show a slight increase in bias for higher redshift galaxies, but otherwise appear to have a weak correlation with this property. This variation could be an indication that, although m and c are weakly correlated with the sample's redshift distribution, they may depend more strongly on other properties that are critical at higher z.

In order to evaluate how these biases vary with other galaxy parameters, a similar analysis was done dividing the sample in bins of magnitude and size. Results from the variation of multiplicative and additive biases as a function of magnitude are presented in Fig. 3.10, and summarised in Table B.2. The limits for the chosen binning are defined at the end of the previous section.

Variation of both calibration and additive biases with source magnitude has been studied and reported in the STEP1 and STEP2 analyses [18, 19]. These analyses computed m and c values using different PSF models, as well as several PSF-correcting algorithms, some of which were KSB-based. From Fig. 3.10, it is possible to observe, as in Fig. 3.8, a clear separation between g_1 and g_2 regarding the additive bias, with the g_2 shear component being less affected by this residual distortion, specifically $\langle c_1 \rangle =$

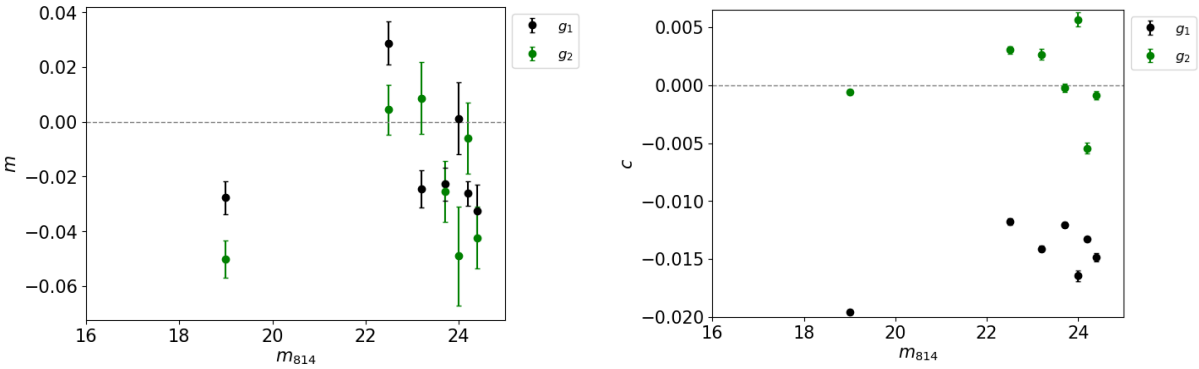

Figure 3.10: Variation of multiplicative bias (left panel), and additive bias (right panel) as a function of magnitude, measured by the HST F814W filter. Larger error bars indicate higher dispersion within magnitude bins.

$(-14.60 \pm 1.03) \times 10^{-3}$, and $\langle c_2 \rangle = (0.60 \pm 1.35) \times 10^{-3}$. High shear offsets were also observed in STEP2, being attributed to the use of highly elliptical PSFs. Figure 3.10 shows, once again, that there is little separation of the two components relative to the multiplicative bias, with m values for g_1 and g_2 behaving in a similar way as a function of magnitude, with $\langle m_1 \rangle = (-1.48 \pm 0.83) \times 10^{-2}$ and $\langle m_2 \rangle = (-2.28 \pm 0.96) \times 10^{-2}$. It also shows that the faintest galaxies tend to be more affected by systematic errors, particularly regarding the multiplicative bias. Binning the sample in this manner increases fitting errors to the order of 10^{-3} for m, and 10^{-4} for c, showing higher variability within each magnitude range. Dispersion of m and c between bins also increases from $\sim 10^{-4}$ to 10^{-3}, relative to the redshift analysis. The variation of both multiplicative and additive biases with source magnitude, shown for the present test sets, is in concordance with what has been reported during both STEP1 and STEP2 analyses [18, 19]. Since bin edges were chosen so as to include approximately the same number of sources in each bin (~ 7000), the magnitude scale is not evenly populated; if it were, then it could have helped to better observe this behaviour. This is also the case for the results obtained when binning the sample based on size, which includes ~ 8000 sources per bin.

Variation of multiplicative and additive biases as a function of half-light radius, in units of pixels, is presented in Fig. 3.11, with values summarised in Table B.3. It shows a general increase in bias for smaller sized galaxies as opposed to extended sources, which was also reported in the STEP2 analysis [19], for KSB-based algorithms. This result is consistent with the previous figure, where bias increased for fainter sources, which is to be expected due to the usual correlation between these two quantities. Figure 3.12 below allows for a better understanding on how this correlation is distributed across the sample. Binning galaxies based on their half-light radius results in average values for multiplicative and additive biases of $\langle m_1 \rangle = (-1.40 \pm 0.46) \times 10^{-2}$, $\langle m_2 \rangle = (-2.32 \pm 0.86) \times 10^{-2}$, $\langle c_1 \rangle = (-14.67 \pm 0.83) \times 10^{-3}$, and $\langle c_2 \rangle = (1.07 \pm 0.61) \times 10^{-3}$. Fitting errors are kept around the same values as observed when binning in magnitude, with dispersion across bins decreasing for c ($\sim 10^{-4}$), while remaining $\sim 10^{-3}$ for m.

Generally, dividing the sample in redshift, magnitude, and size bins allowed to understand existent correlations between correction bias and sample properties. Despite these possible correlations, average values for multiplicative and additive biases were consistent between the different binning choices, showing that, for these first calibration tests, $m \approx 10^{-2}$, and $c \approx 10^{-2} - 10^{-3}$ (here showing a strong dependence with PSF ellipticity), which is in agreement with most weak lensing challenges that quantify correction bias in simulated galaxies [18–21, 36], involving KSB implementations.

However, it is relevant to notice a discrepancy in these trends, where the bin containing the brightest

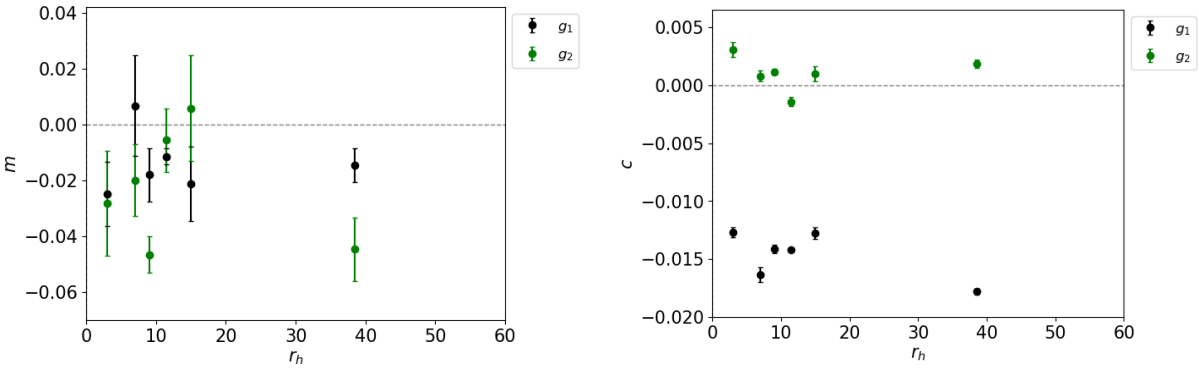

Figure 3.11: Variation of multiplicative bias (left panel), and additive bias (right panel) as a function of half-light radius, given in number of pixels. Larger error bars indicate higher dispersion within size bins.

sources, in Fig. 3.10, and the one with the largest galaxies, in Fig. 3.11, show an unexpected increase in correction bias. This could either be reflecting a correlation with intrinsic ellipticity dispersion within the bin, or with signal-to-noise ratio. As was mentioned, magnitude and size binning limits were chosen so as to include the same number of sources in each bin. For the catalogue used when building the calibration test images, this implies that larger and brighter objects are less numerous, as shown in Section 3.2.1. This results in these two bins including a wider range of galaxy properties, as opposed to a more homogeneous distribution found in other bins. From the difference in c between shear components, presented in the right-hand panel of both Figs. 3.10 and 3.11, it is clear that the KSB algorithm introduces higher residuals for highly elliptical PSFs. It is also known, however, that this method looses some of its accuracy with larger source ellipticities [51]. Since these two bins contain objects with very different characteristics, as illustrated in Fig. 3.12, and since the correction for PSF distortion is done individually to each galaxy, the resulting residual shear may be a contaminated average, due to asymmetric corrections associated to the properties of each galaxy population.

Figure 3.12 shows the variation of galaxy sizes as a function of their respective magnitude, illustrating correlations between galaxy properties, present in the filtered COSMOS catalogue. The different colours represent separate redshift bins, containing approximately the same number of sources. The edge values for this division are $z = \{0.001, 0.418, 0.684, 0.899, 1.192, 2.5\}$. Similar to the information contained in Fig. 3.3, this shows that higher redshift sources in the catalogue are simultaneously, and almost

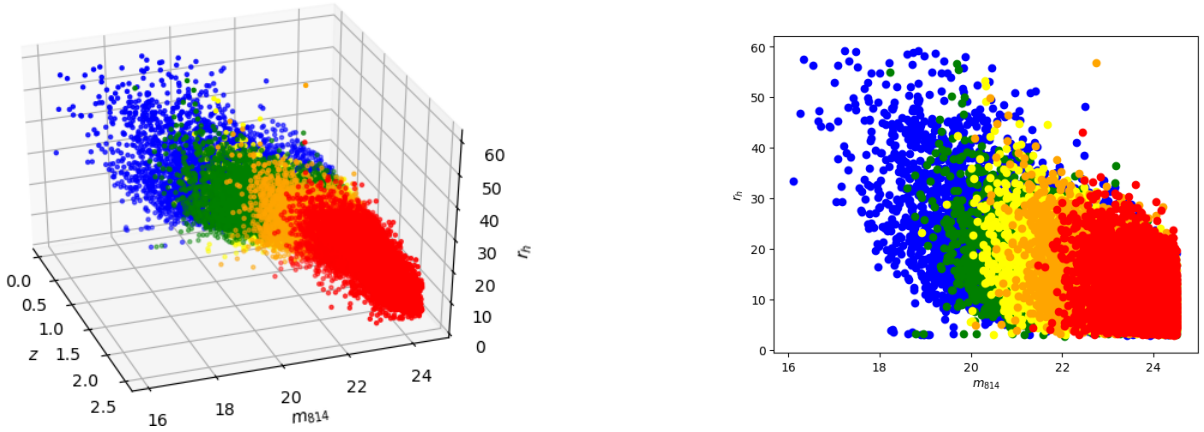

Figure 3.12: *Left panel*: relation between redshift, magnitude, and size in the filtered COSMOS sample. *Right panel*: variation of galaxy size as a function of its magnitude. The different colours correspond to separate redshift bins.

exclusively, faint and small, whereas low z objects, shown in blue, appear to take a wider range of values in both magnitude and size. Analogously, it also shows that larger and brighter sources belong exclusively to the lowest redshift bin. This can help explain m and c variation with redshift, as presented in Fig. 3.9. Here, galaxies with the highest redshift values seem to be more affected by correction bias, and these correspond to objects represented in Fig. 3.12 as red points. On the other hand, sources with lower z that show a weak correlation to this property, appear to be associated with a wider variety of sizes and magnitudes. The lack of homogeneity in this distribution reflects limitations in the detection of fainter galaxies in higher redshift regions, and was already expected since closer objects are easier to resolve, allowing probing a larger range of morphologies.

3.3.2 T3 and T4: impact of shear and noise combination

As before, the galaxy sample used in test sets T1 and T2 was convolved with the same *Euclid*-like PSF profile, this time varying both input shear signal and noise. Test sets T3 and T4 were constructed using all thirteen shear signals, as defined in Table A.1, while simultaneously varying exposure time. The previous binned analysis in redshift, magnitude, and size was also applied to these tests. Variation in exposure time is reflected in the noise model parameters. As mentioned before, the chosen noise model for these calibration tests was of the COSMOS type - a parametrisation for the correlated noise function found in HST COSMOS images.

The results of shape measurement and further quantification of the existent multiplicative and additive biases, for the case of redshift binning, are presented in Fig. 3.13. Here are represented two situations with the lowest and highest exposures times, corresponding to two opposite noise situations, with $t_{\rm exp} = 10$ s and $t_{\rm exp} = 180$ s. The overall values of m and c do not appear to be highly affected by the change in exposure time for this particular noise model, with the exception of a specific redshift range. Test sets T3 and T4 appear to behave similarly to test sets T1 and T2, with a prominent separation between shear components, most likely resulting from imperfect PSF correction.

As observed in test sets T1 and T2, results shown in Fig. 3.13 are a representation of the behaviour of residual shear, illustrated in Figs. 3.14 and 3.15. The highly deviated (m, c) point shown on the left panel of Fig. 3.13 seems to correspond to a particular redshift bin ($0.9 < z < 1.019$), especially affected by higher input shear values, and aggravated by noise. After looking in more detail at the values for the measured PSF-corrected shear, it was observed that *GalSim* was allowing ellipticity components to be higher than one, which implied a reduced shear modulus of $|g| > 1$. As seen in Chapter 2, in the weak

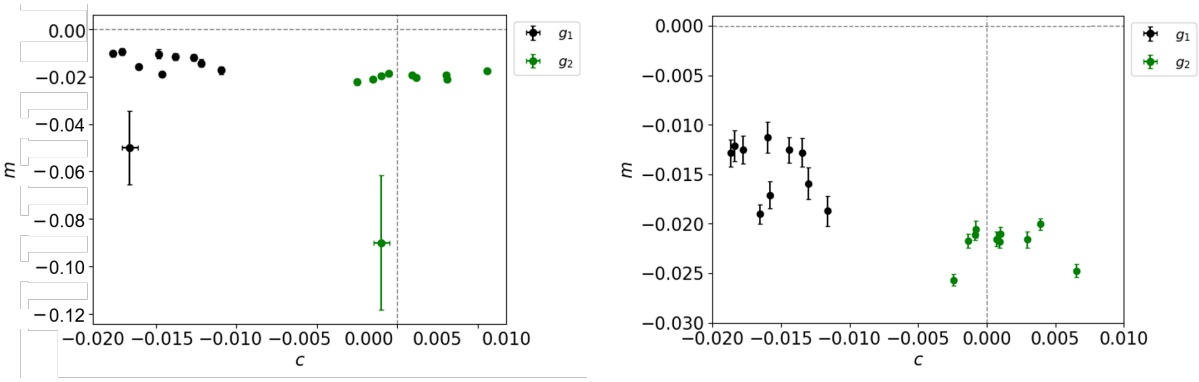

Figure 3.13: Fitted values of multiplicative and additive biases for each redshift bin, for an exposure time of 10 s (left panel), and 180 s (right panel). Black and green points correspond, respectively, to the first and second components of shear.

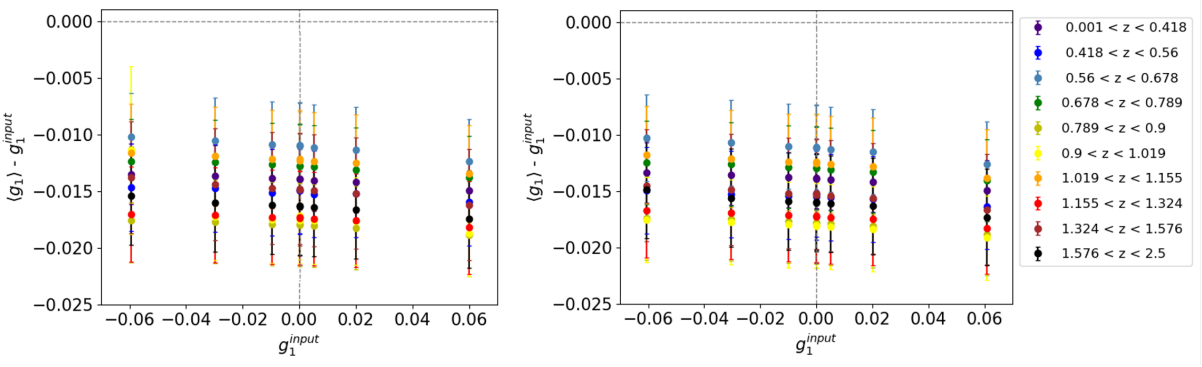

Figure 3.14: Results for the residual shear present in test sets T3 and T4, for the first component, g_1, in the case of an exposure time of 10 s (left panel), and of 180 s (right panel), as a function of input shear signal.

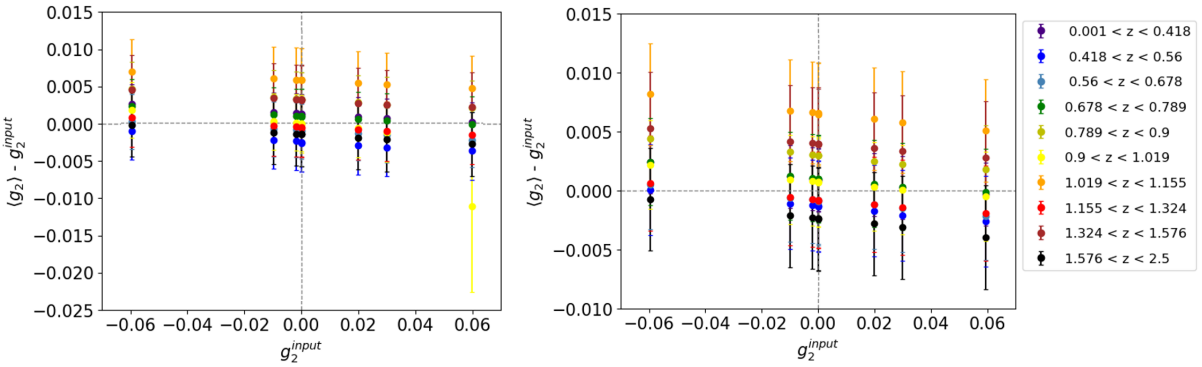

Figure 3.15: Results of the residual shear present in test sets T3 and T4, for the second component, g_2, in the case of an exposure time of 10 s (left panel), and of 180 s (right panel), as a function of input shear signal.

lensing regime, defined by Eq. (2.40), the true shear can be approximated by the reduced shear, so that the estimator for cosmic shear becomes the PSF-corrected ellipticity. This means that g_1 and g_2 should never be higher than one, as they are associated to galaxy ellipticities. For this reason, shear component values resulting in $|g| > 1$ were consequently excluded from the analysis, as they were naturally contaminating the values of multiplicative and additive biases.

From Figs. 3.14 and 3.15, and according to the values for m and c shown in Table B.4, averaged over all redshift bins for the different exposure times, a slightly more pronounced deviation is associated to shorter exposures, which should be in agreement with the expected increase in performance for longer exposures [49], as the signal-to-noise ratio (SNR) also tends to increase. Binning galaxies based on redshift results in average values for multiplicative and additive biases of $\langle m_1 \rangle = (-1.71 \pm 0.38) \times 10^{-2}$, $\langle m_2 \rangle = (-2.70 \pm 0.70) \times 10^{-2}$, $\langle c_1 \rangle = (-14.67 \pm 0.71) \times 10^{-3}$, and $\langle c_2 \rangle = (0.70 \pm 0.80) \times 10^{-3}$, for the 10 s exposure time images. For the longest exposure, these values are $\langle m_1 \rangle = (-1.42 \pm 0.09) \times 10^{-2}$, $\langle m_2 \rangle = (-2.17 \pm 0.06) \times 10^{-2}$, $\langle c_1 \rangle = (-14.80 \pm 0.72) \times 10^{-3}$, and $\langle c_2 \rangle = (1.04 \pm 0.82) \times 10^{-3}$. Since the bias values for the highest exposure time introduced were already close to the ones measured in the noise-free test sets T1 and T2, it is reasonable to assume that multiplicative and additive biases would not improve significantly by increasing exposure time even further. From the analysis of Table B.4, dispersion across redshift bins for $t_{\rm exp} = 180$ s appears to decrease significantly for multiplicative bias (from $\approx 10^{-3}$ to 10^{-4}), while remaining approximately the same for the additive bias.

As observed so far, the explicit variation of m and c values with redshift, presented in Figs. 3.16 and 3.17, shows that the impact, in bias quantification, of varying the exposure time is low. Although most of the errors appear to be introduced at shorter exposure times, the variation of bias values with exposure

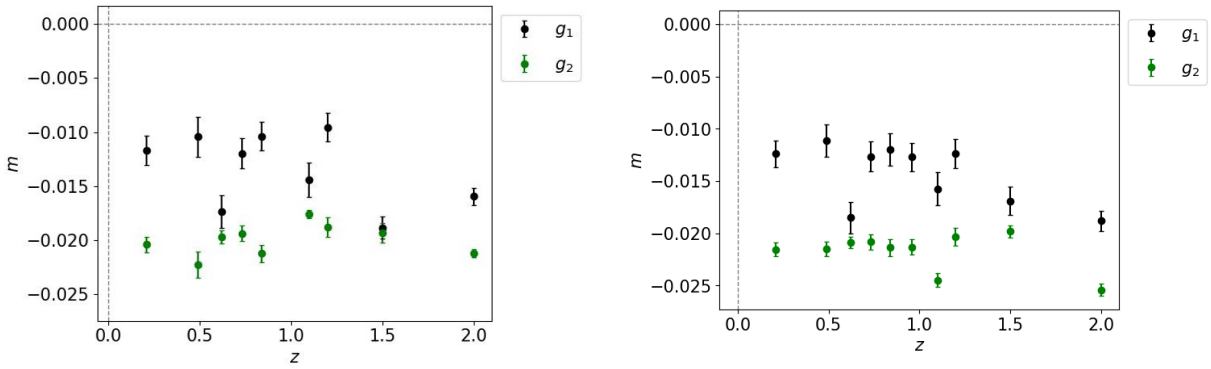

Figure 3.16: Variation of multiplicative bias for $t_{\rm exp} = 10$ s (left panel), and $t_{\rm exp} = 180$ s (right panel) as a function of redshift. Black and green points represent the first and second components of shear. The outlier value corresponding to $0.9 < z < 1.019$ was removed from the plot, so as to better compare the two situations.

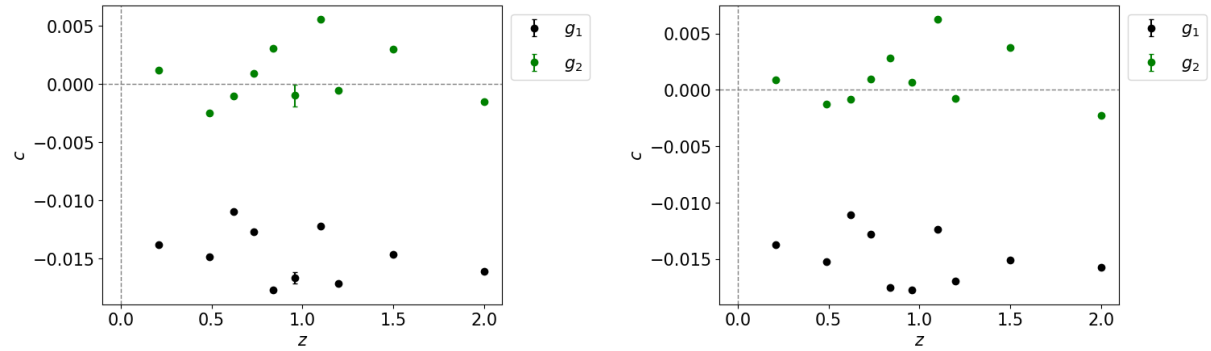

Figure 3.17: Variation of additive bias for $t_{\rm exp} = 10$ s (left panel), and $t_{\rm exp} = 180$ s (right panel) as a function of redshift. Black and green points represent the first and second components of shear.

time is not as significant as first expected, with the effect of noise being more pronounced in the values of multiplicative bias. The amount of noise appears to correlate with the dispersion of m over the redshift range, creating larger variations for the case of $t_{\rm exp} = 10$ s when compared to $t_{\rm exp} = 180$ s which shows a closer distribution to the noise-free tests.

It is relevant to take into consideration that the chosen noise model, even though based on the one existent in the HST data available on *GalSim*, is not necessarily the most similar to the one found in future *Euclid* data. Galaxy simulation results presented in the next chapter will include CCD noise modelled after CCD parameters defined so as to mimic *Euclid* noise.

Overall, the results from varying exposure time, with a COSMOS noise model, in a sample divided in redshift bins, produced similar values as test sets T1 and T2, with higher redshift galaxies being more affected by bias, but with a generally weak correlation with z.

Results from magnitude binning also indicate a similar trend as test sets T1 and T2, regarding multiplicative and additive biases, as shown in Figs 3.18 and 3.19. As before, there is only a clear separation between shear components when analysing additive bias, with m behaving similarly for both g_1 and g_2. Averaging values over all magnitude ranges results in $\langle m_1 \rangle = (-2.28 \pm 1.43) \times 10^{-2}$, $\langle m_2 \rangle = (-4.73 \pm 1.15) \times 10^{-2}$, $\langle c_1 \rangle = (-14.61 \pm 1.08) \times 10^{-3}$, and $\langle c_2 \rangle = (2.45 \pm 1.51) \times 10^{-3}$, for the $t_{\rm exp} = 10$ s simulations, and $\langle m_1 \rangle = (-1.95 \pm 0.98) \times 10^{-2}$, $\langle m_2 \rangle = (-1.39 \pm 0.82) \times 10^{-2}$, $\langle c_1 \rangle = (-14.78 \pm 1.68) \times 10^{-3}$, and $\langle c_2 \rangle = (0.57 \pm 2.08) \times 10^{-3}$, for $t_{\rm exp} = 180$ s. In this case, increasing exposure time generally decreases the error within magnitude bins, indicated by the smaller error bars. Dispersion across magnitude bins does not change significantly, remaining on the order of

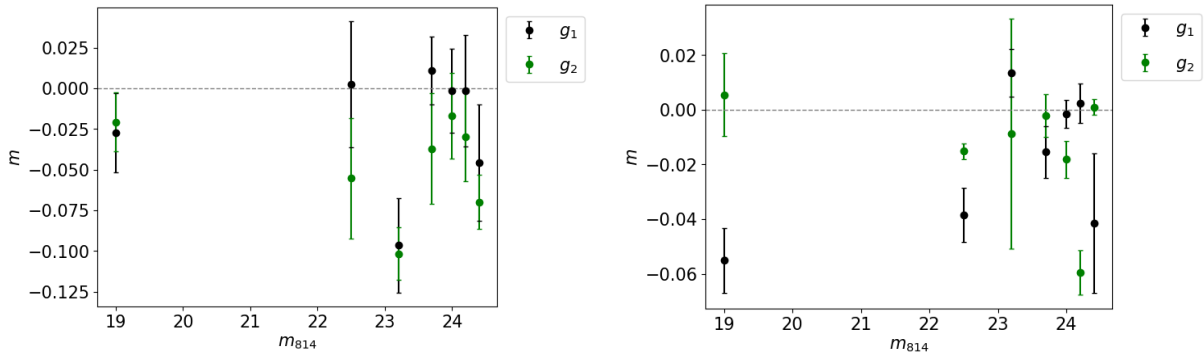

Figure 3.18: Variation of multiplicative bias for $t_{\rm exp} = 10$ s (left panel), and $t_{\rm exp} = 180$ s (right panel), as a function of magnitude, measured by the HST F814W filter. Larger error bars indicate higher dispersion within magnitude bins.

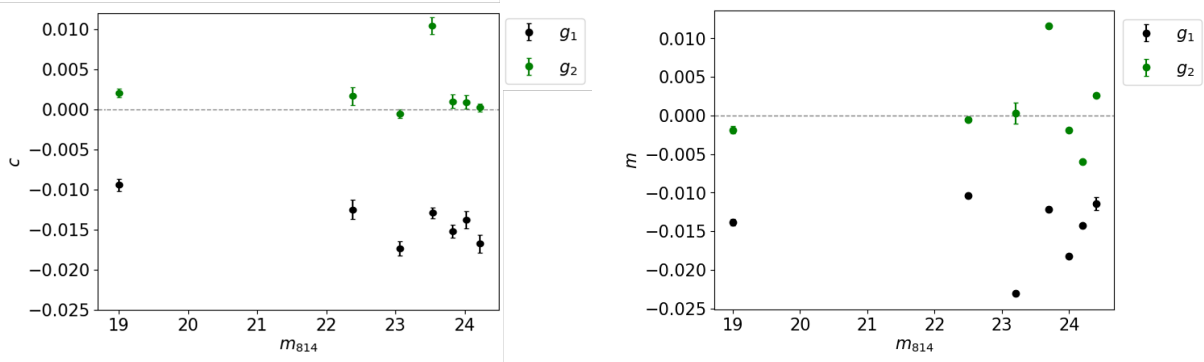

Figure 3.19: Variation of additive bias for $t_{\rm exp} = 10$ s (left panel), and $t_{\rm exp} = 180$ s (right panel), as a function of magnitude, measured by the HST F814W filter.

$\sim 10^{-3}$. While multiplicative bias increases for fainter galaxies, as already seen in the previous tests, additive bias does not appear to follow any particular trend, with high dispersion of c across the different magnitude bins. Explicit values for each m and c, averaged over the magnitude range, corresponding to each exposure time, are presented in Table B.5.

As seen with magnitude binning, results from dividing the sample based on half-light radius, while varying the exposure time, behave similarly to test sets T1 and T2, although with a wider dispersion, so that the correlation between correction bias and galaxy size becomes harder to observe. The values for multiplicative and additive biases as a function of half-light radius are shown in Figs. 3.20 and 3.21. Explicit values for each m and c, averaged over all bins, corresponding to each exposure time introduced, are presented in Table B.6. From the figures below, it is possible to observe a decrease in uncertainty within bins, when increasing the exposure time from 10 s to 180 s. Average values for the bias parameters, in the first case of shorter exposure, are $\langle m_1 \rangle = (-0.38 \pm 0.48) \times 10^{-2}$, $\langle m_2 \rangle = (0.51 \pm 1.23) \times 10^{-2}$, $\langle c_1 \rangle = (-6.92 \pm 0.73) \times 10^{-3}$, and $\langle c_2 \rangle = (-7.13 \pm 0.66) \times 10^{-3}$. In the case of $t_{\rm exp} = 180$, these values appear to approximate the analogous case in test sets T1 and T2, with $\langle m_1 \rangle = (-0.87 \pm 0.86) \times 10^{-2}$, $\langle m_2 \rangle = (-2.01 \pm 0.74) \times 10^{-2}$, $\langle c_1 \rangle = (-11.10 \pm 0.73) \times 10^{-3}$, and $\langle c_2 \rangle = (0.74 \pm 0.57) \times 10^{-3}$. Albeit a high dispersion across bins, Fig. 3.20 shows that smaller objects tend to be more affected, confirming the same behaviour seen in test sets T1 and T2, particularly in the presence of noise.

While the first calibration tests, T1 and T2, focused solely on the variation of correction bias with input shear on PSF convoluted galaxies, test sets T3 and T4 showed how, and how much, the presence

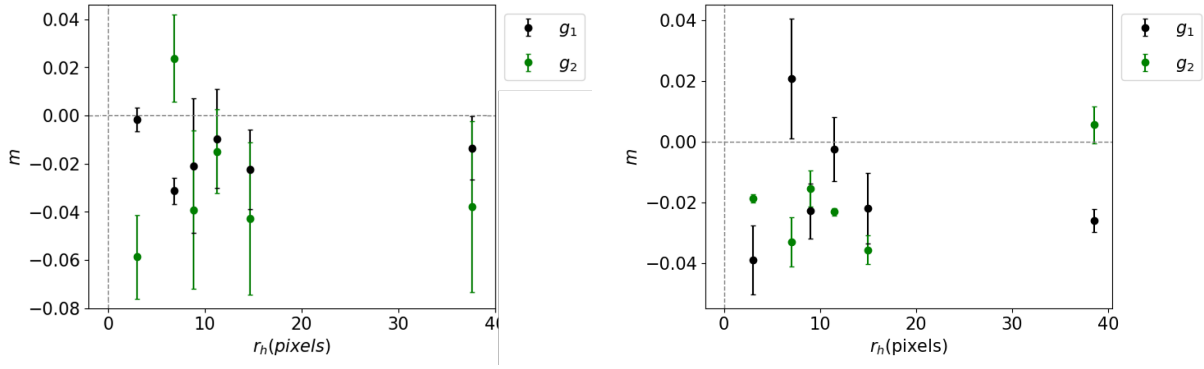

Figure 3.20: Variation of multiplicative bias for $t_{\rm exp} = 10$ s (left panel), and $t_{\rm exp} = 180$ s (right panel), as a function of half-light radius.

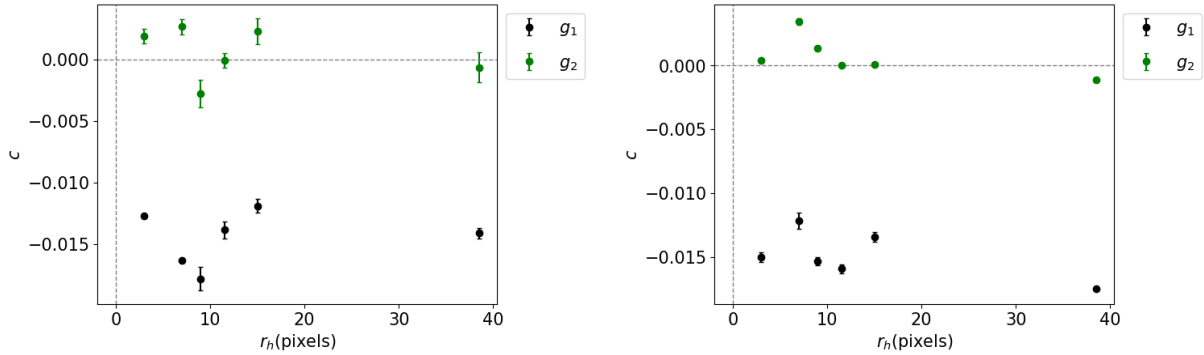

Figure 3.21: Variation of additive bias for $t_{\rm exp} = 10$ s (left panel), and $t_{\rm exp} = 180$ s (right panel), as a function of half-light radius.

of noise can introduce greater uncertainty in shear measurements, while also increasing the correction bias. The noise model that was chosen for these first calibration tests did not impact the measurements as much as expected. Overall, binning the sample based on redshift did not reflect any clear correlation. On the other hand, binning in magnitude and size showed that, generally, fainter, smaller galaxies are more affected by systematic errors, illustrating the need for a very accurate bias analysis regarding these objects, especially since sources with these characteristics make up the most part of the sample, and the bulk of weak lensing surveys.

Overall, results from these calibration tests showed a clear separation between the two shear components, specifically a negative multiplicative bias of the order of $\sim 10^{-2}$, a negative additive bias of $\sim 10^{-2}$ for g_1 (associated with the high ellipticity component of the PSF), and a positive additive bias of $\sim 10^{-3}$ for g_2. During the analysis of these calibration tests, sources of error were detected resulting from the KSB implementation in *GalSim* (for example, allowing corrected shear values $|g| > 1$), which then permitted imposing conditions to the results in Chapter 4 so as to improve the bias measurements. Due to the low impact of the noise model applied in test sets T3 and T4, images in Chapter 4 were therefore simulated using a different type of noise. In these tests, it was also verified that the average intrinsic ellipticity peaked around zero for this sample, which justified the choice of not applying the common procedure of rotating each galaxy by $90°$, and try to use the estimator in more realistic conditions. In that method (see for example [52]), matched pairs of unrotated and rotated versions of each galaxy are used instead of the actual galaxy orientations. The shear estimator is then applied to the pairs, ensuring that the intrinsic ellipticity of each pair is indeed zero, removing this source of bias and uncertainty.

Chapter 4

Simulating *Euclid* data

Being a very small effect in the overall measurement of galaxy shapes, cosmic shear signal is bound to be contaminated by systematic and spurious errors. This chapter aims to quantify the impact that different image manipulation processes have on multiplicative and additive biases, measured in *Euclid*-like simulated images, as well as to quantify biases introduced by PSF variation across *Euclid*'s field-of-view.

4.1 Methodology

4.1.1 Input galaxy sample reduction

Due to limitations regarding computation time, it became necessary to decrease the number of galaxies in the input sample used in this second part of bias analysis. The filtered COSMOS catalogue, described in Section 3.2.1 and applied to the previous calibration tests, was downsized from approximately 50000 objects to 5000, with the new sample representing 10% of the original distribution. This reduction was done by dividing the catalogue in five equally populated bins of redshift, with roughly 10000 galaxies each, and then randomly choosing 1000 objects from each of the bins, resulting in a reduced sample of 5000 galaxies. The sample was also separated in five equally populated bins of magnitude, and in five equally populated bins of size, to which was applied the same procedure, thus obtaining 3 samples of 5000 galaxies. After analysing the three different downsized catalogues, it was observed that they had approximately the same distribution of galaxy properties (redshift, magnitude, size, and intrinsic ellipticity), which resulted in only one being chosen as the final input sample. Afterwards, it was verified that the three cuts along different properties resulted in the same distributions, by analysing the correlations between them (as done in Fig. 3.12).

In order to guarantee, as much as possible, that this new sample was representative of the entire catalogue, the distribution of galaxy characteristics would have to be similar. Fig. 4.1 shows a comparison between the large COSMOS catalogue, in orange, and the new reduced sample, in blue, regarding redshift, magnitude, and half-light radius distributions. Both input samples present an approximate distribution of sources in each galaxy property, with small deviations between them. Particularly, the new catalogue appears to have slightly less sources between $z = 0.4$ and $z = 0.5$, as well as in bin $0.9 < z < 1$. This effect is then translated in a very small variation in magnitude bins, being more apparent in galaxy size distribution, where there is a 2% excess of smaller galaxies ($r_h < 5$), and a decrease in sources around $r_h \approx 15$.

Another relevant characteristic that is likely to influence the results is the sample's intrinsic ellip-

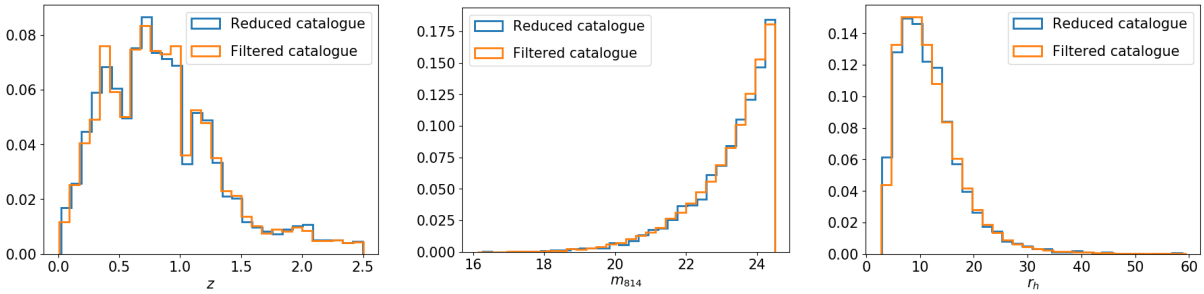

Figure 4.1: Histograms of normalised frequency of redshift (left panel), magnitude in F814W filter (middle panel), and half-light radius (right panel) in the filtered HST COSMOS catalogue (orange), used to build the calibration tests, and in the reduced sample (blue).

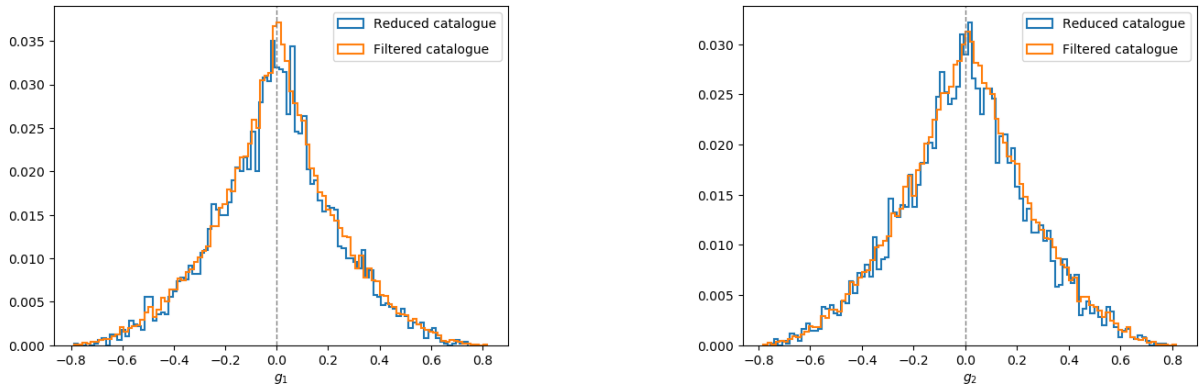

Figure 4.2: Histograms of normalised frequency comparing the distribution of intrinsic ellipticity, in its individual components, between the filtered COSMOS catalogue (orange), and the reduced sample (blue).

ticity distribution. Its individual ellipticity components are shown in Fig. 4.2, compared to the filtered COSMOS catalogue used as the input sample in Chapter 3. This comparison shows that the intrinsic ellipticity distribution is similar in both samples. Average values differ for the two catalogues, with the reduced sample being slightly negative ($\langle g_1 \rangle = -0.0014$, $\langle g_2 \rangle = -0.0016$, compared to $\langle g_1 \rangle = 0.0009$, $\langle g_2 \rangle = 0.0028$), with a dispersion of approximately 0.3. One thing that becomes clear with this figure is that this reduction introduced more variability in the distribution of source ellipticity. Particularly, g_1 in the reduced sample, shows a lack of sources with ellipticity between 0 and 0.05, and an excess around $g_1 = 0.07$. Although overall variations are kept under 1%, it is relevant to remember how the KSB method is susceptible to the pre-PSF shear of the source [51].

4.1.2 Dithering in *Euclid*'s observations

Due to the need for a large field-of-view, *Euclid* space mission will produce undersampled images and therefore distorted by aliasing. This effect occurs when the pixel spacing on a sensor undersamples the full range of spatial frequencies admitted by the optics [30]. It may be overcome by combining multiple, slightly displaced exposures of the same source, creating an oversampled, unaliased image, necessary to satisfy the scientific requirements for weak lensing measurements. Therefore, one of the main objectives was to quantify biases introduced during this dithering process, and due to the further stacking of these exposures. *Euclid*'s dither pattern is represented in Fig. 4.3, showing an "S" shape which corresponds to four dither positions, obtained by displacing the detector in small increments of $(\Delta x, \Delta y) = ((0,0);\ (50,100);\ (0,100);\ (50,100))''$.

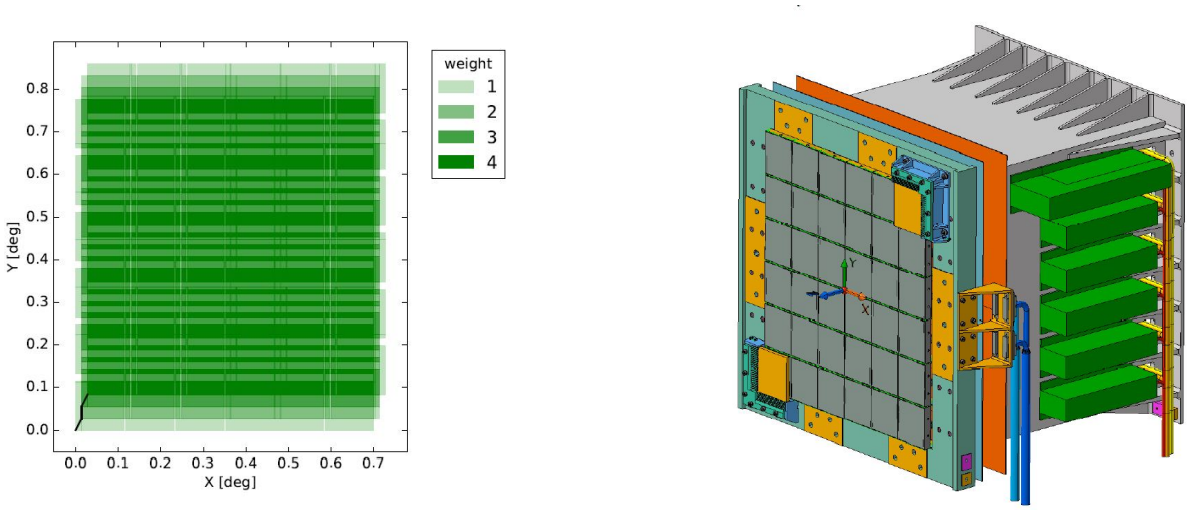

Figure 4.3: *Left panel*: Coverage of the VIS field-of-view. The default dither pattern in *Euclid* is 'S'-shaped, here shown by the black lines in the lower left corner. The weights show how many times an area has been observed. Each individual rectangle represents one of the 6×6 CCDs, to be used in VIS. Adapted from Ref. [32] *Right panel*: illustration of *Euclid*'s detector matrix. Reproduced from Ref. [33].

Apart from solving the aliasing issue, dithering is used in order to guarantee that the sky area falling in the gap between CCDs is also covered during the observation, so that all objects in the observed field-of-view can be detected. The size of these gaps is 12.7" between two columns of VIS CCDs and 64.6" between two rows of VIS CCDs. The "S" dither pattern ensures that 95% of the pixels in the image are covered by at least three of the four exposures [Euclid Collaboration: R. Scaramella et al, in preparation]. An illustration of the CCD matrix is shown in the right panel of Fig. 4.3, where it can be seen how the CCD configuration will result in undetected sky area. Another reason for this procedure is that it can increase the signal-to-noise ratio. By stacking the dithered exposures into one combined image, the resulting image will mimic the effect of a longer exposure time without loosing objects due to saturation of brighter sources. The duration of one *Euclid* VIS dither is defined as $t_{\rm exp} = 565$ s [31], so that the stacked image is equivalent to an exposure time of $t_{\rm exp} = 4 \times 565$ s. Beyond these two reasons, dithering is also used in *Euclid* images due to the inclusion of spectroscopic data in *Euclid*'s capabilities. These data will be obtained by rotating the spectroscopy system in different directions, so that lines from neighbouring sources do not overlap.

4.1.3 *Euclid*'s PSF modelling

As it became clear from the results of the calibration tests presented in Chapter 3, an accurate correction of PSF distortions is paramount when measuring the effects of cosmic shear. Therefore, it is crucial that the point-spread function of each telescope is modelled in great detail. In the case of *Euclid*, its PSF will be varying not only along the field-of-view [32], but also over time [33]. Due to *Euclid*'s broad band optical filter and to the fact that this mission will be diffraction limited, its PSF will also be highly wavelength dependent [34], which means that it will vary according to the galaxy SED.

Current modelling of *Euclid*'s PSF, is being implemented through the *PSFToolkit*, still under development [C. Duncan et al, in prep]. The access to this code was kindly provided by the development team at the University of Oxford, as this work is part of the EWC project, and it was used to produce the PSF images applied to the simulations described in Section 4.1.4. PSF FITS images built with *PSFToolkit* took as input values the coordinates for the different points in the field-of-view, given in degrees. Other

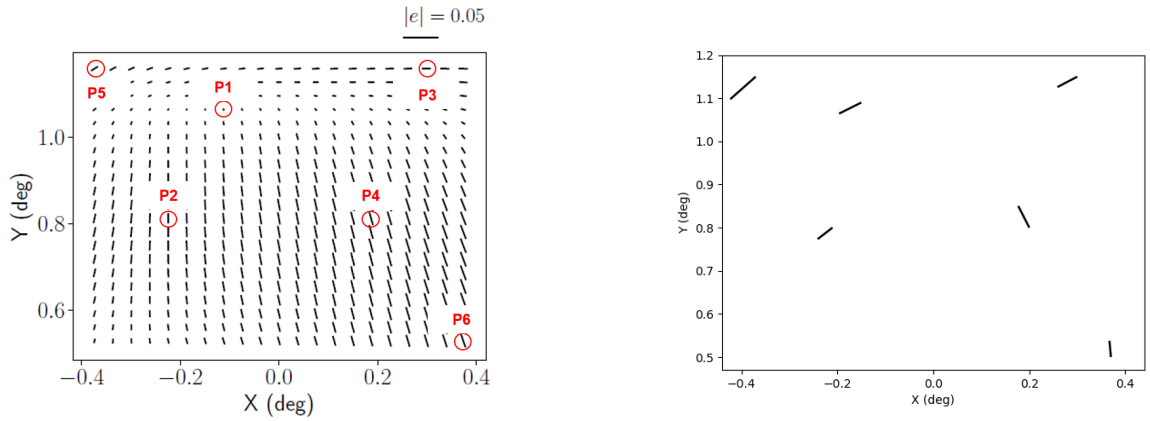

Figure 4.4: *Left panel*: Stick plot describing the variation in ellipticity across *Euclid*'s field-of-view (in degrees) for the nominal focus ($z = 0$). Figure from Ref. [32]. Red circles were added to show the six chosen positions used in the analysis of PSF variation along the field-of-view. *Right panel*: illustration of the actual measured PSF ellipticity corresponding to the PSFs obtained from the *PSFToolkit* using the position coordinates circled in red.

relevant parameters used by this toolkit, that were left on default, included a galaxy SED model, filter bandpass limits, and noise parameters (see Section 4.1.4).

In order to study the biases resulting from PSF variation along the field-of-view, six positions were chosen, based on the ellipticity plot shown on the left panel of Fig. 4.4, reproduced from [32]. These specific positions were chosen so as to include different regions of the FoV with varied PSF ellipticities. PSF images were then generated on those positions using *PSFToolkit*. However, when measuring the actual ellipticities of these generated PSF models, with the HSM module from *GalSim*, the resulting ellipticity values were as shown on the right panel in Fig. 4.4 and summarised in Table 4.1. These are the values that were used in the subsequent analyses, which do not always match the values expected from the left panel of Fig. 4.4. The corresponding PSF images generated with *PSFToolkit* are presented in Fig. 4.5.

In real observations, dithering is translated to a change in each source's position along the field-of-view, as the telescope moves according to the displacements defined for its dither pattern, as seen in Section 4.1.2. Since this work is based on shape measurements of individual objects instead of galaxy fields, dithering is simulated through the convolution of each galaxy's surface brightness profile with the PSF associated to each of the four dither positions, mimicking the effect of varying the galaxy position along the FoV, without having to change its position in the final image.

Table 4.1 summarises the ellipticity values of each PSF used to build the simulated *Euclid*-like images, measured by *Galsim*'s HSM module. Columns P1 to P6 correspond to the PSF models for each of the six chosen positions. Columns D1 to D4 are the ellipticity values for the individual dithers, done at position P6, with the last column corresponding to the combined PSF image, obtained from stacking all four dithered PSFs. It is possible to observe how this PSF model introduces very small changes to the PSF shape, when using mostly default parameters, so that the variation of PSF ellipticity in the dithering process for the remaining points of the FoV was equally small. Note that in the analyses here presented the PSF values are measured by HSM from the PSFs generated with *PSFToolkit* for a fixed value of the PSF model parameters. This is different from the realistic situation, where the PSF model parameters are calibrated from observations of star fields. These analyses do not include additional uncertainties arising from this calibration process. As cautioned by the *PSFToolkit* team, although some variation across de field-of-view is to be expected, the main factor responsible for rapidly altering the PSF shape is the effect

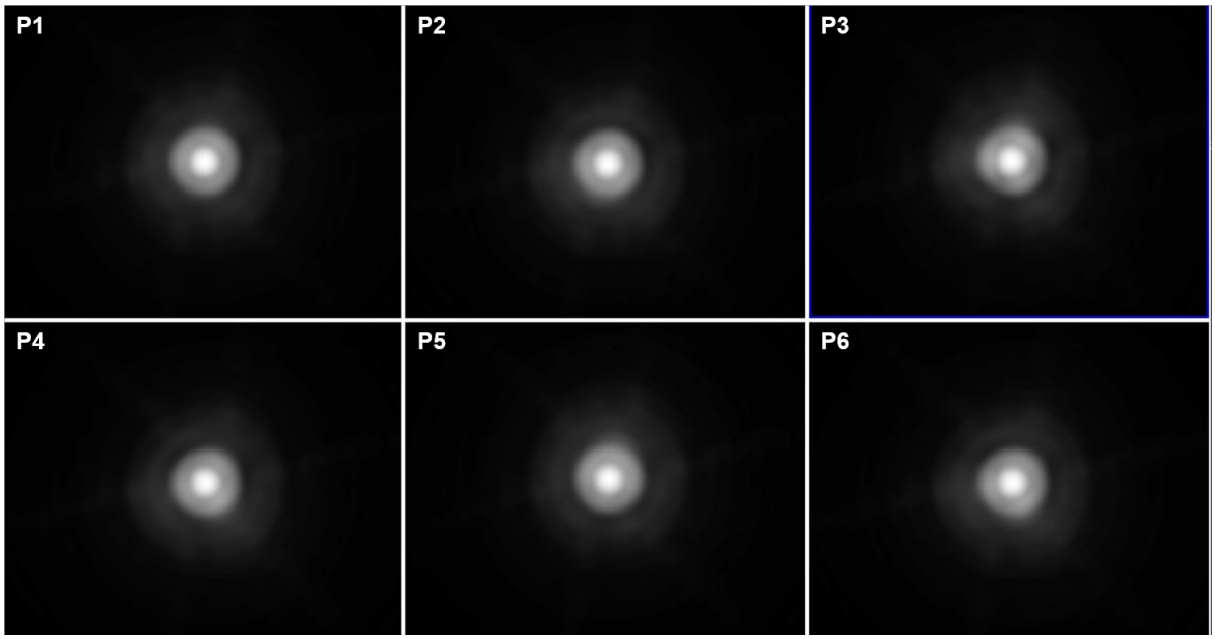

Figure 4.5: Model of *Euclid*'s PSF for each chosen point in the FoV, labelled from P1 to P6, displayed on a logarithmic scale.

Table 4.1: Summary of ellipticity values, as measured by the HSM module in *GalSim*, of all the PSFs produced with *PSFToolkit*.

g	P1	P2	P3	P4	P5	P6	D1	D2	D3	D4	Combined
$g_1(10^{-3})$	-7.22	-5.3	-6.5	-3.6	-9.5	-6.2	-6.2	-6.6	-6.9	-7.2	-6.9
$g_2(10^{-3})$	1.7	1.8	1.6	-3.3	3.6	-3.8	-3.8	-3.9	-3.7	-3.7	-3.9

of optical surface errors, which was not implemented in the model at the time of this work. Therefore, differences in PSF ellipticity between dithered exposures will be even smaller, as their displacements in the field-of-view are much less than the distance between the six chosen positions.

4.1.4 GalSim general configuration

Simulating *Euclid* data involved a similar procedure as in the previous calibration tests. The surface brightness profiles used when building the parametric galaxies were based on the reduced COSMOS catalogue, described in Section 4.1.1. An input shear was then applied to all galaxies in the same manner as before. Afterwards, all galaxy profiles were convolved with a PSF modelled after *Euclid*'s parameters, interpolated from FITS images, as described in Section 4.1.3. Since the simulated galaxy images presented in this chapter were built with two main purposes, they will follow slightly different methodologies regarding PSF convolution. The first objective was to evaluate the impact of *Euclid*'s PSF variation along the field-of-view on shape measurement bias. This entailed convolving the entire galaxy sample with six different PSF profiles, corresponding to six separate points in *Euclid*'s FoV, as illustrated by Fig 4.4. The exposure time for these simulations was defined as the duration of one *Euclid* VIS dither. The second objective involved studying the impact of dithering, where each galaxy was convolved with four different PSFs corresponding to each *Euclid* dither position. As was done for the previous test sets, the pixel scale was fixed at 0.1 arcsec/pixel, so as to mimic the pixel size in *Euclid*'s VIS instrument.

Regarding the noise model, the following simulations contain *CCDnoise* in place of *COSMOSnoise*

Table 4.2: Summary of *CCDnoise* parameters defined so as to simulate *Euclid*-like noise conditions.

Gain [e^-/ADU]	3.5
Read-out [e^-/pix]	5.4
Sky background [counts/pix]	114

used for the calibration tests. This combines detector characteristics, defined by its gain and read-out parameters, with Poisson noise from background contamination. The resulting images are taken to be already sky-subtracted, but where the added sky level contamination is propagated to the Poisson noise [35, 53]. Values for the parameters used in this noise model are defined in Table 4.2, and were based on previous works simulating *Euclid*-like conditions [54], as well as on default values used when building the necessary *Euclid* PSFs, using the *PSFToolkit* described in Section 4.1.3.

In order to study the biases introduced by image manipulation processes, different cases were simulated. The procedure used in each simulation case is illustrated in Fig. 4.6.

Case I is a single exposure, with $t_{\rm exp} = 565$ s, observed in six positions of *Euclid*'s field-of-view, as shown in Fig. 4.4, where galaxies are convolved with the PSF corresponding to each of the six points. Except for case I, all the other cases were performed in the position P6. Correction for PSF distortions, using the HSM module in *GalSim*, requires a PSF model as the input, which, in this case, was the true point-spread function. Case I evaluates the PSF variation along the field-of-view, while also representing the case of lowest signal-to-noise ratio.

Case II corresponds to four dithered exposures, stacked into one combined image. Galaxy profiles in each exposure were originally convolved with the respective dither PSF, however, the correction used a combined point-spread function, obtained by stacking the four individual PSF images. This case simulates a higher signal-to-noise ratio image, while showing the impact of correcting with an effective PSF that is not the one originally applied.

In case IId, each dither is convolved with its respective PSF, and afterwards corrected with the same originally convolved PSF. This produced four sets of shear measurements corresponding to the four dithers, which are then averaged, resulting in the final values for case IId. This case differs from case II in that the PSF correction was done individually using the corresponding convolved PSF.

Case III simulates a higher exposure time observation, with $t_{\rm exp} = 4 \times 565$ s, taken in one single position in the field-of-view. As in case II, the PSF convolved with the galaxy image is the PSF at that dither position, and the PSF used for correction is the combined PSF of the four dither positions.

Finally, case IV is similar to case II, with the exception that the PSF correction was done using one of the four dither PSFs (the first one). This case allows the comparison of two different realistic correcting methods. PSF correction can be done either by considering an effective PSF, which might be necessary in the case of only having the stacked images, or by choosing one of the dither PSFs for the correction.

4.2 Results and Discussion

4.2.1 Case I: PSF variation along the field-of-view

As described in Section 4.1.4, the surface brightness profiles used to build the parametric galaxies are based on the reduced COSMOS catalogue. A total of approximately 5000 sources was convolved with the *Euclid* PSF, modelled with *PSFToolkit*, corresponding to each of the six points in *Euclid*'s field-of-view, as defined in 4.1.3. Images in Case I were simulated with an exposure time of 565 s, corresponding

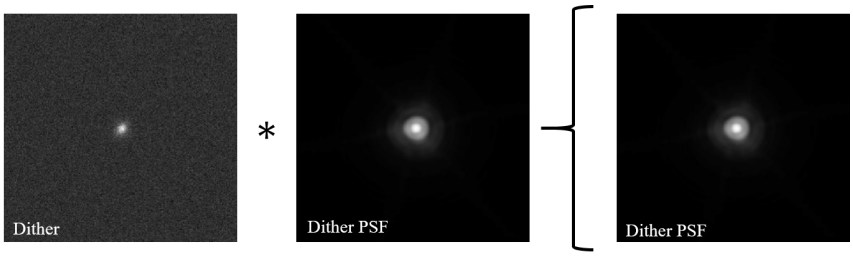

(a) Case I: Galaxy was convolved with the PSF corresponding to the chosen position in the FoV, and afterwards corrected with the same true PSF model.

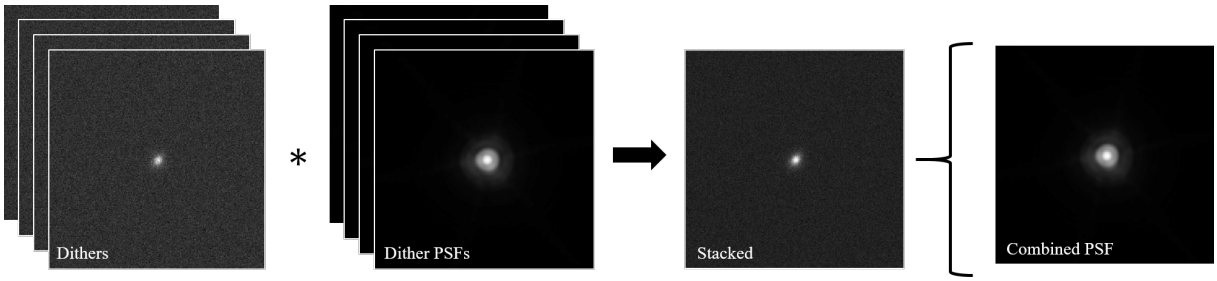

(b) Case II: Galaxy was convolved with each of the four dither PSFs, and combined into a stacked image. It was then corrected by the effective combined PSF.

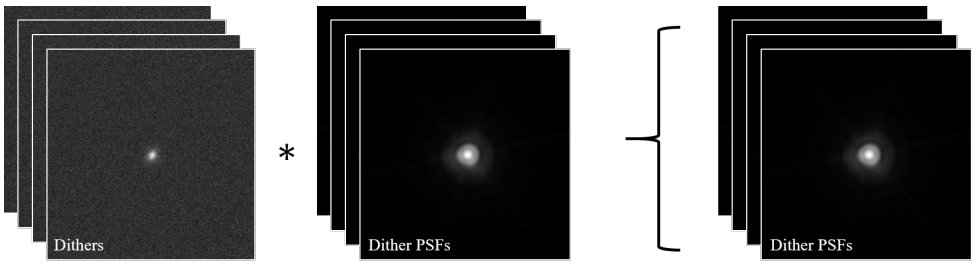

(c) Case IId: Galaxy was convolved with each of the four dither PSFs, and afterwards corrected with the same true PSF models.

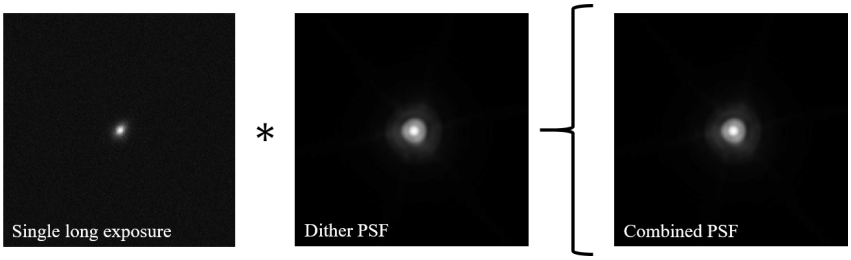

(d) Case III: Galaxy was convolved with one of the dither PSFs, and corrected by the combined stacked PSF.

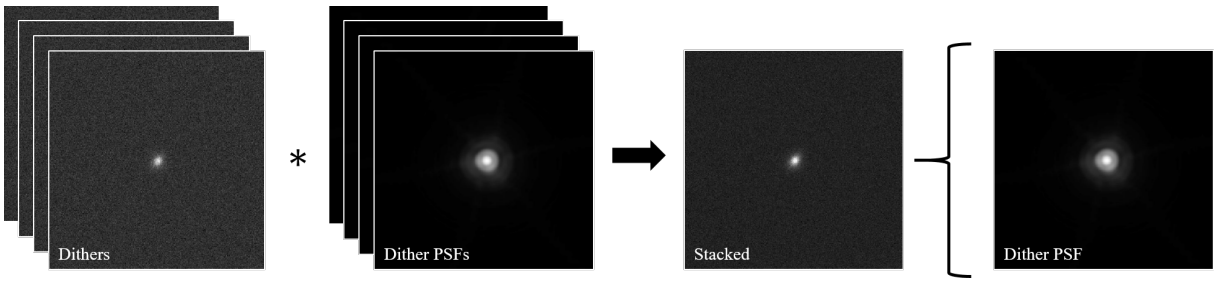

(e) Case IV: Galaxy was convolved with each of the four dither PSFs, and combined into a stacked image. It was then corrected by one of the dither PSFs.

Figure 4.6: Illustration of the procedures used to simulate different image manipulation conditions. Cases I to IV are shown.

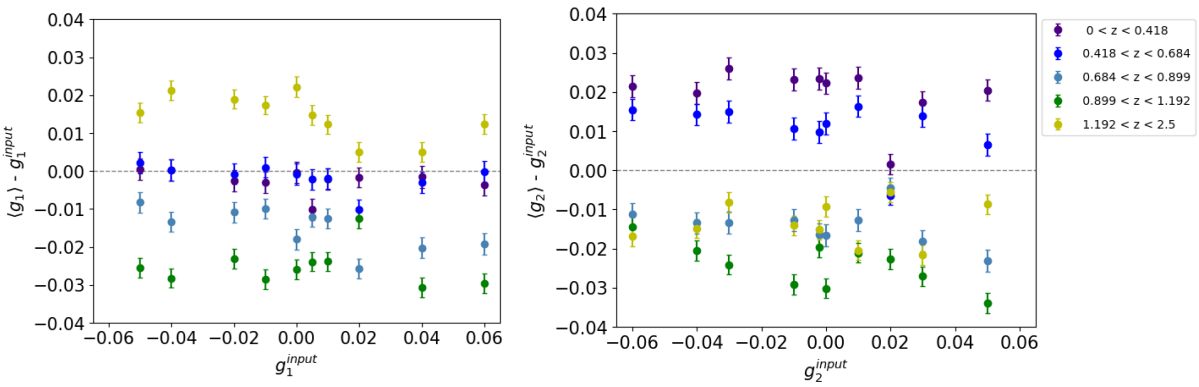

Figure 4.7: Results of the residual shear, for one position of the FoV, divided in its components g_1 (left panel) and g_2 (right panel), as a function of input shear signal. The different colours represent the different redshift bins, with each bin containing approximately 1000 galaxies.

to the duration of one *Euclid* VIS dither, and at each point in the field-of-view a set of input shear values was applied. The applied values were the same as the ones used in the tests of Chapter 3 (see Table A.1).

KSB measurements resulted in PSF-corrected shears for all six positions, which then allowed evaluating multiplicative and additive biases, following Eq. (3.7).

Dividing the sample in redshift bins, this time with bin edges defined by $z = \{0.001, 0.418, 0.684, 0.899, 1.192, 2.5\}$, returned a residual shear variation as presented in Fig. 4.7. This figure shows a consistent behaviour within each redshift bin as a function of input shear, with a more significant difference between redshift ranges than the one found in the previous calibration tests.

Variation of m and c values, due to binning the sample in redshift, magnitude, and size, is presented in Fig. 4.8. While a comparison can be made between the results from Section 3.3.2 and the ones shown in this figure, particularly regarding the behaviour of multiplicative bias, trends in the variation of bias as a function of each of the sample's properties are harder to distinguish. The absence of a clear separation between ellipticity components associated to the additive bias, as seen in Chapter 3, can be explained by the differences in the PSF model applied in both simulations. One thing that becomes clear when analysing Fig. 4.8, is that, even after excluding values of measured shear responsible for introducing abnormal deviations, both multiplicative and additive biases are still too high to allow an accurate study of the impact of PSF variation along *Euclid*'s field-of-view. The measurements here presented are most likely being affected by the reduction in galaxy sample. Since the reduced catalogue represents 10% of the filtered COSMOS catalogue used in Chapter 3, binning has divided the sample in sets containing approximately 2% of the sources, which was aggravated by the necessary exclusion of the outlier shears, resulting in each bin containing less than 1000 galaxies. The downsize in the number of observations for the binned analysis, in combination with the intrinsic variability in galaxy properties within bins, appear to be the most significant factors for the abnormal values of bias illustrated in Fig. 4.8.

Since no significant trend with the physical properties of the sample was found during the analysis in Chapter 3, the following work will make use of the full reduced sample of 5000 galaxies, in order to get better statistics.

Results for the residual shear offset, as a function of input shear, are presented in Fig. 4.9. Computing the averages over the entire sample appears to have minimised, in part, the impact of the additional errors due to binning. As expected, due to the small ellipticity variation of *Euclid*'s modelled PSF, the response to the convolution with each position's PSF is translated to a similar behaviour regarding residual shear.

Following the same procedure as before, a representation of the fitted values for the multiplicative

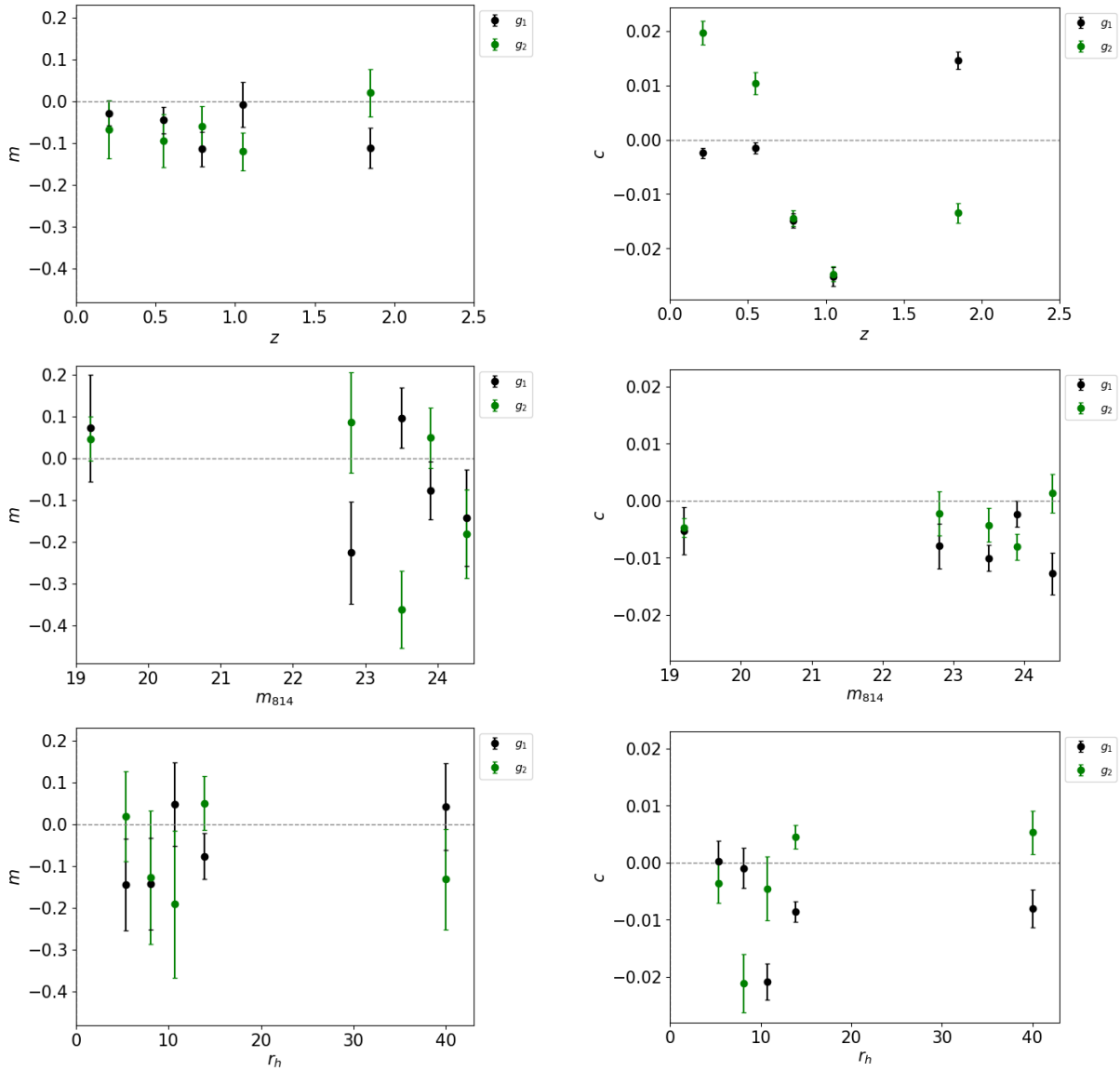

Figure 4.8: Variation of multiplicative (left panels) and additive (right panels) biases as a function of redshift (top row), magnitude (middle row), and half-light radius (bottom row), in one position of the FoV, for the reduced sample binned in these three properties.

and additive biases is given in Fig. 4.10, with the explicit values summarised in Table C.1. The six points on the left of the dashed line represent the g_1 component of all six field-of-view positions, whereas points on the right of this line correspond to the respective g_2 value, with each colour being associated with a different point. As observed in this figure, and following the same trend found during the calibration tests, the first shear component appears to be more affected by additive bias than the second one, with average values across the FoV of $\langle c_1 \rangle = -9.26 \times 10^{-3}$, and $\langle c_2 \rangle = -2.93 \times 10^{-3}$. This can be explained by the overall higher (negative) ellipticity of the g_1 component of the applied PSF models. Although the second ellipticity term of the PSF is positive in most positions, c_2 is still mostly negative, which may be reflecting a cross contamination between ellipticity components [51]. Regarding multiplicative bias, the second shear component shows an overall higher m, with the averages being $\langle m_1 \rangle = -1.34 \times 10^{-2}$, and $\langle m_2 \rangle = -2.77 \times 10^{-2}$.

Comparing the fitted values for the residual shear offset, from Fig. 4.10, to the respective PSF ellipticities, in Table 4.1, shows that even after correcting for PSF distortions, biases are still too high, with

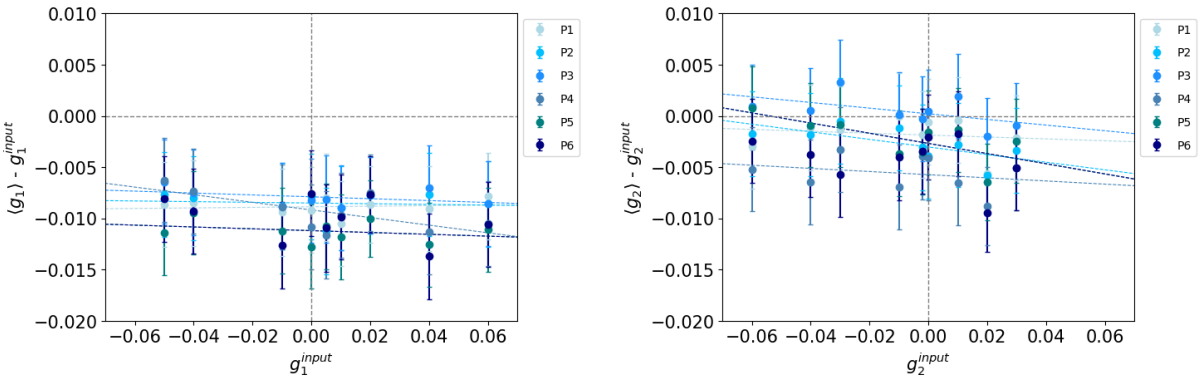

Figure 4.9: Results from the residual shear, divided in its individual components g_1 (left panel) and g_2 (right panel), as a function of input shear signal. The different colours represent the 6 chosen positions in the FoV. Each point represents an average over approximately 5000 galaxies.

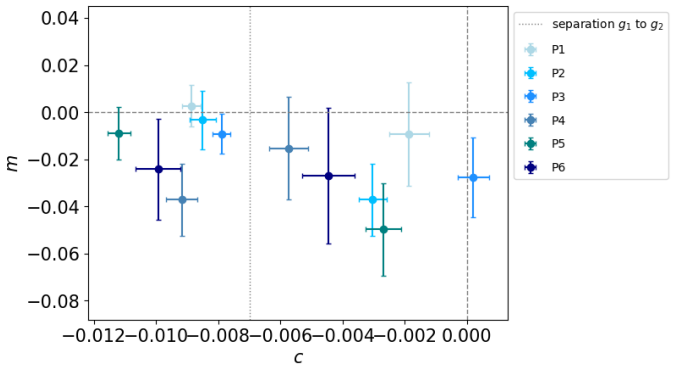

Figure 4.10: Fitted values of multiplicative and additive biases for each position in the field-of-view. Points with the same colour represent components g_1 and g_2 of the same position.

the additive bias being higher than the original PSF effect itself. Considering the fact that additive biases are mainly introduced by the PSF anisotropic component, this indicates a systematic effect beyond the expected PSF residuals. Since the observed ellipticity of a source is a combination of PSF distortion, input cosmic shear, and intrinsic ellipticity, after correcting the PSF effects and subtracting the known input shear, the final shape will be a reflection of original source shape and residual additive bias, resulting from the PSF correcting method. The usual procedure is to assume that galaxies are randomly oriented in the sky so that the average intrinsic ellipticity is zero, but, as seen in Section 4.1.1, due to the catalogue reduction, this intrinsic ellipticity is no longer zero, but of the order of c. This too was taken into consideration in the presented results, with the mean intrinsic ellipticity being subtracted from the PSF-corrected shears. Therefore, the high additive bias appears to be a combination of the contribution of several factors. Reducing the number of objects in the catalogue affected the average intrinsic ellipticity, which in turn directly impacted on the measured c values. However, even after subtracting this value from the measurements (and excluding values satisfying $|g| > 1$), the additive bias must have already been contaminated due to a poor correction of highly elliptical sources [51], as this correction is done to each object, individually.

Nonetheless, it is still possible to observe how the PSF variation along *Euclid*'s field-of-view can impact the measured biases, even with a model producing very low ellipticity variation. These biases will then affect the constraint of cosmological parameters, as studied in the next chapter.

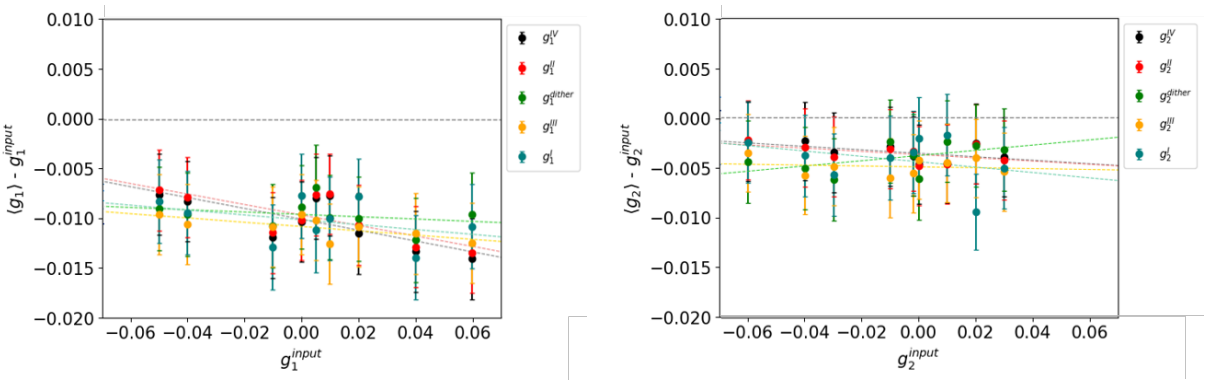

Figure 4.11: Results of the residual shear, divided in its individual components g_1 (left panel) and g_2 (right panel), as a function of input shear signal. The different colours represent each of the considered cases of image processing procedures.

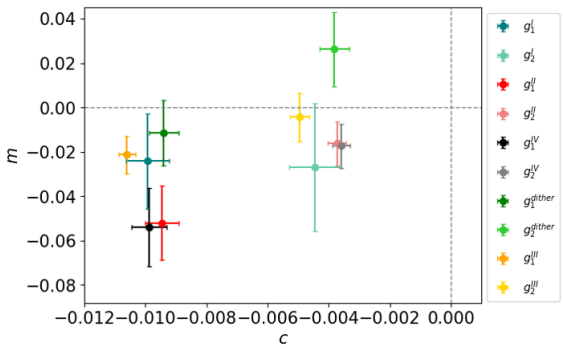

Figure 4.12: Fitted values of residual shear offset and shear multiplicative bias for each case. Points with the same colour represent components g_1 and g_2 of the same procedure.

4.2.2 Cases II, IId, III, and IV: Bias resulting from image manipulation

Images in cases II, IId, III, and IV were simulated as illustrated in Fig. 4.6. As before, all 5000 sources were convolved with the corresponding PSF models, as described in Section 4.1.3. A total of thirteen shear input values were applied to these images, with some of the KSB corrected shear values being excluded for the reasons mentioned above. The sample's average intrinsic ellipticity was also subtracted from these measurements, as was done for the results presented in Section 4.2.1.

Variation of residual shear, as a function of input shear signal, corresponding to each of the described cases is presented in Fig. 4.11. As seen in Table 4.1, due to the small variation in the shape of the applied PSF model, the four PSFs associated to each dither position are very close in ellipticity. This results in a similar behaviour regarding residual shear offsets between the different simulations. Fitted values for the multiplicative and additive biases are presented in Fig. 4.12, with the explicit values summarised in Table C.2. Each colour represents a different case, with the darker and the lighter tones corresponding to the first and second ellipticity components, respectively.

It is now possible to evaluate the impact that different image manipulation procedures have in the values of m and c. As observed in Fig. 4.12, cases II and IV show similar values for the estimated biases, as both simulations involve the stacking of the same dithered images. Since, in both cases, the convolved PSFs are different from the models used for the KSB correction, neither will reflect an exact PSF subtraction. These two cases also simulate the same noise level, corresponding to an exposure time of four times the duration of one dither exposure ($t_{\rm exp} = 4 \times 565$ s). Case I represents the lowest case of signal-to-noise ratio, as the exposure time is the shortest, which is reflected in the respective error bars.

Case III, on the other hand, has the smallest uncertainty, as it also represents the longest exposure time in one single observation. Case IId was computed by averaging the measured PSF-corrected shears from each individual dither, thus being affected by the same amount of noise as case I. The result from this averaging mimics the effect of stacking, as the information from the same source is computed four times. While this method is more affected by noise, it improves in PSF correction, as this is done using the true convolved PSF, individually in each dithered image.

Overall, multiplicative bias appears to significantly vary depending on the choice of PSF model used when applying the KSB algorithm, with the most affected cases being the ones where an effective PSF, different from the true convolved on, was applied. This bias associated to the g_2 shear component also appears to depend on the level of noise present in the images, with cases I and IId producing higher $|m|$ values. Regarding additive bias, there is a clear separation between the two ellipticity components, deriving mainly from the applied PSF models, as seen in previous results, without a significant effect of dithering, and stacking, in the results for this bias. While it might be expected that correcting for an effective combined PSF would result in larger residual errors, the shape similarity between this PSF and the dithered PSF models decreases the impact on the correcting bias. The overall effect in additive bias appears to be, as seen in the previous results, due to systematics resulting from the combination of errors introduced by the KSB method application, and a reduction in the number of galaxies.

Since biases in shear measurements can directly impact the constraint of cosmological parameters, the next chapter presents an analysis of the impact that the biases resulting from PSF variation along the field-of-view, as well as from the different cases here considered, have in the constraint of Ω_m and σ_8 parameters.

Chapter 5

Impact of shear measurement biases on the constraints on cosmological parameters

5.1 Cosmic shear as a cosmological probe

Cosmological models aiming to describe the composition and dynamics of the Universe will have to fit the high-precision data that has been gathered so far. The increasing precision and accuracy of observational cosmology has contributed to a complex parametrisation of such models, reflected in the definition of a wide range of cosmological parameters. The values of these parameters are estimated through the measurement of observable quantities. These observables are usually dependent on more than one cosmological parameter, resulting in degeneracies, since different values of the vector of parameters can produce the same observable quantity. However, different types of observations are sensitive to different combinations of cosmological parameters, allowing to break these degeneracies [55].

The two major categories of cosmological probes are related with the geometry of the Universe and its structure. Observables associated with geometrical properties, such as distance modulus from supernovae Ia, probe the dynamics and evolution of the homogeneous Universe, whereas structure-related observables probe the formation and distribution of matter at large scales (inhomogeneous Universe). Examples of structure probes include gravitational lensing, CMB anisotropies, and galaxy clustering.

Being a consequence of weak gravitational lensing, cosmic shear is also a structure probe, where the observable quantity is the amount of distortion affecting the observed galaxy shapes. As described in previous chapters, this distortion is estimated by measuring correlations in ellipticity between galaxy pairs in an image, and it is associated with the amount of total matter, acting as a lens, affecting the light's trajectory towards the observer.

As seen in Section 2.4.1, the factor before the integral, in Eq. (2.34), shows the direct relation of P_γ with Ω_m, resulting from the Poisson equation. The shear power spectrum is also related to σ_8 through the direct dependency of P_δ with this quantity. As such, the cosmic shear estimator is strongly related to the gravitational potential produced by both luminous and dark matter, therefore being highly correlated to the cosmological parameter Ω_m, and to the amplitude of the matter power spectrum, σ_8.

In addition to probing the matter content in the Universe, independently of its nature, cosmic shear is also sensitive to the evolution of dark energy, as this component affects the evolution of the matter power spectrum [56]. Therefore, it is possible to constrain dark energy parameters, such as w_0, through the measurement of weak lensing distortions across different redshift ranges, for which accurate source redshift determination is necessary.

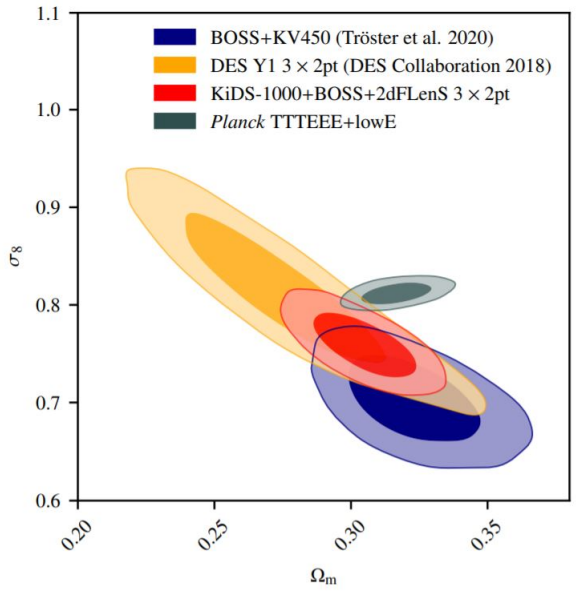

Figure 5.1: 68% and 95% confidence level contours in the Ω_m - σ_8 plane, comparing the joint analysis from KiDS-1000 with BOSS and 2dFLens (red), with the analysis from DES Y1 (yellow) [57], and a previous joint analysis of BOSS and KV450 (blue) [58]. CMB constraints are also presented for comparison (grey) [23]. Reproduced from Ref. [59].

Constraint contours in the Ω_m - σ_8 plane are shown in Fig. 5.1, resulting from the analysis of data from different cosmological probes, specifically from weak lensing measurements from the Kilo-Degree Survey (KiDS-1000), redshift-space galaxy clustering observations from the Baryon Oscillation Spectroscopic Survey (BOSS), and galaxy-galaxy lensing data from the overlap between KiDS-1000, BOSS and the spectroscopic 2-degree Field Lensing Survey (2dFLenS). Figure 5.1 also includes the constraints imposed by *Planck* measurements of the CMB, and both galaxy clustering and weak lensing data from the Dark Energy Survey (DES), allowing a broad overview of the constraining capabilities of the different cosmological probes.

The weak lensing constraints show a well-defined degeneracy in this plane, due to the dependence on the two parameters, as shown in Eq. (2.34). The weak lensing contours from the various datasets are curved (non-elliptical) contours along a line $\sigma_8 = \text{constant} \times (\Omega_\text{m}/0.3)^\alpha$, where the value $\alpha = -1/2$ is a good fit to the direction of the degeneracy, and $\Omega_m = 0.3$ is used for normalisation. The value of the constant models how high in the plane the contour is. This constant defines the S_8 parameter, i.e.,

$$S_8 = \sigma_8 \sqrt{\Omega_m/0.3}. \tag{5.1}$$

The weak lensing contours can then be summarised by one parameter S_8, and its uncertainty tells about the width of the contours.

On the other hand, the early Universe observations from *Planck* give a different constraint, since they depend in a different way on the two parameters. They have thus the potential to break the Ω_m - σ_8 degeneracy and enable individual strong constraints on both parameters. However, some discrepancies, or 'tensions', exist between *Planck* data and the other surveys. In Fig. 5.1, it is clear that its contour barely overlaps with the late-time observations of large-scale structure. Results from *Planck* observations would be consistent with a WL-type contour with $S_8 = 0.834 \pm 0.016$ [23]. This is a 3.1σ tension with the value of S_8 of the KiDS-1000 contour ($S_8 = 0.766^{+0.020}_{-0.014}$) [59] and a 2σ tension with DES $S_8 = 0.783^{+0.021}_{-0.025}$)

[59]. The tension with the combined result from BOSS and KV450 is a higher 3.4σ, since the blue contour is even lower in Fig. 5.1 ($S_8 = 0.728 \pm 0.026$) [59]. The difference between the *Planck* S_8-equivalent value and the other S_8 values quoted is thus in the range $0.05 - 0.10$.

While S_8 tensions might be attributed to statistical fluctuations, the increasing accuracy of the most recent observations combined with large-scale analysis such as the one shown in Fig. 5.1, shows that other explanations might be necessary to justify the existent tensions. Beyond a statistical effect, these discrepancies might be evidence of systematic errors that are not being taken into account, or a reflection of the need for new physics.

5.2 Methodology

5.2.1 The likelihood function

As both the quantity and quality of cosmological data have been rapidly evolving over the years, the choice regarding the best methods for data analysis has also become an increasing concern. Among many reasons, this concern arises due to the accuracy of such large-scale datasets being limited, not only by technological capabilities, but also by the efficiency in removing systematic effects during data analysis.

In contemporary cosmology, the standard approach to the analysis of such datasets is through a Bayesian approach that aims to find the conditional probability of the model given the observed data. This probability is called the posterior, $p(\Theta|D)$, where Θ represents the set of parameters in which the model is based, and $D = \{x_1, x_2, ..., x_i\}$ is a specific dataset [55].

Based on Bayes' theorem, the posterior distribution can be transformed into the likelihood function

$$p(\Theta|D) = \frac{p(D|\Theta)\, p(\Theta)}{p(D)}, \tag{5.2}$$

where $p(D|\Theta) = L(\Theta)$ is the conditional probability of an experiment resulting in a specific dataset D given a particular cosmological model of parameters Θ, i.e., the likelihood of the model. In this way, the posterior distribution can be found from a likelihood evaluation of the model parameter space, assuming $p(D)$ and $p(\Theta)$ are known. $p(D)$ is the probability of the data. Being independent of the model, it is just a normalisation in the parameters' space, and so it is irrelevant when comparing values of the posterior in different points of the parameter space. $p(\Theta)$ is the probability of the model independently of the data, thus corresponding to an external restriction on the models, coming from prior data or any type of assumptions. Priors are commonly taken to be a top-hat or a Gaussian distribution in an interval of assumed values for the parameters.

Considering an arbitrary likelihood function which depends on a set of cosmological parameters, the best-fit values for the model's parameters correspond to the position in the parameter space with the maximum value for the posterior, obtained by computing

$$\frac{\partial L(\theta_i)}{\partial \theta_i} = 0, \qquad i = 1, 2, ..., n. \tag{5.3}$$

The errors associated to the parameters' estimates are thus determined by the width of the likelihood surface around this maximum, corresponding to the confidence regions, $R(\alpha)$, as defined in Eq. (5.4).

$$\int_{R(\alpha)} L(\theta_i)\, d^n\theta = \alpha. \tag{5.4}$$

The region $R(\alpha)$ is the area for which the integral below evaluates to $0 < \alpha < 1$, assuming a normalised posterior. The typical choices are $\alpha = 0.683, 0.954, 0.997$, also denoted as $1\sigma, 2\sigma$, and 3σ.

5.2.2 *nicaea*: overview and configuration

In order to evaluate the impact that the previously measured biases might have on cosmological parameter constraints, it is first necessary to define the observables to use in the cosmological analysis. This work uses the two-point shear correlation functions between galaxy pairs. The previous chapters focused on individual images of galaxies produced with *GalSim*. No field of galaxies was simulated and this work did not produce simulations of correlation functions. The objective of the previous analyses was to study the biases on the shear estimates, and the next step is to propagate those biases to two-point shear correlation functions.

To do this, the approach was to use the public code NumerIcal Cosmology And lEnsing cAlculations (*nicaea*)[5] to compute theoretical two-point shear correlation functions for expected *Euclid* observing conditions, and then transform them according to the previously found biases. It is then possible to perform a likelihood analysis on a parameter space, comparing biased correlation functions to unbiased theoretical correlation functions, such as to constrain the cosmological parameters' values that fit the biased data.

nicaea is a C-code that provides numerical routines used to compute cosmology related quantities from theoretical models of the large-scale structure [60]. It is the base of the cosmology module in the CosmoPMC package[6], which uses a Monte-Carlo sampling method to explore the likelihood of various cosmological probes. In this thesis, however, *nicaea* was used as a standalone module to calculate weak lensing observables. Among the functionalities supported by *nicaea*, is the ability to compute second and third order shear statistics, as well as matter power spectra, in light of an input cosmological model, specified by the definition of a set of cosmological parameters, redshift bins, and angular scales.

For this work, *nicaea* was used specifically to compute the weak lensing two-point correlation functions of galaxies following a *Euclid*-like redshift distribution, calculated from the matter power spectrum, as described in Section 2.4.1. The angular scales in which the correlation functions were evaluated were defined as ten bins logarithmically spaced between $0.1'$ and $300'$, following the analysis of [61]. The two lowest bins of ξ_- and the two highest bins of ξ_+ were discarded for the reasons explained in [61], that mainly derive from limitations in the simulations that were used in that work. This resulted in eight bins centred on $(0.15', 0.33', 0.74', 1.65', 3.67', 8.17',\ 18.20', 40.54')$ for ξ_+, and $(0.74', 1.65', 3.67', 8.17', 18.20', 40.54', 90.27', 201.03')$ for ξ_-.

To perform a likelihood analysis, not only the correlation function data vector is needed but also its covariance matrix. This analysis uses the covariance matrix obtained by *Euclid*'s High-Order Weak Lensing Statistics project (HOWLS) [N. Martinet, private communication]. This covariance matrix was obtained by computing the dispersion of correlation functions measured in 256 lensing maps of size 5×5 degree each, produced with the DUST-Grain simulations [62]. Since the correlation functions used for computing the covariance matrix were measured at the angular scales defined in [61], this work also followed that same prescription when defining the angular scales for these analyses. The HOWLS maps were created with the same redshift distribution of *Euclid*'s observations and thus have a comparable shear signal (see Eq. (2.34)). They were also created with the same expected galaxy density of the *Euclid* survey, which is an important factor to determine the noise of the experiment (see Eq. (2.42)). However,

[5] `https://github.com/CosmoStat/nicaea`
[6] `https://github.com/CosmoStat/CosmoPMC`

the $25\ \mathrm{deg}^2$ maps are much smaller (by a factor of 600) than the expected area of *Euclid* ($15000\ \mathrm{deg}^2$), and therefore in order to be able to use this covariance matrix to simulate *Euclid*'s confidence levels, a rescaling was introduced during the likelihood calculations.

The HOWLS maps were constructed from N-body simulations with the cosmological parameter values shown in Table 5.1. The choice for these values was based on the latest release of the *Planck* Collaboration analysis [23], except for Ω_m, Ω_Λ, and σ_8, which were defined based on weak lensing observations [62]. The covariance matrix is only weakly dependent on the choice of these values.

Table 5.1: Summary of cosmological parameters set as default, for the unbiased case, in the configuration of *nicaea*.

Ω_m	0.313
Ω_Λ	0.687
h_{100}	0.67
σ_8	0.842
n_s	0.96
w_0	-1.03

5.2.3 Biased correlation functions and parameters' space sampling

As has been mentioned throughout this thesis, real cosmological data are affected by bias, and this also applies to measurements of the cosmic shear estimator. Starting by defining the fiducial model, this is a vector with 16 values, corresponding to ξ_+ and ξ_- calculated in 8 angular bins, computed with *nicaea* for the fiducial cosmology of Table 5.1. The fiducial covariance matrix is the 16x16 matrix obtained for this cosmology in the HOWLS project, and it was from this fiducial (unbiased) data vector, that the biased data vectors were built. The first step was to add the measured m and c values for each case, as summarised in Table C.2, to the unbiased correlation functions measured by *nicaea*, thus simulating the observations of a biased weak lensing experiment. The shear correlation functions in the presence of the shear m and c biases were derived by computing Eq. (2.30) using Eq. (2.44) written as $\hat{\gamma}_i^{obs} = \gamma_i^{true}(m_i + 1) + c_i$, resulting in

$$\xi_{ii}(\theta) = \langle \gamma_i \gamma_i \rangle(\theta), \qquad i = 1, 2.$$

$$\begin{aligned} \langle \gamma_i^{obs} \gamma_i^{obs} \rangle &= \langle (\gamma_i^{true}(m_i + 1) + c_i)(\gamma_i^{true}(m_i + 1) + c_i) \rangle \\ \Leftrightarrow \langle \gamma_i^{obs} \gamma_i^{obs} \rangle &= \langle \gamma_i^{true} \gamma_i^{true} \rangle (m_i + 1)^2 + c_i^2 + 2c_i(m_i + 1)\langle \gamma_i^{true} \rangle, \end{aligned} \tag{5.5}$$

where it is assumed that $\langle \gamma_i^{true} \rangle = 0$. Then, using the definition given in Eq. (2.31), ξ_+ and ξ_- become

$$\xi_\pm^{obs} = (\xi_+^{true} + \xi_-^{true}) \frac{(1 + m_1)^2}{2} \pm (\xi_+^{true} - \xi_-^{true}) \frac{(1 + m_2)^2}{2} + c_1^2 + c_2^2. \tag{5.6}$$

The type of biases presented in Chapter 4, resulting from different image manipulation procedures, are usually corrected in real data. If the biases found from simulations are removed from the measured correlation functions, then the measurements become unbiased, and there is only a decrease in the signal-to-noise ratio that accounts for uncertainties in the correction. However, the work presented in this chapter aims to evaluate a different impact, by comparing the biases introduced in the different scenarios defined in Chapter 4. As an example, considering case IV (where the shear is estimated by deconvolving

the stacked image with an individual PSF) and case II (where the shear is estimated by deconvolving the stacked image with the dither-combined PSF). These two procedures introduce different values of bias, as seen in Chapter 4. It is debatable which is the optimal or correct way to proceed. So even if the bias introduced by one of the shear estimation methods is completely removed, the result is still biased with respect to what would be obtained if the other method had been applied. This is called a residual bias, and the objective of this analysis is to find out if the residual bias between pairs of valid and realistic data processing methods may have a meaningful impact in the cosmological parameters constraints.

The results from the impact of residuals remaining from the PSF variation along the field-of-view are also presented in this chapter.

As discussed in the previous chapters, additive biases appear to be the dominant systematics throughout this work, regardless of simulation conditions. For that reason, when applied to Eq. (5.6), the effect of additive bias dominates the position of the posterior distribution, introducing a high deviation from the unbiased model, unrelated to the realistic impact from PSF variation. Since it has been established that the obtained values for the additive bias were strongly affected by sample conditions, and do not reflect an accurate effect of PSF variation, additive biases will be set as $c = 0$ in the following section and the analysis will focus on the impact of the residual m bias.

To propagate the residual bias to the parameters constraints, two biased vectors are built from the fiducial data vector, inserting the values of m_1, and m_2 of the two cases under comparison in Eq. (5.6). This approach allows building a "theoretical" biased data vector (corresponding to the method assumed to be the correct one), and an "observed" biased data vector (corresponding to the method assumed to be the one applied in the measurements). The two methods under study are interchangeable and either of them could be considered the theoretical or the observed case. The cosmological parameters' space is then sampled by computing the likelihoods of "theoretical" models produced by *nicaea* (with m and c values fixed for that case) with respect to the "observed" model (that remains with all parameters, cosmological and bias, fixed).

The likelihood of a theoretical model given the observed one (assuming as usual that the statistical properties of the observed data can be modelled by a Gaussian distribution) is given by

$$L \approx N \exp\left[-\frac{1}{2}(\xi_{\mathrm{i}}^{\mathrm{obs}} - \xi_{\mathrm{i}}^{\mathrm{th}})^{\top}\, \mathrm{C_{ij}}\, (\xi_{\mathrm{j}}^{\mathrm{obs}} - \xi_{\mathrm{j}}^{\mathrm{th}})\right]. \tag{5.7}$$

The sampling of the parameter space was done by building a grid and evaluating Eq. (5.7) for each point of this grid. The values of ξ^{obs} were fixed while ξ^{th} was computed with *nicaea* for each point of the grid.

For this part of the work, a two-dimensional parameter grid was built, by varying the values of Ω_m and σ_8 introduced in *nicaea*'s configuration. Since weak lensing is more sensitive to these two cosmological parameters, this analysis focused only on their variation. Choosing Ω_m and σ_8 also allows studying the impact of shear biases on the S_8 tension. Two main grids were used, the first one being larger and with lower resolution, defined by $\Omega_m = [0.1 - 0.4]$, and $\sigma_8 = [0.6 - 1.1]$. This broad range of values permitted locating the maximum likelihood position, as in some cases the difference between the theoretical and observed correlation functions was too large, pushing the contours outside of the grid. After locating the maximum likelihood region for each case, another higher resolution grid was defined by setting $\Omega_m = [0.29 - 0.34]$, and $\sigma_8 = [0.81 - 0.87]$. This compromise between resolution and grid scale was necessary due to limitations in both computation time and power.

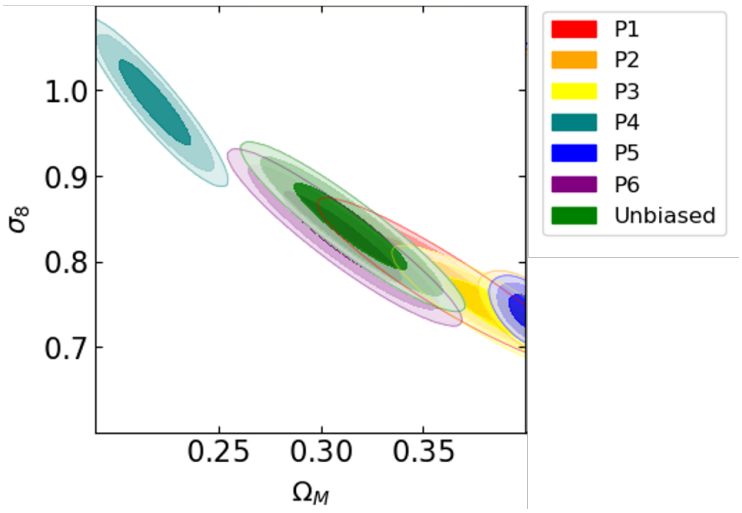

Figure 5.2: Marginalised posterior distribution in the $\Omega_m - \sigma_8$ plane, comparing the simulated unbiased ΛCDM constraint (green) with the confidence regions evaluated for different points in the field-of-view, with the respective colours identified in the label.

5.3 Results and Discussion

5.3.1 Impact from PSF variation

In order to evaluate the impact of residual errors resulting from *Euclid*'s PSF variation along the field-of-view, biased correlation functions were computed according to Eq. (5.6), by adding the values of the multiplicative biases found in Section 4.2.1, and summarised in Table C.1. The results from the marginalised posterior distributions are presented in Fig. 5.2, comparing the unbiased ΛCDM model with the constraints found for the biased likelihoods in each considered position in the field-of-view.

As defined in Table 5.1, the unbiased confidence regions are centred around $\Omega_m = 0.313$ and $\sigma_8 = 0.842$, corresponding to previously constrained parameters for a ΛCDM model. The maximum likelihood values for the different biased cases, shown in Fig. 5.2 and summarised in Table 5.2, show a wide range of measured $\Omega_m - \sigma_8$ pairs, generally along the same line of degeneracy as the unbiased model. Since the grid used for this part of the work did not have enough resolution for a *Euclid* rescaling, these results were rescaled by a factor corresponding to the KiDS survey area (1000 deg^2).

Apart from the maximum likelihood values for Ω_m and σ_8, Table 5.2 summarises the results of S_8, computed for each position in the field-of-view, following Eq. (5.1), and the corresponding ΔS_8 values calculated relative to the unbiased case. This last quantity can be used as a distance measure between the results from the varied positions and the unbiased model, showing a consistent behaviour as the one seen in Fig. 5.2, with the apparent exceptions of P_3 and P_6. Although the constraint contour associated with P_6 appears as the closest one to the unbiased model, its value of ΔS_8 defines it as the second furthest case. Similarly, P_3 might be expected to show a ΔS_8 value higher than the one obtained for P_1. As S_8 reflects the combined effect of Ω_m and σ_8, being constant along the line of degeneracy of these two parameters, biases deviating the maximum likelihood regions orthogonally to this line appear to have greater impact on the values of ΔS_8. This may explain the apparently unexpected offset of positions 3 and 6 regarding the unbiased model. As points P_1, P_2, P_3, and P_5 lower the estimate for σ_8 while increasing Ω_m, along the degeneracy line, both P_4 and P_6 follow the opposite direction. The behaviour shown by P_4 and P_6 may be related to the fact that these two positions are the only ones with a PSF model described by two negative shear components, while the remaining positions are characterised by

Table 5.2: Results from biased model performance represented by ΔS_8, as well as maximum likelihood parameter values for Ω_m and σ_8, obtained with the module *getdist*.

	$\Omega_m \pm \Delta\Omega_m$	$\sigma_8 \pm \Delta\sigma_8$	S_8	$\Delta S_8(\%)$
Unbiased	0.315 ± 0.014	0.841 ± 0.025	0.859	0.0
P_1	0.359 ± 0.017	0.779 ± 0.024	0.863	0.4
P_2	> 0.396	< 0.746	0.872	1.5
P_3	$0.383^{+0.016}_{-0.013}$	< 0.752	0.859	0.0
P_4	0.219 ± 0.009	> 0.973	0.819	4.7
P_5	> 0.400	< 0.746	0.872	1.5
P_6	0.310 ± 0.015	0.828 ± 0.026	0.841	2.2

a negative g_1 and a positive g_2, as shown in Table 4.1. Overall, comparing the computed ΔS_8 values among different positions shows how variations in the PSF model along the field-of-view can produce more than 2σ tension (P_4) regarding this structure growth parameter.

The goal of simulating the effect of systematics on cosmological parameters is to quantify their impact in future measurements so this can be accounted for and subsequently removed. The differences in the impact of PSF variation show how an inaccurate correction of the PSF model may introduce errors associated to measurements done in specific regions of the field-of-view, that will directly affect cosmological parameter constraints. As the expected precision of future missions, such as *Euclid*, increases, issues such as this will become specially concerning, and must be a target of extensive analysis.

5.3.2 Impact from image manipulation procedures

Similar to what was done for the impact of PSF variation, multiplicative bias values, summarised in Table C.2, were applied to Eq. (5.6) so as to obtain the biased correlation functions corresponding to each of the image manipulation procedures. For this part of the work, the grid used to probe the parameter space was built with enough resolution to apply a *Euclid*-like rescaling of the survey area, so that the results here presented simulate what is expected for the size of *Euclid*'s confidence regions.

As defined in Section 5.2.3, the biased models chosen for this analysis correspond to cases II, IId, and IV, already described in Chapter 4. Case III was excluded from this analysis since it was found that the residual bias left when comparing this case with the remaining cases resulted in the constraint contours falling partially outside of the larger parameter grid, thus not being fully probed. Each case affects the estimation of cosmological parameters due to its own bias, originating from the many factors explored in previous chapters, such as the PSF correction algorithm itself. This type of bias is generally accounted for and removed from the observations by marginalising the cosmological parameter constraints over the m and c bias values. However, an additional residual error might be introduced due to the difference in the correction of image manipulation procedures, that might not have been taken into consideration.

The constraint contours presented in Fig. 5.3 compare the unbiased model parameters with the posterior distributions resulting from the residual effect due to the difference in correcting procedures. Therefore, the top, left-hand panel illustrates the effect of the additional bias introduced due to correcting a stacked image with an effective combined PSF (case II), instead of correcting each dither individually (case IId), and vice-versa. The remaining panels show the same type of comparison, between correcting a stacked image with an individual PSF (case IV), instead of an effective combined PSF (case II); and between correcting a stacked image with an individual PSF (case II) as opposed to correcting each dither individually (case IId). Each comparison is plotted with its inverse correction, both being located in

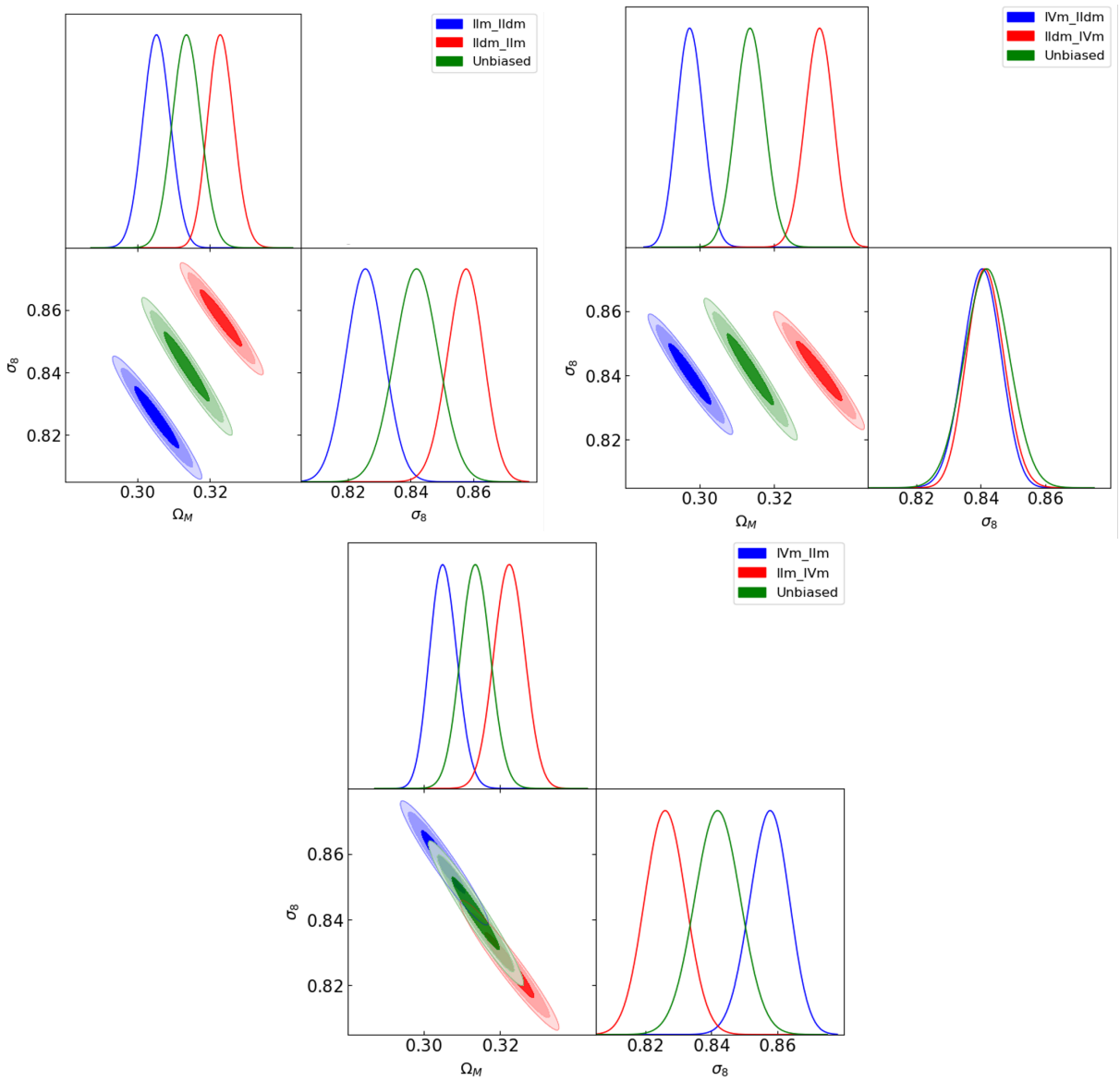

Figure 5.3: Marginalised posterior distributions in the $\Omega_m - \sigma_8$ plane of simulated unbiased ΛCDM model (green) and the different case comparisons, explicit in the label.

opposite directions, depending on which is considered the fiducial model.

From Fig. 5.3, it is possible to observe how different image processing methods can leave residual errors that greatly impact the constraints of cosmological parameters. Assuming that the common sources of systematics between the different procedures are known and corrected, such as the average intrinsic ellipticity of galaxies and residuals from a specific PSF correcting algorithm, the remaining bias can be attributed to the procedures themselves. Therefore, the differences shown in this figure represent the additional bias that may not have been corrected, and that could be affecting the measurements.

Considering the top, left-hand panel, and assuming case IId as the ideal correction method, where each dithered image is corrected by its true convolved PSF, then the difference resulting from the correction by a stacked image with an effective combined PSF shows a residual systematic that affects the values of σ_8 and Ω_m in more than 2σ, calculated from the values in Table 5.3. This effect results from varying, not only the PSF model used as the basis for the PSF distortion removal, but also the procedure itself, with one case being computed from the shear in a stacked image and the other through an averaged

Table 5.3: Results from biased model performance represented by S_8, as well as maximum likelihood parameter values for Ω_m and σ_8.

	$\Omega_m \pm \Delta\Omega_m$	$\sigma_8 \pm \Delta\sigma_8$	S_8	$\Delta S_8(\%)$
Unbiased	0.312 ± 0.003	0.840 ± 0.004	0.860	0.0
IId-II	0.323 ± 0.003	0.857 ± 0.005	0.889	3.4
II-IId	0.305 ± 0.004	0.826 ± 0.006	0.833	3.2
IId-IV	0.332 ± 0.004	0.842 ± 0.005	0.885	2.8
IV-IId	0.297 ± 0.003	0.840 ± 0.005	0.837	2.8
II-IV	0.322 ± 0.004	0.826 ± 0.006	0.856	0.5
IV-II	0.305 ± 0.003	0.858 ± 0.006	0.865	0.5

shear from individual exposures. This also includes noise variation, as the stacked image simulates an exposure time four times the duration of one dither. In this comparison, the direction of the constraint contours remains the same as the unbiased model, while showing a $45°$ offset in the parameter space.

On the other hand, comparing this ideal case with the correction of a stacked image by an individual PSF (top, right-hand panel) appears to conserve the value for σ_8 (with a deviation of less than 1σ) and greatly impact Ω_m in more than 4σ. The results from this comparison originate from similar conditions as the previous panel, with the respective constraint contours aligning in σ_8, with an offset regarding Ω_m, as seen from the values of the maximum likelihood parameters. This unexpected alignment may suggest a possible way of breaking the degeneracy between these two cosmological parameters, and distinguishing Ω_m effects from the impact of σ_8.

The residual error remaining between different correction methods for the two stacked images (bottom panel) behaves similarly as the top left-hand panel, regarding the impact on cosmological parameter constraints, with a deviation of more than 2σ for both. Here, the impact results solely from the variation in PSF correction, as both stacked images are the same, remaining along the line of degeneracy.

The relative bias between methods II and IV is the smallest one. There is a slight shift of the contours along the degeneracy, and thus the impact on S_8 is negligible. This shows that the *Euclid* PSF varies very little from dither to dither position. In this way, the 4-dither averaged PSF used in case II is very similar to the single dither PSF used in case IV.

The main differences arise when using case IId. This shows that measuring the shapes in individual dithers (IId) is different from measuring the shapes in stacked images (II or IV). Note that the relative bias between IId and the other cases is also partly due to the smaller signal-to-noise of the individual dithers compared to the stacked images. The relative bias propagates directly into a change of S_8. The impact is slightly different when comparing the two pairs. While the relative bias between IId and II moves the contours orthogonally to the degeneracy direction, the relative bias between IV and II moves them both orthogonally and along the direction (the result of these two movements being contours shifted horizontally along Ω_m only). This behaviour shows that the analyses are consistent; indeed it can be written schematically as $IId/II + II/IV = IId/IV$, or in terms of operations in the $\Omega_m - \sigma_8$ plane: orthogonal displacement + collinear displacement = horizontal displacement. This is indeed what is shown in Fig. 5.3, starting from the unbiased green ellipse in the top-left panel, moving it orthogonally to the red ellipse in the same panel, and moving it collinearly as the red ellipse in the bottom panel, will result in the red ellipse in the top-right panel.

Table 5.3 shows the constraints on Ω_m, σ_8, and S_8 resulting from the various relative biases. In order to quantify the contribution of this systematic to the problem of the σ_8 tension discussed in the literature, S_8 variations are here given in absolute values instead of relative sigma values. This is because in this

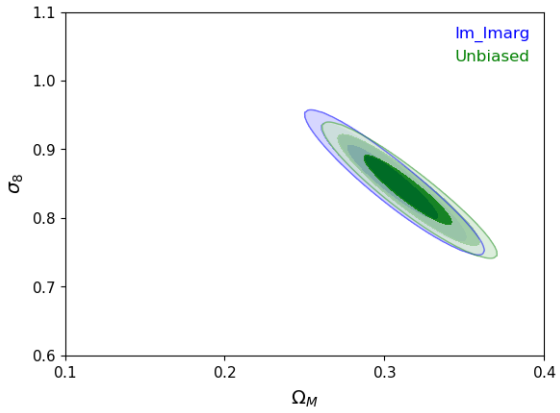

Figure 5.4: Marginalised posterior distribution in the $\Omega_m - \sigma_8$ plane, comparing the simulated unbiased ΛCDM constraint (green) with the confidence regions evaluated for case I (P6) marginalised over the bias parameter m.

analysis all the other cosmological parameters are kept fixed, while the results given in literature (for example the values discussed in Fig. 5.1) result from analyses where a higher-dimensional parameter space was probed (i.e., the results for S_8 are marginalised over a large number of parameters). In this way, the uncertainties for S_8 here presented are artificially smaller, and should not be used to set the sigma scale. It is then better to directly compare the ΔS_8 values.

As seen in Table 5.3, S_8 varies at most 0.034 (for the worst case IId/II) as compared to the unbiased case. This may indicate that for *Euclid*, the impact of this type of image manipulation relative biases will not be a major contribution to the σ_8 tension (that is currently at the level of ΔS_8 0.05-0.1 as discussed in Fig. 5.1).

Although the comparison shown in Fig. 5.3 results from different values for the multiplicative bias, the impact on cosmological parameter constraints is, in some cases, at the same level, indicating a possible degeneracy between the bias values. This effect has been observed and reported, where different values for m and c affected the estimation of cosmological parameters in the same way [63].

Besides analysing the residual bias, it is also possible to consider the impact on the size of the contours. In Fig. 5.3, the contour sizes are similar, since all grids where made in similar conditions, and no relevant impact is seen. However, more relevant might be the inclusion of the uncertainty on the calibration m parameters in the analyses. For this, 4-dimensional grids can be considered, including not only $\Omega_{\rm m}$ and σ_8, but also m_1 and m_2. As an example, such a grid was built for the case I, with the range of the m parameters extending to their $\pm 3\sigma$ values (the 1σ values are given in table C.2). Note that here, the case I was used both for the observed and for the theoretical correlation functions, and therefore it is an unbiased case. This method allowed producing contours on the $(\Omega_m,\ \sigma_8)$ plane, marginalised over m_1 and m_2. The contours are slightly larger that the corresponding ones for the original case of fixed m values. Figure 5.4 shows the resulting marginalised and the fixed contours. In this analysis a larger grid was used, for a covariance matrix scaled for 1000 $\deg^2$, and not for *Euclid*, hence the relatively larger contours. As seen in this figure, the marginalised contour is slightly larger than the one for the fixed case, as expected.

The increase in uncertainty can be quantified by computing the *Figure-of-merit* (FoM) of the $\Omega_m - -\sigma_8$ contour. The FoM was originally introduced to quantify the constraining power on dark energy parameters, but it may be applied to any contour plot. In this case, it is defined as

$$\mathrm{FoM} = \frac{1}{\sqrt{det(C_{\Omega_m \sigma_8})}}, \tag{5.8}$$

where $C_{\Omega_m \sigma_8}$ is the covariance matrix of the resulting posterior distribution. The FoM is thus inversely proportional to the area of the contour, and the larger it is, the stronger is the contraint. The FoM was originally defined for elliptical contours, such as the ones produced with the Fisher matrix approximation. However, given the small size of the contours in this analysis, they are well fitted by ellipses. To evaluate the covariance matrix, likelihood-weighted variances are computed from the points in the grid. The results for the KiDS-like scaling are: FoM = 10553 (marginalised case) and FoM = 11286 (fixed case). The relatively large uncertainties on the m parameters produce then a decrease of 6% on the FoM. For curiosity, the typical values of FoM for the *Euclid* scaling are of the order of 200,000. For comparison, the recent values of the $\Omega_m\,\sigma_8$ FoM found by the DES Year 3 analyses [64], considering their $\xi_\pm$ weak lensing only analysis, resulted in a FoM of the order of 1000. This is consistent with the fact that they found, for that case, errors of $\sim 10\%$ for both Ω_m and σ_8, while in this work's simplified analysis for the *Euclid* scaling with all additional cosmological parameters fixed, the errors were found to be around 3%. Since the FoM scales with the area, that is with the errors squared, this work consistently found a FoM around 100 times larger. Even though presenting a "toy-analysis", it must be kept in mind that the *Euclid* area is 3 times larger than DES and the number density of galaxies is 5 times larger, and as such, *Euclid* has the potential to be a large improvement with respect with current state-of-the-art weak lensing surveys, and this again calls for a very careful study of all systematics.

Overall, these final results permitted evaluating the impact that these common image manipulation procedures and PSF variations might have on weak lensing measurements, demonstrating the importance of accurately calibrating each data processing step regarding systematics, so as to reach the level of precision required in future cosmology missions.

Chapter 6

Conclusions and Future Work

This thesis presents an analysis of the biases introduced by common image manipulation procedures, and their impact on the estimation of cosmological parameters. With the increase of precision of the requirements for future cosmological tests, the need for this type of analysis also grows, as systematic errors become a concerning limitation to future observations.

Calibration tests done with the larger sample of parametric galaxies measured additive and multiplicative biases derived from *GalSim*'s implementation of the KSB algorithm, in the presence of noise, and as a function of variable cosmic shear signal. The results showed a clear separation between the two shear components, most likely derived from PSF properties. The analysis of the results binned in intervals of redshift, magnitude, and size, showed a weak correlation with the first property, while confirming that fainter, smaller galaxies are more susceptible to systematics, particularly in the presence of noise. Results from the analysis without binning showed an improvement in uncertainty, while reflecting lower m and c values. Overall, these calibration tests produced a negative multiplicative bias of the order of $\sim 10^{-2}$, and an additive bias of $\sim 10^{-2}$ for g_1 (associated with the high ellipticity component of the PSF), and $\sim 10^{-3}$ for g_2. Although the second shear component of the applied PSF was approximately zero, it has been reported that the KSB algorithm allows cross-contamination of residuals between components [51], which may explain the additive bias values for g_2 still being higher than expected, considering g_2^{PSF}.

Simulated *Euclid*-like galaxy images were then created, using 10% of the original sample. Non-binned results from PSF variation along *Euclid*'s field-of-view showed biases of the same order as before (negative multiplicative bias of $\sim 10^{-2}$, and an additive bias of $\sim 10^{-3}$ for both components). Although the PSF models produced with *PSFToolkit* were very similar regarding ellipticity, it is still possible to observe that even small variations can produce varied residual levels. These results also reflect inconsistencies related to the expected values of additive bias. Although a residual shear offset of $\sim 10^{-3}$ is in agreement with the c values obtained in previous works, considering the low ellipticity of the PSF models, it would be expected that these values would be even lower. Instead they appear on the same order of the PSF itself, implying an inefficient PSF correction. This type of additional bias is observed throughout Chapter 4, and is most likely a combined effect of KSB residuals, and systematics due to sample reduction. Although the reduced sample was analysed in its properties, in order to guarantee the similarity with the original galaxy catalogue, its mean intrinsic ellipticity changed to a value of the same order but negative, in both components. This reduction also introduced higher variability in the intrinsic shape of the galaxies in the sample. Albeit the small changes, the KSB method is known for introducing higher residual errors when correcting sources with higher ellipticity, or when removing highly elliptical PSFs [51]. Considering that this algorithm is applied individually to each galaxy, and that this sample

allows for an ellipticity dispersion of ~ 0.3, the analysis of 10% of the original sample might be too susceptible to residual errors from a poor PSF correction of the galaxies with higher ellipticities. Statistical fluctuations that were not detected in the calibration tests may also be affecting measurements in the reduced sample.

Apart from studying *Euclid*'s PSF variation with the position in its field-of-view, the same galaxy images, simulating *Euclid*'s observing conditions, were used to quantify biases introduced by common image manipulation procedures, such as dithering and subsequent stacking of these dithered images. Five different cases were compared, differing in the amount of noise, PSF model correction, and manipulation processes. Two cases represented the same stacked images, corrected by two different PSF models (cases II and IV), neither of which being the same as the initially convolved one; one case was simulated as a longer exposure, four times the duration of one *Euclid* VIS dither (case III); another case was computed from the average of the corrected shear values from the four dithered images (case IId); and finally, a last case was obtained considering shear values from a single dither, corrected by its own true PSF (case I). All five cases were computed for the same position in the field-of-view. Results from PSF correction of both stacked images, obtained by first simulating *Euclid*'s dithering process, showed a higher multiplicative bias than the remaining cases, resulting from removing PSF distortions based on a PSF model that was not the true convolved one. Multiplicative bias values for case IId were the lowest, followed by case III, and finally case I. Comparing the lower biases in the last three cases to the results from the stacking procedure shows a clear difference in the residuals due to correcting with the true PSF instead of an effective one. The amount of noise in the different images appears to be reflected in the uncertainty values of both additive and multiplicative biases, with case III generally presenting the lowest errors, and case I the highest.

The multiplicative bias values from Chapter 4 were used to evaluate the impact of these procedures in the estimation of cosmological parameters Ω_m and σ_8, leading to the calculation of the structure growth parameter, S_8, as a measure of deviation from an unbiased model. The computation of biased correlation functions, using *nicaea*, resulted in constraint contours corresponding to both the effects from PSF variation and from residual correction errors due to image processing methods. The results showed how small PSF changes along the field-of-view can greatly affect parameter estimation, and demonstrate how this effect, if incorrectly calibrated, can produce significant deviations from the expected cosmological model. Analysis of the constraints obtained from differences in image manipulation procedures are useful in understanding possibly unaccounted systematics, confirming the need for accurate calibration of each processing step in data reduction, particularly considering *Euclid*'s precision requirements.

Overall, the results presented in this thesis are limited to the implementation of one particular PSF correcting algorithm, and were impacted by computational limitations. Improvements can be done to this work in order to limit uncontrolled effects on bias measurements. These may include the rotation of galaxy orientations so as to guarantee a perfectly symmetric sample, with zero mean intrinsic ellipticity; the analysis of signal-to-noise ratio, which might clarify issues in the bias values, in conjunction with size and magnitude properties; and the addition of calibration tests done in simple galaxy models. Most importantly, producing this study in an even larger galaxy sample would certainly aid in decreasing the uncertainty, and avoid statistical effects.

Future work can be done using the knowledge and expertise gained throughout this thesis, in the scope of model performance evaluation. All the procedures studied and presented in this work can be analysed while varying other aspects of cosmological observations. One being the characteristic galaxy colour gradients, which, as described in Chapter 2, will introduce a colour gradient bias in future *Euclid* data. The quantification of this effect is already being done, in the context of *Euclid*, but could also be

applied to the framework here presented. Another variable that may be added to this type of analysis is pixel scale variation, since pixelation affects the rendering of galaxy shapes in an image. Finally, other image processing methods can be considered, beyond dithering and stacking, such as aliasing, or image registration, both relevant in future *Euclid* measurements.

As has been the key lesson throughout this thesis, with the evolution of cosmological data comes the need for better, more accurate calibration methods. From PSF modelling and its proper removal, to the impact of posterior image processing procedures, every step of data handling must be evaluated, and the resulting systematic errors quantified. This thesis, albeit in a humble way, has attempted to contribute to this ever-evolving work.

Bibliography

[1] Einstein, A. (1918). Prinzipielles zur allgemeinen Relativitätstheorie. *Annalen der Physik*, 360(4): 241–244.

[2] Einstein, A. (1917). Kosmologische Betrachtungen zur allgemeinen Relativitätstheorie. *Sitzungsberichte der Königlich Preußischen Akademie der Wissenschaften (Berlin)*, pages 142–152, .

[3] Lemaître, G. (1927). Un univers homogène de masse constante et de rayon croissant rendant compte de la vitesse radiale des nébuleuses extra-galactiques. *Annales de la Société Scientifique de Bruxelles*, 47:49–59.

[4] Hubble, E. (1929). A relation between distance and radial velocity among extra-galactic nebulae. *Proceedings of the National Academy of Sciences*, 15(3):168–173.

[5] Lemaître, G. (1931). The Beginning of the World from the Point of View of Quantum Theory. *Nature*, 127(3210):706.

[6] Alpher, R. A. & Herman, R. (1948). Evolution of the Universe. *Nature*, 162(4124):774–775.

[7] Penzias, A. & Wilson, R. W. (1965). A Measurement of Excess Antenna Temperature at 4080 Mc/s. *The Astrophysical Journal*, 142:419–421.

[8] Sachs, R. K. & Wolfe, A. M. (1967). Perturbations of a Cosmological Model and Angular Variations of the Microwave Background. *The Astrophysical Journal*, 147:73.

[9] Harrison, E. R. (1970). Fluctuations at the Threshold of Classical Cosmology. *Physical Review D*, 1:2726–2730.

[10] Zeldovich, Ya. B. (1972). A Hypothesis, Unifying the Structure and the Entropy of the Universe. *Monthly Notices of the Royal Astronomical Society*, 160(1):1P–3P.

[11] Doroshkevich, A. G., Sunyaev, R. A. & Zeldovich, Ya. B. (1974). The formation of galaxies in Friedmannian universes. In M. S. Longair, editor, *Confrontation of Cosmological Theories with Observational Data*, volume 63, pages 213–225.

[12] Peebles, P. J. E. (1982). Large-scale background temperature and mass fluctuations due to scale-invariant primeval perturbations. *The Astrophysical Journal Letters*, 263:L1–L5.

[13] Bennett, C. L., Halpern, M., Hinshaw, G., et al. (2003). First-Year Wilkinson Microwave Anisotropy Probe (WMAP) Observations: Preliminary Maps and Basic Results. *The Astrophysical Journal Supplement Series*, 148(1):1–27.

[14] Einstein, A. (1917). *Letter to de Sitter*. CPAE 8 (Doc. 325), . URL `https://einsteinpapers.press.princeton.edu/vol8-trans/343`.

[15] LIGO Scientific Collaboration and Virgo Collaboration: Abbott, B. P., Abbott, R., Abbott, T. D., et al. (2016). Observation of gravitational waves from a binary black hole merger. *Physical Review Letters*, 116:061102.

[16] Event Horizon Telescope Collaboration: Akiyama, K., Alberdi, A., Alef, W., et al. (2019). First M87 Event Horizon Telescope Results. I. The Shadow of the Supermassive Black Hole. *The Astrophysical Journal Letters*, 875(1):L1.

[17] Schneider, P., Ehlers, J. & Falco, E. (1992). *Gravitational Lenses*. Springer-Verlag New York.

[18] Heymans, C., Van Waerbeke, L., Bacon, D., et al. (2006). The Shear Testing Programme – I. Weak lensing analysis of simulated ground-based observations. *Monthly Notices of the Royal Astronomical Society*, 368(3):1323–1339.

[19] Massey, R., Heymans, C., Bergé, J., et al. (2006). The Shear TEsting Programme 2: Factors affecting high precision weak lensing analyses. *Monthly Notices of the Royal Astronomical Society*, 376.

[20] Bridle, S., Balan, S., Bethge, M., et al. (2010). Results of the GREAT08 Challenge: An image analysis competition for cosmological lensing. *Monthly Notices of the Royal Astronomical Society*, 405:2044 – 2061.

[21] Kitching, T., Amara, A., Gill, M., et al. (2011). Gravitational Lensing Accuracy Testing 2010 (GREAT10) Challenge Handbook. *The Annals of Applied Statistics*, 5(3):2231–2263.

[22] Kilbinger, M. (2015). Cosmology with cosmic shear observations: a review. *Reports on Progress in Physics*, 78(8):086901.

[23] Aghanim, N., Akrami, Y., Ashdown, M., et al. (2020). Planck 2018 results. *Astronomy & Astrophysics*, 641:A6, Sep .

[24] Mo, H., van den Bosch, F. C. & White, S. (2010). *Galaxy Formation and Evolution*. Cambridge University Press, .

[25] Coles, P.P. & Lucchin, P.F. (2003). *Cosmology: The Origin and Evolution of Cosmic Structure*. Wiley.

[26] Bartelmann, M. & Schneider, P. (2001). Weak gravitational lensing. *Physics Reports*, 340(4–5): 291–472, .

[27] Peter, P. & Uzan, J. P. (2009). *Primordial Cosmology*. OUP Oxford.

[28] D'Inverno, R. (1992). *Introducing Einstein's Relativity*. Oxford University Press, Cambridge, U.K.

[29] Kaiser, N., Squires, G. & Broadhurst, T. (1995). A method for weak lensing observations. *The Astrophysical Journal*, 449(460).

[30] Shapiro, C., Rowe, B. T. P., Goodsall, T., et al. (2013). Weak gravitational lensing systematics from image combination. *Publications of the Astronomical Society of the Pacific*, 125(934):1496–1513.

[31] Laureijs, R., Amiaux, J., Arduini, S., et al. (2011). Euclid definition study report.

[32] Euclid Collaboration: Paykari, P., Kitching, T., and Hoekstra, H., et al. (2020). Euclid preparation - VI. Verifying the Performance of Cosmic Shear Experiments. *Astronomy & Astrophysics*, 635: A139, Mar .

[33] Cropper, M., Pottinger, S., Niemi, S., et al. (2016). VIS: the visible imager for Euclid. *Space Telescopes and Instrumentation 2016: Optical, Infrared, and Millimeter Wave*.

[34] Er, X., Hoekstra, H, Schrabback, T., et al. (2018). Calibration of colour gradient bias in shear measurement using HST/CANDELS data. *Monthly Notices of the Royal Astronomical Society*, 476 (4):5645–5657.

[35] Rowe, B. T. P., Jarvis, M., Mandelbaum, R., et al. (2015). GALSIM: The modular galaxy image simulation toolkit. *Astronomy and Computing*, 10:121–150.

[36] Mandelbaum, R., Rowe, B., Bosch, J., et al. (2014). The Third Gravitational Lensing Accuracy Testing GREAT3 Challenge Handbook. *The Astrophysical Journal Supplement Series*, 212(1):5.

[37] Mandelbaum, R., Lackner, C., Leauthaud, A. & Rowe, B. (2012). Cosmos real galaxy dataset. URL `https://doi.org/10.5281/zenodo.3242143`.

[38] Scoville, N., Aussel, H., Brusa, M., et al. (2007). The cosmic evolution survey (COSMOS): Overview. *The Astrophysical Journal Supplement Series*, 172(1):1–8.

[39] Hirata,C. & Seljak, U. (2003). Shear calibration biases in weak-lensing surveys. *Monthly Notices of the Royal Astronomical Society*, 343(2):459–480.

[40] Mandelbaum, R., Hirata, C., Seljak, U., et al. (2005). Systematic errors in weak lensing: application to SDSS galaxy-galaxy weak lensing. *Monthly Notices of the Royal Astronomical Society*, 361(4): 1287–1322.

[41] Euclid Collaboration: Martinet, N., Schrabback, T., Hoekstra, H., et al. (2019). Euclid preparation - IV. Impact of undetected galaxies on weak-lensing shear measurements. *Astronomy & Astrophysics*, 627:A59.

[42] Mo, H., van den Bosch, F. C. & White, S. (2010). *Galaxy Formation and Evolution*. Cambridge University Press, .

[43] Hoekstra, H., Franx, M., Kuijken, K. & Squires, G. (1998). Weak lensing analysis of cl 1358+62. *New Astronomy Reviews*, 42(2):137 – 140.

[44] Bartelmann, M. & Schneider, P. (2001). Weak gravitational lensing. *Physics Reports*, 340(4-5): 291–472, Jan .

[45] Luppino, G. A. & Kaiser, N. (1997). Detection of Weak Lensing by a Cluster of Galaxies at z= 0.83. *The Astrophysical Journal*, 475(1):20–28, jan .

[46] Erben, T., Van Waerbeke, L., Bertin, E., Mellier, Y. & Schneider, P. (2001). How accurately can we measure weak gravitational shear? *Astronomy & Astrophysics*, 366(3):717–735, .

[47] Deshpande, A. C., Kitching, T. D., Cardone, V. F., Taylor, P. L. et al. (2020). Euclid: On the reduced shear approximation and magnification bias for stage iv cosmic shear experiments. *Astronomy & Astrophysics*, 636(3):717–735.

[48] Euclid Collaboration: Blanchard, A., Camera, S., Carbone, C., et al. (2020). Euclid preparation - VII. Forecast validation for Euclid cosmological probes. *Astronomy & Astrophysics*, 642:A191.

[49] Hoekstra, H., Viola, M. & Herbonnet, R. (2017). A study of the sensitivity of shape measurements to the input parameters of weak-lensing image simulations. *Monthly Notices of the Royal Astronomical Society*, 468(3):3295–3311.

[50] Semboloni, E., Tereno, I., Van Waerbeke, L. & Heymans, C. (2009). Sources of contamination to weak lensing tomography: redshift-dependent shear measurement bias. *Monthly Notices of the Royal Astronomical Society*, 397(2):608–622.

[51] Viola, M., Melchior, P. & Bartelmann, M. (2011). Biases in, and corrections to, KSB shear measurements. *Monthly Notices of the Royal Astronomical Society*, 410(4):2156–2166.

[52] Nakajima, R. & Bernstein, G. (2007). Shear recovery accuracy in weak-lensing analysis with the elliptical gauss-laguerre method. *The Astronomical Journal*, 133(4):1763–1779, mar .

[53] Howell, S. (2006). *Handbook of CCD Astronomy*. Cambridge observing handbooks for research astronomers, Vol. 5 Cambridge, UK: Cambridge University Press.

[54] Tewes, M., Kuntzer, T., Nakajima, R., Courbin, F. Hildebrandt, H. & Schrabback, T. (2018). Weak-lensing shear measurement with machine learning. Teaching artificial neural networks about feature noise. *Astronomy & Astrophysics*, 621.

[55] Amendola, L. & Tsujikawa, S. (2010). *Dark Energy: Theory and Observations*. Cambridge University Press.

[56] Wang, Y. (2010). *Dark Energy*. Wiley Series in Cosmology. Wiley.

[57] Dark Energy Survey Collaboration 1: Abbott, T. M. C., Abdalla, F. B., Alarcon, A., et al. (2018). Dark Energy Survey year 1 results: Cosmological constraints from galaxy clustering and weak lensing. *Physical Review D*, 98:043526, Aug .

[58] Tröster, T., Sánchez, A. G., Asgari, M., et al. (2020). Cosmology from large-scale structure. *Astronomy & Astrophysics*, 633:L10, Jan .

[59] Heymans, C., Tröster, T., Asgari, M., et al. (2021). KiDS-1000 Cosmology: Multi-probe weak gravitational lensing and spectroscopic galaxy clustering constraints. *Astronomy & Astrophysics*, 646:A140.

[60] Kilbinger, M., Benabed, K., Guy, J., et al. (2009). Dark-energy constraints and correlations with systematics from CFHTLS weak lensing, SNLS supernovae Ia and WMAP5*. *Astronomy & Astrophysics*, 497(3):677–688.

[61] Martinet, N., Harnois-Déraps, J., Jullo, E. & Schneider, P. (2021). Probing dark energy with tomographic weak-lensing aperture mass statistics. *Astronomy & Astrophysics*, 646:A62, Feb .

[62] Giocoli, C., Baldi, M. & Moscardini, L. (2018). Weak lensing light-cones in modified gravity simulations with and without massive neutrinos. *Monthly Notices of the Royal Astronomical Society*, 481(2):2813–2828, 09 .

[63] Massey, R., Hoekstra, H., Kitching, T., et al. (2012). Origins of weak lensing systematics, and requirements on future instrumentation (or knowledge of instrumentation). *Monthly Notices of the Royal Astronomical Society*, 429(1):661–678, 12 .

[64] DES collaboration: Abbott, T. M. C., Aguena, M., Alarcon, A., et al. (2021). Dark Energy Survey Year 3 Results: Cosmological Constraints from Galaxy Clustering and Weak Lensing. arXiv:2105.13549.

Appendix A

GalSim configuration: Input shear values

Table A.1: Input shear values.

g_1	-0.06	-0.05	-0.04	-0.03	-0.02	-0.01	0.005	0.02	0.04	0.06
g_2	0.06	0.01	-0.03	0	0.05	-0.01	-0.002	0.02	-0.04	-0.06

Appendix B

Summary of results from calibration test sets

B.1 Test sets T1 and T2

Table B.1: Best-fit values for calibration bias, m, and additive bias, c, for the two components of shear, g_1 and g_2, for each redshift bin. Averages for the four parameters over the entire redshift range are presented in the last row.

z	m_1 (10^{-2})	c_1 (10^{-3})	m_2 (10^{-2})	c_2 (10^{-3})
$0.001 - 0.418$	-1.26 ± 0.09	-13.62 ± 0.03	-2.14 ± 0.06	0.87 ± 0.02
$0.418 - 0.56$	-1.15 ± 0.12	-15.05 ± 0.04	-2.19 ± 0.07	-1.30 ± 0.03
$0.56 - 0.678$	-1.82 ± 0.11	-11.09 ± 0.04	-2.09 ± 0.06	-0.83 ± 0.02
$0.678 - 0.789$	-1.31 ± 0.09	-12.81 ± 0.03	-2.13 ± 0.05	1.00 ± 0.02
$0.789 - 0.9$	-1.05 ± 0.09	-17.28 ± 0.03	-2.21 ± 0.06	3.13 ± 0.02
$0.9 - 1.019$	-1.25 ± 0.09	-17.75 ± 0.03	-2.13 ± 0.07	0.67 ± 0.02
$1.019 - 1.155$	-1.54 ± 0.12	-12.39 ± 0.04	-2.45 ± 0.07	6.23 ± 0.03
$1.155 - 1.324$	-1.23 ± 0.10	-16.93 ± 0.03	-2.05 ± 0.07	-0.74 ± 0.02
$1.324 - 1.576$	-1.73 ± 0.09	-15.13 ± 0.03	-1.99 ± 0.06	3.78 ± 0.02
$1.576 - 2.5$	-1.83 ± 0.16	-15.70 ± 0.06	-2.59 ± 0.07	-2.31 ± 0.03
Mean	-1.42 ± 0.09	-14.77 ± 0.71	-2.20 ± 0.06	1.05 ± 0.83

Table B.2: Best-fit values for multiplicative bias, m, and additive bias, c, for the two components of shear, g_1 and g_2, for each magnitude bin. Averages for the four parameters over the entire magnitude range are presented in the last row.

m_{814}	m_1 (10^{-2})	c_1 (10^{-3})	m_2 (10^{-2})	c_2 (10^{-3})
$16.2 - 22.0$	-2.77 ± 0.59	-19.58 ± 0.21	-5.02 ± 0.67	-0.58 ± 0.23
$22.0 - 22.9$	2.87 ± 0.79	-11.80 ± 0.29	0.44 ± 0.90	3.04 ± 0.31
$22.9 - 23.5$	-2.46 ± 0.68	-14.13 ± 0.25	0.87 ± 1.32	2.66 ± 0.45
$23.5 - 23.8$	-2.23 ± 0.61	-12.07 ± 0.22	-2.54 ± 1.10	-0.25 ± 0.38
$23.8 - 24.1$	0.13 ± 1.32	-16.46 ± 0.48	-4.50 ± 1.81	5.67 ± 0.62
$24.1 - 24.3$	-2.62 ± 0.44	-13.30 ± 0.16	-0.59 ± 1.28	-5.44 ± 0.44
$24.3 - 24.5$	-3.23 ± 0.94	-14.86 ± 0.34	-4.23 ± 1.11	-0.88 ± 0.38
Mean	-1.48 ± 0.83	-14.60 ± 1.03	-2.28 ± 0.96	0.60 ± 1.35

Table B.3: Best-fit values for multiplicative bias, m, and additive bias, c, for the two components of shear, g_1 and g_2, for each half-light radius bin. Averages for the four parameters over the entire half-light radius range are presented in the last row.

r_h	m_1 (10^{-2})	c_1 (10^{-3})	m_2 (10^{-2})	c_2 (10^{-3})
$0-6$	-2.49 ± 1.16	-12.70 ± 0.42	-2.82 ± 1.87	3.10 ± 0.64
$6-8$	0.67 ± 1.81	-16.37 ± 0.66	-2.00 ± 1.28	0.80 ± 0.44
$8-10$	-1.80 ± 0.95	-14.13 ± 0.35	-4.67 ± 0.65	1.16 ± 0.22
$10-13$	-1.16 ± 0.29	-14.22 ± 0.10	-0.56 ± 1.15	-1.43 ± 0.39
$13-17$	-2.13 ± 1.33	-12.78 ± 0.49	0.58 ± 1.89	0.96 ± 0.65
$17-60$	-1.46 ± 0.61	-17.83 ± 0.22	-4.47 ± 1.13	1.85 ± 0.39
Mean	-1.40 ± 0.46	-14.67 ± 0.83	-2.32 ± 0.86	1.07 ± 0.61

B.2 Test sets T3 and T4

Table B.4: Best-fit values for calibration bias, m, and additive bias, c, for the two components of shear, g_1 and g_2, averaged over redshift bin. Each entry corresponds to a different exposure time.

$t_{exp}(s)$	$\langle m_1 \rangle$ (10^{-2})	$\langle c_1 \rangle$ (10^{-3})	$\langle m_2 \rangle$ (10^{-2})	$\langle c_2 \rangle$ (10^{-3})
10	-1.71 ± 0.38	-14.67 ± 0.71	-2.70 ± 0.70	0.70 ± 0.80
30	-1.33 ± 0.15	-14.79 ± 0.74	-1.91 ± 0.32	1.09 ± 0.82
60	-1.75 ± 0.28	-14.94 ± 0.78	-3.56 ± 1.38	1.67 ± 1.16
120	-1.11 ± 0.35	-14.85 ± 0.72	-1.99 ± 0.21	1.06 ± 0.83
180	-1.42 ± 0.09	-14.80 ± 0.72	-2.17 ± 0.06	1.04 ± 0.82
T1&T2	-1.42 ± 0.09	-14.77 ± 0.71	-2.20 ± 0.06	1.05 ± 0.83

Table B.5: Best-fit values for calibration bias, m, and additive bias, c, for the two components of shear, g_1 and g_2, averaged over magnitude bin. Each entry corresponds to a different exposure time.

$t_{exp}(s)$	$\langle m_1 \rangle$ (10^{-2})	$\langle c_1 \rangle$ (10^{-3})	$\langle m_2 \rangle$ (10^{-2})	$\langle c_2 \rangle$ (10^{-3})
10	-2.28 ± 1.43	-14.61 ± 1.08	-4.73 ± 1.15	2.45 ± 1.51
30	-0.99 ± 0.97	-14.60 ± 1.18	-0.56 ± 1.32	2.90 ± 1.43
60	-1.91 ± 1.21	-14.73 ± 1.74	-1.46 ± 0.79	0.63 ± 2.09
120	-1.35 ± 1.19	-14.92 ± 1.68	-1.19 ± 0.92	0.67 ± 2.04
180	-1.95 ± 0.98	-14.78 ± 1.68	-1.39 ± 0.82	0.57 ± 2.08
T1&T2	-1.48 ± 0.83	-14.60 ± 1.03	-2.28 ± 0.96	0.60 ± 1.35

Table B.6: Best-fit values for calibration bias, m, and additive bias, c, for the two components of shear, g_1 and g_2, averaged over redshift bin. Each entry corresponds to a different exposure time.

$t_{exp}(s)$	$\langle m_1 \rangle$ (10^{-2})	$\langle c_1 \rangle$ (10^{-3})	$\langle m_2 \rangle$ (10^{-2})	$\langle c_2 \rangle$ (10^{-3})
10	-0.38 ± 0.48	-6.92 ± 0.73	-0.51 ± 1.23	-7.13 ± 0.66
30	-2.59 ± 0.59	-22.00 ± 1.10	-5.02 ± 1.46	8.66 ± 0.94
60	-2.28 ± 0.84	-17.34 ± 0.67	-2.00 ± 1.33	-1.43 ± 0.81
120	-1.23 ± 1.07	-14.90 ± 0.71	-0.25 ± 0.52	-3.04 ± 0.60
180	-0.87 ± 0.86	-11.10 ± 0.73	-2.01 ± 0.55	0.74 ± 0.57
T1&T2	-1.40 ± 0.11	-14.67 ± 0.04	-2.32 ± 0.06	1.07 ± 0.02

Appendix C

Summary of results from *Euclid* data simulations

C.1 Case I: PSF variation along the field-of-view

Table C.1: Best-fit values for multiplicative bias, m, and additive bias, c, for the two components of shear, g_1 and g_2, for each position in the field-of-view.

$Position$	m_1 (10^{-2})	c_1 (10^{-3})	m_2 (10^{-2})	c_2 (10^{-3})
P_1	0.27 ± 0.87	-8.87 ± 0.29	-0.92 ± 2.19	-1.87 ± 0.64
P_2	-0.33 ± 1.24	-8.50 ± 0.41	-3.71 ± 1.54	-3.04 ± 0.45
P_3	-0.92 ± 0.84	-7.89 ± 0.28	-2.76 ± 1.70	0.21 ± 0.49
P_4	-3.72 ± 1.55	-9.18 ± 0.51	-1.54 ± 2.18	-5.74 ± 0.63
P_5	-0.90 ± 1.12	-11.20 ± 0.37	-4.97 ± 1.96	-2.68 ± 0.57
P_6	-2.41 ± 2.15	-9.94 ± 0.71	-2.70 ± 2.89	-4.45 ± 0.84

C.2 Cases II, IId, III, and IV: Bias resulting from image manipulation

Table C.2: Best-fit values for multiplicative bias, m, and additive bias, c, for the two components of shear, g_1 and g_2, for each considered case.

$Cases$	m_1 (10^{-2})	c_1 (10^{-3})	m_2 (10^{-2})	c_2 (10^{-3})
I	-2.41 ± 2.15	-9.94 ± 0.71	-2.70 ± 2.89	-4.45 ± 0.84
II	-5.19 ± 1.67	-9.46 ± 0.55	-1.63 ± 1.00	-3.73 ± 0.29
IId	-1.15 ± 1.47	-9.40 ± 0.49	2.62 ± 1.68	-3.82 ± 0.49
III	-2.12 ± 0.85	-10.61 ± 0.28	-0.44 ± 1.10	-4.96 ± 0.32
IV	-5.39 ± 1.76	-9.88 ± 0.58	-1.74 ± 0.99	-3.60 ± 0.29